A Hydroelastic Method for the Analysis of Global Ship Response Due to Slamming Events

by

Dominic J. Piro

A dissertation submitted in partial fulfillment
of the requirements for the degree of
Doctor of Philosophy
(Naval Architecture and Marine Engineering)
in The University of Michigan
2013

Doctoral Committee:

Assitant Professor Kevin J. Maki, Chair
Professor Carlos E. Cesnik
Professor Armin W. Troesch
Associate Professor Yin Lu (Julie) Young

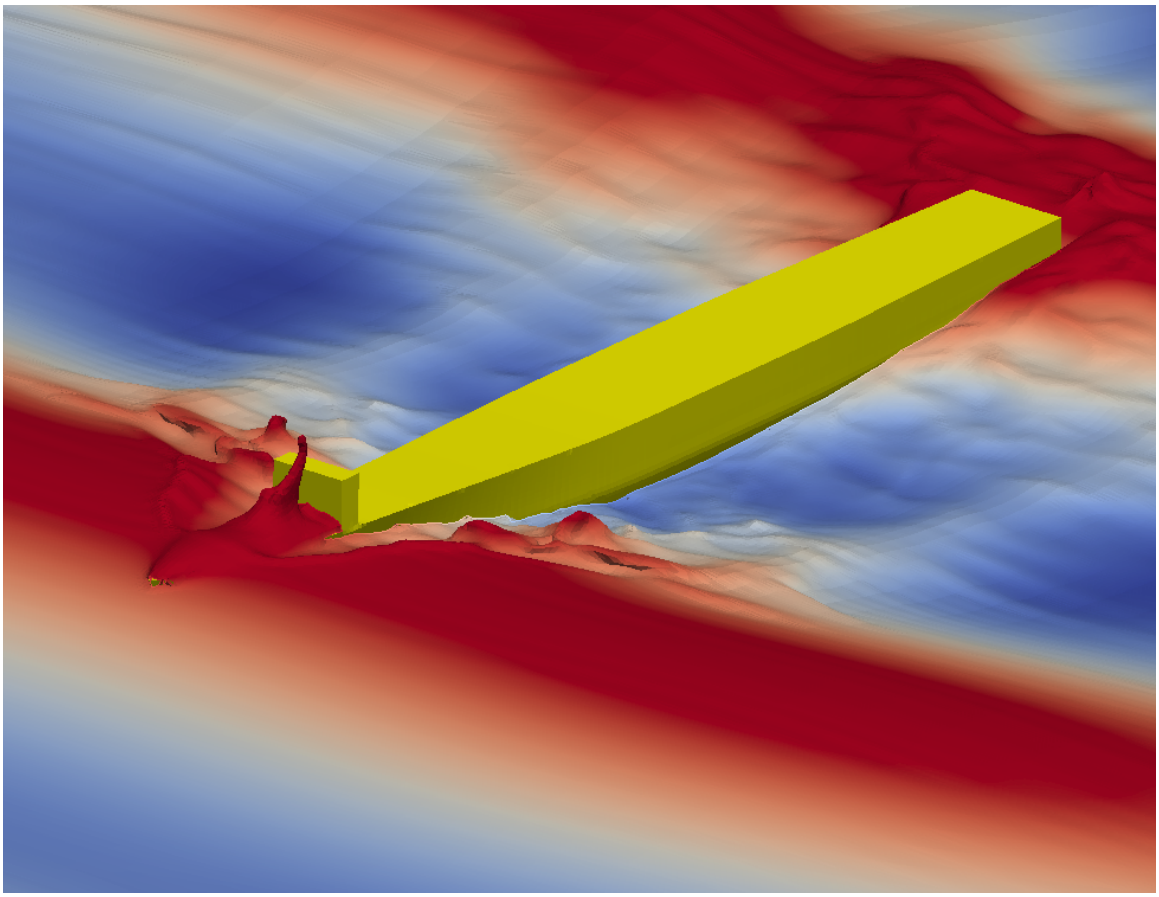

ACKNOWLEDGEMENTS

Thank you to my family, without whose support this would not be possible. I am especially appreciative of my wife, Caroline, who has dealt well with the consequences of my decision to pursue a doctoral degree.

I would like to thank my committee - Prof. Kevin Maki, Prof. Carlos Cesnik, Prof. Armin Troesch, and Prof. Julie Young - for all of the advice and mentoring throughout my graduate studies.

Thank you to my friends and fellow graduate students for helping me work through details of numerical implimentations, as well as providing a sounding board when I needed one.

I would also like to thank Dr. Tom Fu and Jayson Geiser at NSWCCD for providing the JHSS experimental data, without which my validation efforts would have been hampered.

I am grateful the the support offered by the Office of Naval Research and Kelly Cooper, under the awards #N00014-10-1-0301 and #N00014-11-1-0846.

TABLE OF CONTENTS

ACKNOWLEDGEMENTS ii

LIST OF FIGURES v

LIST OF TABLES vii

ABSTRACT viii

CHAPTER

I. Introduction 1

II. Background And Related Work 4

2.1 Hydroelastic Impact 4
2.2 Global Vessel Hydroelastic Response 8

III. Fluid-Structure Interaction Solver 13

3.1 Introduction 13
3.2 Fluid Domain Solution 13
3.3 Structural Domain 15
3.3.1 Modal Decomposition 15
3.3.2 Finite Element Modeling 17
3.4 Rigid Body Motion 24
3.5 Coupling of Fluid and Structure Domains 26
3.5.1 Under-Relaxation and Iterative Algorithm 26
3.5.2 Exchange of Data on the Mutual Interface 34
3.5.3 Fluid-Boundary Condition on the Mutual Interface . 35

IV. Hydroelastic Wedge Entry and Exit 37

4.1 Constant Velocity Hydroelastic Wedge Impact 38

4.1.1 Convergence of Finite-Element Discretization 39
4.1.2 Modal Convergence 40
4.1.3 CFD Grid Convergence 42
4.1.4 Comparison with Previous Numerical Simulations . 44
4.2 Entry and Exit of a Rigid Wedge 45
4.3 Entry and Exit of a Hydroelastic Wedge 50
4.4 Summary 59

V. An Elastic Ship in Waves 60

5.1 Wave Generation and Propogation 60
5.1.1 Two-dimensional Wave Generation and Damping . . 61
5.1.2 Wave Generation and Damping Evaluation 62
5.1.3 Two-dimensional Wave Propagation 63
5.2 Wigley Hull Seakeeping 67
5.3 Elastic Box Barge in Oblique Seas 68
5.4 JHSS Segmented Model in Head Seas 76
5.4.1 JHSS Model Tests 76
5.4.2 Numerical Set-up 77
5.4.3 Results and Analysis 84
5.4.4 Comparison to Hydroelastic Approximations 101
5.5 Summary 108

VI. Summary and Conclusions 109

6.1 Summary 109
6.2 Contributions 111
6.3 Future Work 113

BIBLIOGRAPHY 115

LIST OF FIGURES

Figure

3.1	Example of surface meshing.	18
3.2	Example of transfer elements.	23
3.3	Test box dropping into the water and subsequently floating.	32
3.4	Comparison of box heave time-series using different relaxation methods.	33
3.5	Illustration of grid matching.	35
4.1	Elastic wedge model.	38
4.2	Modal force for 18mm plate.	41
4.3	Deflection with different numbers of modes.	42
4.4	Modal convergence for magnitude and time of maximum deflection.	43
4.5	Deflection comparison for rigid wedge impact.	45
4.6	Pressure contours for Cases 2 and 4.	48
4.7	Wetted length comparision: entry and exit.	49
4.8	Force comparision: entry and exit.	50
4.9	Beam deflection for 12 mm beam	53
4.10	Beam deflection for 18 mm beam	54
4.11	Beam deflection for 32 mm beam	54
4.12	Beam deflection for 50 mm beam	55
4.13	Modal force for 50 mm beam	56
4.14	Maximum stress ratio: RQS	56
4.15	Maximum stress ratio: RDyn	58
5.1	Two-dimensional wave tank	63
5.2	Example time series of wave generation assesment.	64
5.3	Accuracy of wave generation and damping	65
5.4	Illustration of two-dimensional single wave domain.	65
5.5	Wave damping relative to M/λ and N/H	66
5.6	Wigley hull seakeeping in regular, head seas.	69
5.7	Wigley hull motions for three iteration, second order case.	69
5.8	Convergence of Wigley hull motions	70
5.9	Segmented box barge in study	71
5.10	Box barge shown in oblique seas	72
5.11	First three modes of box barge.	73
5.12	Comparison of box barge RAOs	75

5.13 JHSS model layout. 76
5.14 JHSS structural backspline cross-section geometry. 77
5.15 JHSS model in Run 478: 15 kts, 1/15 wave slope 79
5.16 First five dry mode shapes of JHSS numerical model. 80
5.17 JHSS fluid and structrual meshes on hull, views from above. 82
5.18 JHSS fluid and structural meshes on hull, views from below. 83
5.19 JHSS coarse grid with refinement block 84
5.20 JHSS impact flow for different grids. 85
5.21 JHSS experiment: RB motion - 15 knots, 1/30 wave slope. 86
5.22 JHSS seakeeping comparison: 15 knots, 1/15 wave slope case 87
5.23 JHSS seakeeping comparison: 15 knots, 1/30 wave slope case 87
5.24 JHSS seakeeping comparison: 35 knots, 1/30 wave slope case 88
5.25 JHSS coarse grid: BM time series - 15 knots, 1/15 wave slope. . . . 90
5.26 JHSS coarse grid: BM time series - 15 knots, 1/30 wave slope. . . . 90
5.27 JHSS coarse grid: BM time series - 35 knots, 1/30 wave slope. . . . 91
5.28 JHSS coarse grid: BM FFT - 15 knots, 1/15 wave slope. 92
5.29 JHSS coarse grid: BM FFT - 15 knots, 1/30 wave slope. 92
5.30 JHSS coarse grid: BM FFT - 35 knots, 1/30 wave slope. 93
5.31 JHSS fine grid: BM time series - 15 knots, 1/15 wave slope. 94
5.32 JHSS fine grid: BM time series - 15 knots, 1/30 wave slope. 94
5.33 JHSS fine grid: BM time series - 35 knots, 1/30 wave slope. 95
5.34 JHSS fine grid: BM FFT - 15 knots, 1/15 wave slope. 95
5.35 JHSS fine grid: BM FFT - 15 knots, 1/30 wave slope. 96
5.36 JHSS fine grid: BM FFT - 35 knots, 1/30 wave slope. 96
5.37 JHSS refined coarse grid: BM time series - 15 knots, 1/15 wave slope. 97
5.38 JHSS refined coarse grid: BM time series - 15 knots, 1/30 wave slope. 98
5.39 JHSS refined coarse grid: BM time series - 35 knots, 1/30 wave slope. 98
5.40 JHSS refined coarse grid: BM FFT - 15 knots, 1/15 wave slope. . . 99
5.41 JHSS refined coarse grid: BM FFT - 15 knots, 1/30 wave slope. . . 100
5.42 JHSS refined coarse grid: BM FFT - 35 knots, 1/30 wave slope. . . 100
5.43 JHSS coarse grid: BM comparison - 15 knots, 1/15 wave slope. . . . 102
5.44 JHSS coarse grid: BM comparison - 15 knots, 1/30 wave slope. . . . 102
5.45 JHSS coarse grid: BM comparison - 35 knots, 1/30 wave slope. . . . 103
5.46 JHSS fine grid: BM comparison - 15 knots, 1/15 wave slope. 104
5.47 JHSS fine grid: BM comparison - 15 knots, 1/30 wave slope. 104
5.48 JHSS fine grid: BM comparison - 35 knots, 1/30 wave slope. 105
5.49 JHSS refined coarse grid: BM comparison - 15 knots, 1/15 wave slope. 106
5.50 JHSS refined coarse grid: BM comparison - 15 knots, 1/30 wave slope. 106
5.51 JHSS refined coarse grid: BM comparison - 35 knots, 1/30 wave slope. 107
5.52 JHSS rigid body motion comparison for 15 knot, 1/15 wave slope case. 107

LIST OF TABLES

Table

3.1	Mesh quality characteristics for example mesh.	19
3.2	Convergence of box heave motion at $t = 1$ s using different relaxation methods.	31
4.1	Structural grid convergence.	40
4.2	Modal response energy - rigid impact.	41
4.3	Modal convergence of deflection.	43
4.4	Fluid grid convergence	44
4.5	Entry and exit cases	46
5.1	Assessment of accuracy of wave generation and damping.	64
5.2	Wigley hull seakeeping response comparison	70
5.3	Strutural properties of JHSS model backspline.	78

ABSTRACT

A Hydroelastic Method for the Analysis of Global
Ship Response Due to Slamming Events

by

Dominic J. Piro

Chair: Kevin J. Maki

An important aspect of ship design is structural strength. To accurately assess the structural design, the loads experienced by the vessel during its lifetime must be properly understood. Hydroelasticity is the study of conditions where there is a coupled interaction between loads from a dense fluid, such as water, and the response of an elastic structure. Present methods for numerically predicting hydroelastic response either use potential flow models or computational-fluid dynamics (CFD) to model the fluid domain. The potential flow models cannot easily handle an overturning free surface as occurs in slamming, and thus the slamming problem is usually treated separately. The current hydroelastic method uses the accuracy and flexibility of CFD, focusing on efficiency while maintaining numerical stability.

The present fluid-structure interaction solver couples finite-volume CFD with a modal finite-element description of the structure. Predictions of vessel structural response in waves is achieved by combining the structural solver with a large-amplitude rigid-body motion solver. Under-relaxation and iteration are used for stability and accuracy. New stability limits are developed to guide relaxation selection. The solver

is designed to be as efficient as possible, using inertial under-relaxation to reduce the number of iterations and an approximate boundary condition that removes the need for expensive mesh deformation.

Several problems are chosen to validate the present method. Constant velocity elastic wedge impact is used to validate the solver. Then, the role of hydroelasticity is examined for a wedge that enters and exits the water, highlighting that it is important to account for hydroelastic effects when the loading period is relatively small. The validation of the combined rigid-body and structural method is performed with Wigley hull seakeeping and segmented elastic box barge experiments, with the method performing exceptionally well vertical plane motions and bending. The method is demonstrated on the Joint High Speed Sealift (JHSS) segmented model data, a realistic ship geometry. The JHSS model is used to evaluate approximate methods used in industry and show cases when it is important to include hydroelastic effects for a ship in a seaway.

CHAPTER I

Introduction

Accurate structural analysis of ships is important for safety and survivability. In certain conditions, the response of the structure influences the fluid loading on the structure, resulting in a coupled system. The study of this coupling between a dense fluid (water) and an elastic structure is termed hydroelasticity. Hydroelastic effects are often important for the local structural response of ship sections that violently impact the water (known as slamming), and must be taken into account to accurately design the structure. Hydroelastic effects can also be seen in a ship structure in a global sense. If the encountered wave frequency is near the structural natural frequency, a resonance phenomenon known as springing occurs. Local section slamming can also introduce ringing vibrations in the hull, called whipping.

Slamming and the associated whipping response can lead to failure of the ship structure. The failure can be catastrophic, when the stress in the structure exceeds the level that the material can withstand. Predicting whipping response is important for this failure mode, because whipping can add dynamic stress to the structure of the same order of magnitude as the wave induced bending stress. Fatigue failure is also affected by slam-induced whipping. Fatigue damage is correlated with stress ranges and the number of cycles over which the stress occurs. Whipping adds a stress to the structure which has a large amplitude and high frequency (and thus large number of

cycles). Fatigue leads to cracks in the structure which must be repaired or else will lead to more catastrophic failure.

The design of ships is challenging with many interacting aspects, such as cost, propulsion, structural design, operability, manufacturabilty, etc. Hydroelastic effects are usually only considered a small part of the structural design, while they can have a large influence on failure. Therefore, it is important to improve the methods designers used to predict the effect of hydroelasticity early in the design stage (design rules), when there is more ability to make changes, as well as provide high fidelity tools to verify the performance of advanced designs. The structural failure of current vessels, military and commercial, highlights the importance of improving the prediction of hydroelastic effects in design.

Current capabilities in global ship hydroelastic analysis range from modal description of a beam model with strip theory, to computational fluid dynamics (CFD) coupled with full finite-element discretization of the ship structure. Also, there are potential-flow methods that use either the modal model or finite element model for the structure. The strip-theory-hydrodynamic methods do not fully capture three-dimensional effects, while numerical potential-flow methods cannot easily handle wave breaking. Because impact and slamming can lead to an overturning free-surface, the potential-flow methods separate the slamming and global wave bending problems. Due to the expense of computational fluid dynamics simulations, often a one-way coupling is performed, where the ship is rigid in the fluid simulation and an added mass is included in the structural response calculation. The value of this added mass can change with time, especially in extreme conditions, so it is not clear what value should be used. The hydroelastic solver proposed in this work calculates the added mass with full nonlinearity.

A hydroelastic solver has been developed that uses CFD coupled with a modal description of the structure. The coupling is performed in a tightly-coupled manner:

within each time-step, iteration is performed between the solutions to the fluid domain and structure domain. This method allows (with under-relaxation) for the simulation of fluid-structure interaction problems with large fluid added mass that can vary with time. The modal description of the structure reduces the problem into many single degree-of-freedom systems instead of a single large coupled multi-degree-of-freedom system, as well as allows for a reduction of the number of degrees-of-freedom with truncation. The use of inertial under-relaxation allows for fewer iterations to be used than would be possible with explicit under-relaxation, thus contributing to reduced computational time. The use of CFD with volume-of-fluid (VOF) interface capturing is important to solve the global wave-bending and slamming problems together.

In the following sections, Chapter II gives an overview of literature associated with the two main problems of interest: hydroelastic slamming and global ship structural response in waves, specifically related to springing and whipping. Chapter III gives the relevant details on the theory and implementation of the present FSI simulation tool. The solver is applied to two-dimensional elastic wedge-shaped bodies in Chapter IV. The constant velocity elastic wedge impact problem is used as validation, and the new problem of elastic wedge entry and exit is studied. The application of the solver to floating bodies in regular waves is included in Chapter V. Three problems are studied in Chapter V: Wigley hull seakeeping in head seas, an elastic box barge in oblique seas, and the Joint High Speed Sealift (JHSS) segmented model in head seas. Finally a summary and conclusion are given and possible extensions to this work are proposed in Chapter VI

CHAPTER II

Background And Related Work

Vessels that operate in the ocean experience several types of hydroelastic phenomena. This work is focused on numerically predicting structural response to operation in waves with slamming, both locally and globally. Slamming can be defined most generally as a rapid change in wetted surface, which occurs when there is large relative motion between the water surface and the ship combined with large relative velocities. Slamming is experienced by many types of vessels. This includes high-speed planing craft that skip across the tops of waves, and large slower-moving vessels such as cruise ships that may experience slamming when flat sections in the stern of the vessel come in contact with the free surface with large relative velocity. Slamming is important because it can lead to local and global structural failure, either due to fatigue loading or extreme loading in a catastrophic event. Also, slamming can generate unwanted vibration and noise. Thus the study of slamming and the resulting pressure on an elastic body is important to improve the design of marine craft.

2.1 Hydroelastic Impact

Impact, or slamming, is a complicated problem that couples a structure with an air-water fluid flow. Very large fluid pressures can result during impact. The maximum pressure occurs over a small area and moves rapidly along the body. The

fluid flow generates a free surface that may contain a very thin sheet of water, and in general will lead to wave breaking and re-entry of the spray sheet. Also, in many cases there is strong coupling between the fluid and the deformable structure.

Ship slamming has been studied broadly for many decades. The following is a review of references that are particularly important in the development of the current work.

The papers *Kvålsvold and Faltinsen* (1995), *Faltinsen* (1997) and *Faltinsen et al.* (1997) describe theoretical and experimental analysis of the structural response in the wet deck of a multihull during a slamming event. A hydroelastic-beam model is developed to represent the wet deck. In this theory the slamming event is described as occurring during an initial structural-inertia phase, and subsequent free-vibration phase. The fluid flow is represented by a velocity potential that satisfies a body-boundary condition that accounts for structural deformation and forward-speed effects of the vessel. Experimental results are included for the drop of a horizontally-arranged flat plate onto a curved-water surface. Results of structural strain and displacement show strong agreement between the theory and experiment.

In related work, the water entry of a wedge is studied in the paper by *Faltinsen* (1999). Orthotropic-plate theory is used to model the stiffened panel of an aluminum hull catamaran. Comparison of the theoretical and measured strain is made. The amplitude of strain is predicted with reasonable accuracy, although it is difficult to sycronize time-series with the full-scale data as it is impossible to precisely assess the environmental conditions.

A hydroelastic method that uses finite-element analysis to describe the structure of a wedge-shaped body that impacts a calm free surface with constant velocity is presented in *Korobkin et al.* (2006) and *Khabakhpasheva and Korobkin* (2013). In these papers, a Wagner model is used to predict the hydrodynamic solution that accounts for structural deformation. Results are shown for the deformation and stress

in a pinned-pinned beam. The Wagner model is most accurate for bodies that possess a low deadrise angle (small angle between the bottom of the body and the water surface), and the method is used for validation of the present results.

The work presented in *Lu et al.* (2000) studies impact of a wedge with a coupled boundary-element and finite-element method for the fluid and structure, respectively. The structure is modeled with Euler-beam elements, and the fluid is assumed to be described by a velocity potential that satisfies fully-nonlinear free-surface boundary conditions.

The impact of a horizontal plate with a wavy surface is studied in *Korobkin and Khabakhpasheva* (2006). The problem is posed in two spatial dimensions, so that the plate is modeled as a beam. In this paper three different impcact conditions are described: central impact when the ends of the beam are dry and the water touches the interior region, edge impact with one end wet and the other dry, and impact with cavity where both edges are wet but a cavity of air is trapped in the interior. The theory of *Korobkin and Khabakhpasheva* (2006) is compared to experimental measurements and theory that is presented in *Faltinsen* (1997). The comparison of the quantities of strain, displacement, and velocity is excellent during the time period from initial impact until air is drawn under the plate.

Wall et al. (2007) use an Arbitrary Lagrangian-Eulerian (ALE) finite-element approach to model hydroelastic phenomena with a free surface. They study the fluid-structure response of a basin of fluid with a free surface and an elastic arch that is embedded in the bottom of the basin. The deformation of the arch is very large with respect to the other length scales of the problem. The free-surface motion is calculated using a deforming mesh strategy. Their implicit fluid-structure coupling is similar to that which is used in the current work, although the complex free surface encountered in slamming, the problems of interest in the current work, are not easily treated with a deforming-mesh strategy.

Stenius et al. (2010) study idealized hull-water impact using the commercial code LS-DYNA (their method is also described in *Stenius et al.* (2007)). The paper presents results for wedge impact with several end boundary conditions. The influence of longitudinal stiffeners is studied by introducing springs at an interior location of the structure. Finally, they assess the accuracy of several approximations that are commonly made in ship design that greatly reduce the complexity of the analysis, namely, the rigid-quasi-static approach where the structure deforms due to loading predicted by a fluid solution that does not see the structural deformation. Also, the structural inertia is neglected in the rigid-quasi-static approach. Their analysis is useful for the designer to understand the conditions in which the rigid-quasi-static approximation may be used with confidence. *Das and Batra* (2011) also use LS-DYNA to study the impact of composite panels.

Maki et al. (2011) study the constant-velocity impact of an elastic wedge-shaped body using a one-way-coupled simulation method. A finite-volume CFD program that uses VOF for interface capturing solves the fluid solution for a rigid body. The added-mass force due to flexure of the elastic body is found in the structural finite-element software by using acoustical-solid elements in a representative fluid domain. Modal analysis is performed on the finite-element model such that wet mode shapes and frequencies are produced. The one-way transfer of rigid fluid pressure onto a wet modal model of the structure is shown to produce accurate prediction of the maximum stress, although the prediction of the time of maximum stress is less accurate for cases in which the structural deformation becomes large relative to the body-length scale. The current simulation method is tightly coupled such that information between the structure and fluid is exchanged in a time-accurate manner.

The study of the influence of slamming on a fast vessel moving in waves is presented in *Dessi and Mariani* (2006); *Mariani and Dessi* (2012). The authors use both the Wagner and von Karman theory of wedge impact to predict the sectional force on

an elastic-beam model of the ship. The Wagner theory is employed for impact, and the von Karman when a section exits the water. Their theory shows strong agreement with the experimental measurements. These papers also emphasize the importance of the forcing that occurs during the exit stage. The importance of exit on the structural response of two dimensional sections is shown with the current solver in *Piro and Maki* (2011, 2013).

The current method differs from these references by tightly-coupling finite-volume CFD with VOF interface capturing and a modal structure. Of the coupled methods referenced here, none use finite-volume CFD. The use of CFD allows for simulation with a nonlinear fluid and free surface while implicitly handling an overturning free surface. The nonlinear finite element method used in several of the references can also handle the overturning free surface, but that method is not typically used for full ship flows because of aspect ratio requiremts on the mesh.

2.2 Global Vessel Hydroelastic Response

Hydroelastic response of ship hulls is generally categorized in two ways - springing and whipping. Springing is a resonance phenomenon where the encounter frequency matches the ship structural frequency (usually the first bending mode). Whipping describes a ringing phenomenon, when a transient hull vibration is induced by bow or stern slamming. A review of some relevant literature on this topic is included here.

The classic reference for global hydroelastic analysis of marine vessels is the book by *Bishop and Price* (1979). The book uses nonuniform beam theory to describe the structure of ships, and strip theory to describe the hydrodynamics. The structure is decomposed into mode shapes, and the solution for a finite number of modal coordinates is obtained. The analysis includes forward speed effects through encounter frequency, and contains both symmetric response (head/following seas with vertical bending only) and antisymmetric response (oblique/beam seas with torsion and

lateral bending).

Newman (1994) uses a linear panel method for the fluid domain coupled with a modal description for deformable bodies and multiple connected bodies. The method is demonstrated with examples of a flexible barge, bending of a vertical circular cylinder, hinged barge, and vertical cylinder in a channel. The use of orthogonal polynomials is emphasized for structural deflections, instead of the natural modes.

Experiments on a rectangular segmented barge in waves are described in the paper *Š. Malenica et al.* (2003). The experiments are compared to a hydroelastic time-domain method using a Timoshenko-beam finite-element model with vertical bending only. Deflections from the structure are transferred to the fluid mesh, where a potential-flow panel method is used to generate hydrodynamic added mass and damping forces. The frequency-domain representation is converted to the time domain using a convolution-integral technique, allowing for non-linearities such as slamming. For small waves at zero forward speed, deflection Response Amplitude Operators (RAOs) compare well bewteen the experiments and numerical model. The method is extended in *Remy et al.* (2006) to include horizontal bending and torsion. Experiments are used to validate the RAOs generated with the numerical model. Slamming forces are added by *Tuitman and Š. Malenica* (2009) by incorporating a Generalized Wagner Model on two-dimensional sections near the bow. The slamming model is activated when the relative motion and relative velocity predicted by linear seakeeping exceed a pre-defined threshold. The results show how the whipping response associated with slamming events can increase the fatigue damage on ships.

The generalized mode method is used in *Tuitman et al.* (2012) to study both multi-body problems and flexible ship problems. Special consideration is given such that large amplitude, non-linear motions are allowed for the rigid body modes. The viability of the method is demonstrated for Floating Production, Storage, and Offloading (FPSO) unit offloading and for containership whipping. The present work

similarly treats the rigid body modes as generalized modes, but uses fully nonlinear hydrodynamics.

The current method differs from those previously mentioned by incorporating fully nonlinear fluid solutions. Including these nonlinearities directly in the simulation allows for solution of the global wave bending and slamming at the same time. Therefore, any nonlinear interaction between these two aspects can be treated in the present method, but not in those described previously.

A method for predicting global design loads is described in *el Moctar et al.* (2006), *Schellin and el Moctar* (2007), and *Oberhagemann et al.* (2009). The method first uses a frequency domain panel code to generate RAO's of relative motion in slamming-prone locations of a vessel. Then long-term statitistics are used to develop design regular waves to induce the desired relative motion. The design wave is used in Reynolds Averaged Navier Stokes (RANS) simulations (*el Moctar et al.* (2006) and *Oberhagemann et al.* (2009)) or in a non-linear strip theory method (*Schellin and el Moctar* (2007)) to calculate non-linear motion. The pressures from the RANS simulations are applied to finite-element models to predict whipping response in a one-way coupled system. Lewis forms (e.g. see *Bishop and Price* (1979) for formulas) are used to generate added mass that is distributed in the FE model. For the non-linear strip theory, the motion is subsequently used in RANS simulations to obtain design pressures. The pressures are validated with model tests, and compared to design rules. The rules are found to underpredict the results of the simulations, which indicates a need to use coupled FSI methods, such as the current method, to evaluate the applicability of design rules.

The springing phenomenon has been studied using coupled finite element and potential methods in *Kim et al.* (2009, 2013). The fluid domain is modeled using a high-order B-spline Rankine panel method, and the structure using Vlasov-beam finite elements. These elements allow for warping during torsion, important for ships

with large deck openings, such as container ships. The method uses under-relaxation to stabilize the fluid-structure system, similar to the present work. The RAO's of vertical bending moment are calculated for both a rigid and elastic S175 container ship, where the rigid ship prediction does not capture the response at resonance. This indicates that the flexural modes provide a method of energy dissipation, even for the rigid body motion, and thus using a tightly coupled method can be important when the encounter frequency is near the vessel rigid body natural frequencies.

One-way and two-way coupled global hydroelastic simulations are performed in *Paik et al.* (2009) on a S175 containership. The structure is defined by a finite element model and decomposed into modes. The one-way coupling uses acoustic finite elements to model added mass effects on the ship. The two-way coupled simulations deform an overset mesh around the ship to match the calculated deflection. The two methods are compared to experimental data for the S175 container ship. The two-way coupled simulations predict the frequency and phase of the experimental bending moments well, but overpredict the sagging moment.

Two-way coupled simulations are preformed in *el Moctar et al.* (2011) using finite volume CFD with volume of fluid interface capturing and a Timoshenko beam model. The method is shown to be able to predict midship vertical bending moment response in irregular seas. The paper concludes that the computational time required for the method limits its applicability to real problems. The current work aims to improve the speed of similar calculations to increase their usefulness, as well as allow for more complex structures than simple beam models.

A probabilistic hydroelastic method is developed for very large floating structures by *Papaioannou et al.* (2013). The method uses the boundary element method to develop the hydrodynamic mass, stiffness, and damping for the structural degrees of freedom. The structure is described by a plate and discretized using finite elements to develop the mode shapes. The method is demonstrated using several numerical

examples for multi-directional seas.

The current work expands the field of tightly-coupled fluid-structure interaction simulation of ships in a seaway using CFD, which is currently described in a small body of work. The use of nonlinear fluid solvers is important for the slamming problem and for combining it with the global wave-bending problem, while for much of the previous work in the area, they slamming and global wave problems have been separated. The present method is focused on improving efficiency while maintaining accuracy and stability, such that the method is a usable late-stage design tool or practical to provide high-fidelity information for the development of future design rules.

CHAPTER III

Fluid-Structure Interaction Solver

3.1 Introduction

This chapter describes the details of the tightly-coupled FSI solver, which is an expanded version of the solver first described in *Piro and Maki* (2013). Since that paper, the rigid-body motion solver and inertial under-relaxation have been added. First the use of CFD on the fluid domain is described. Then the solution process of the structural as well as rigid body motion is discused. Finally, the coupling algorithm is described, with emphasis on the under-relaxed iteration and exchange of data between the fluid and structure domains.

3.2 Fluid Domain Solution

The fluid-structure interaction solver uses CFD to solve for the flow in the fluid domain. A finite-volume discretization is used with arbitrary Lagrangian-Eulerian (ALE) formulation - found in *Jasak* (2009) - to allow for moving and deforming grids. The fluid is assumed to be laminar and incompressible. The laminar assumption is made because turbulence is not expected to have time to develop during a slamming event and thus have a significant effect on the hydroelastic response. Thus the additional complexity of turblence models is not included. However, analysis of

this assumption is a possible extension of this work. The fluid is governed by the Navier-Stokes equations:

$$\nabla \cdot \vec{u} = 0, \tag{3.1}$$

$$\frac{\partial \rho \vec{u}}{\partial t} + \nabla \cdot \rho \vec{u}\vec{u} = -\nabla p + \nabla \cdot \left[\mu(\nabla \vec{u} + \nabla \vec{u}^T)\right] + \rho \vec{g}, \tag{3.2}$$

where $\vec{u}$ is the fluid velocity, ρ and μ the fluid density and dynamic viscosity, p the fluid pressure, and $\vec{g}$ the acceleration due to gravity.

The nature of free-surface hydroelastic phenomena requires solution of the position of the free-surface. The slamming problems that are studied in this work have complex evolution of the free surface during the impact and exit stages. In order to efficiently solve for the nonlinear and complex free surface, the volume-of-fluid interface-capturing technique is used. The VOF method is widely used; for example, see *Ubbink and Issa* (1999) for VOF on an arbitrary unstructured finite-volume discretization of the fluid domain. The VOF method combines the properties of the two fluids - air and water - into a single, continuous fluid using the volume fraction variable α, as shown here:

$$\rho(\vec{x}, t) = \rho_{\text{water}} \alpha(\vec{x}, t) + \rho_{\text{air}}(1 - \alpha(\vec{x}, t)), \tag{3.3}$$

$$\mu(\vec{x}, t) = \mu_{\text{water}} \alpha(\vec{x}, t) + \mu_{\text{air}}(1 - \alpha(\vec{x}, t)). \tag{3.4}$$

Combining the VOF equation for density and the conservative form of the transport equation for α:

$$\frac{\partial \alpha}{\partial t} + \nabla \cdot (\alpha \vec{u}) + \nabla \cdot (\alpha(1 - \alpha)\vec{u}_r) = 0. \tag{3.5}$$

The last term on the left hand side applies the artificial compressive velocity $\vec{u}_r$ to sharpen the interface and is only active in the vicinity of the interface due to the $\alpha(1 - \alpha)$ term.

The OpenFOAM CFD library is used to solve equations on arbitrary-polyhedral

discretization of the fluid domain. The unknowns are stored using a collocated arrangement at the geometric center of each cell. The discretizaton error of all terms in space and time is second order.

3.3 Structural Domain

3.3.1 Modal Decomposition

The structural domain is modeled using a finite number of mode shapes and associated natural frequencies. Modal theory is based upon linear superposition, and thus assumes small displacements and rotations. For many metallic marine structures, this small displacement approximation is suitable. The natural frequencies are obtained in a vacuum because the influence of the fluid is accounted for as an external force on the structure. The orthogonality of the mode shapes allows for decoupling of the structural equations of motion, giving the normal equations of motion shown below in Equation (3.6).

$$[I]\{\ddot{q}\} + [2\zeta\omega_n]\{\dot{q}\} + [\omega_n^2]\{q\} = \{f\}, \tag{3.6}$$

where $[I]$ is the identity matrix, $[\omega_n^2]$ is a diagonal matrix of the natural frequencies, $[2\zeta\omega_n]$ is the modal viscous damping matrix (assumed proportional damping), $\{q\}$ is the vector of the modal amplitudes, and $\{f\}$ is the vector of the modal forces. Note that while the modes may become coupled hydrodynamically, the coupling is on the right hand side of the equations and thus does not affect the solution procedure. The main advantage of using a modal model to describe the structure is that only a small number of degrees-of-freedom, typically less than 100, are necessary to solve and accurately represent the response of the structure. For reference, the number of degrees-of-freedom used in industrial applications for modeling entire ships is above 100,000.

The structural mode shapes and frequencies can be generated analytically for

simple geometries. Beam and plate theories give continuous representations of the mode shapes, but are only feasible for structures consisting of a single beam or plate. For more realistic structures, numerical methods provide a more feasible means of creating the modal basis. The most common discretization strategy in structural analysis is the finite-element method, which is used in this work, as discussed in Section 3.3.2.

The modal viscous damping can be generated either with a propotional damping matrix, or entered as structural damping. Proportional damping occurs when the damping matrix can be written as a linear combination of the mass and stiffness matricies. Structural damping, also called hysteretic damping, is modeled in the frequency domain as $\{f_d\} = -i\eta[\omega_n^2]\{q\}$, where η is the loss coefficient. The imaginary term causes difficulty when incorporating structural damping in the time domain. An approximate modal viscous damping coefficient which equates two damping models at the natural frequencies as in *Henwood* (2002) uses a constant value of $\zeta = \eta/2$ for all modes.

The equations of motion are solved using a state-space representation, shown in Equation (3.7). This representation allows for the use of standard ODE solution methods.

$$\frac{d}{dt}\begin{Bmatrix} \{q\} \\ \{\dot{q}\} \end{Bmatrix} = \begin{bmatrix} 0 & [I] \\ -[\omega_n^2] & -[2\zeta\omega_n] \end{bmatrix} \begin{Bmatrix} \{q\} \\ \{\dot{q}\} \end{Bmatrix} + \begin{Bmatrix} 0 \\ \{f\} \end{Bmatrix}. \tag{3.7}$$

Presently, the time derivative is approximated with a second-order (three time level)

finite differencing scheme, and the structural terms are treated implicitly, shown here:

$$a_0 \begin{Bmatrix} \{q\} \\ \{\dot{q}\} \end{Bmatrix}^{n+1} + a_1 \begin{Bmatrix} \{q\} \\ \{\dot{q}\} \end{Bmatrix}^{n} + a_2 \begin{Bmatrix} \{q\} \\ \{\dot{q}\} \end{Bmatrix}^{n-1} = \begin{bmatrix} 0 & [I] \\ -[\omega_n^2] & -[2\zeta\omega_n] \end{bmatrix} \begin{Bmatrix} \{q\} \\ \{\dot{q}\} \end{Bmatrix}^{n+1} + \begin{Bmatrix} 0 \\ \{f\} \end{Bmatrix}, \quad (3.8)$$

where $a_0 = (\Delta t^n + 2\Delta t^{n+1})/(\Delta t^{n+1}(\Delta t^n + \Delta t^{n+1}))$, $a_1 = -(\Delta t^n + \Delta t^{n+1})/(\Delta t^n \Delta t^{n+1})$, $a_2 = \Delta t^{n+1}/(\Delta t^n(\Delta t^n + \Delta t^{n+1}))$, Δt^{n+1} is the time interval between time steps n and $n+1$, and Δt^n between $n-1$ and n. Equations (3.7) and (3.8) has a large bandwidth, and thus are rearraged to contain 2x2 blocks for each mode that can be solved independently.

3.3.2 Finite Element Modeling

For the complicated structural arrangements in marine vessels, finite-element modeling (FEM) is an efficient method to handel the complex geometry. The finite-element method is a discretization strategy which divides the structure into small pieces (elements) that connect points (nodes). Each node typically contains six degrees of freedom - three translations and three rotations. Many different element types have been developed with different levels of approximation, including one-dimensional beams and two-dimensional plates.

The finite element models in the current work are developed using an in-house three-dimensional modeling program. The program is written in the Java programming laguage for the ease of GUI (Graphical User Interface) development. The geometry of the structure is first defined, either using the program's entities or by importing IGES files from another three-dimensional modeling program. A focus of the geometry development has been the generation of quality surface meshes, espe-

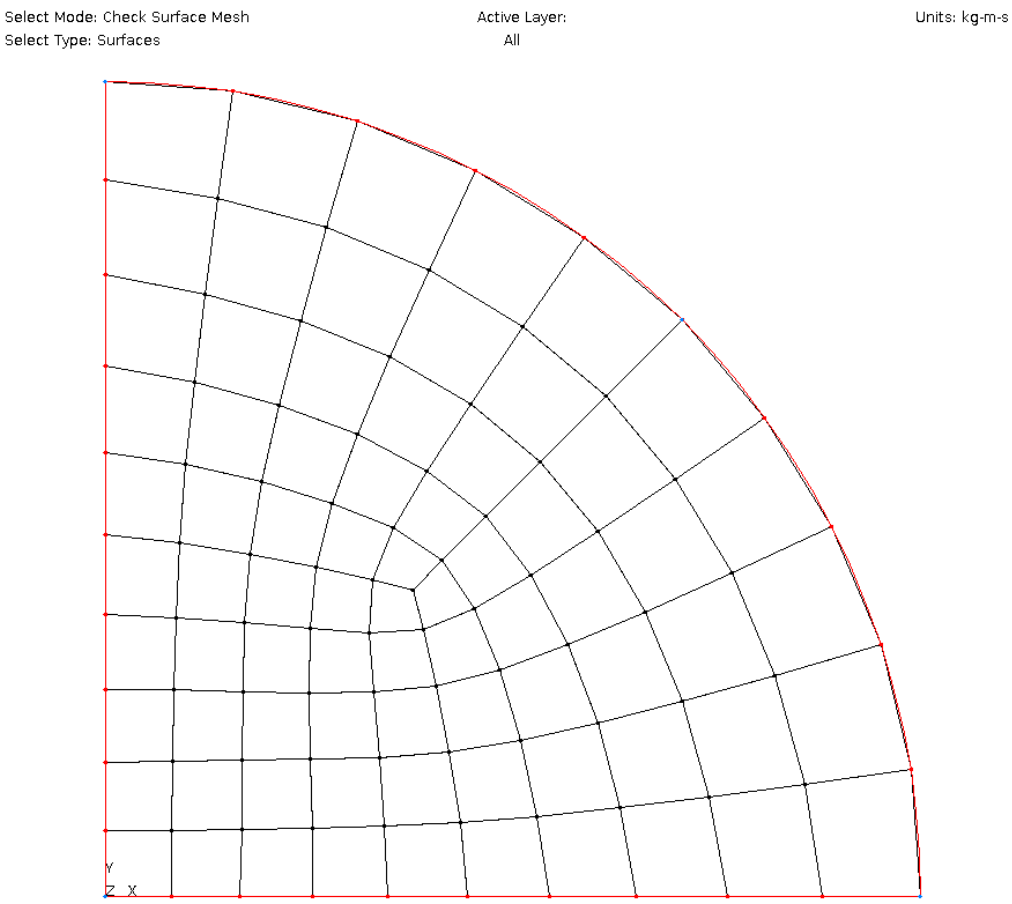

Figure 3.1: Example of surface meshing with a quarter circle. The mesh maintains all quadrilateral elements with good aspect ratio and skewness properties (see Table 3.1).

cially for non-rectangular domains. For example, the quarter circle surface shown in Figure 3.1 has three edges but quadrilateral elements are maintained. A table of mesh quality metrics for this example is shown in Table 3.1. The emphasis on quadrilateral elements is based on the loss of accuracy when using triangular plate elements.

The geometry is then used to generate the finite element model. Nodes are created at the mesh points, and the elements are created based upon the geometry type. One-dimensional elements - trusses, beams, and frames - are meshed on curves, which can be lines, arcs, or splines. Surfaces are used to create two-dimensional elements, either membranes, plates, or shells. Most of the element definitions are obtained from

Metric	min	ave	max	target
aspect ratio	1.01175	1.14933	1.39943	< 3
skew	0.07990	2.69468	9.38625	< 45
Jacobian	0.98737	0.99657	0.99999	> 0.6

Table 3.1: Mesh quality characteristics for example quarter circle mesh.

standard FEM references, such as *Chandrupatla and Belegundu* (2002); *Shames and Dym* (2003). The exceptions are described below.

When developing finite element formulations, a standard method for calculating element mass and stiffness matricies ($[M_e]$ and $[K_e]$) is to start from the kinetic and potential (strain) energies, T_e and U_e respectively. Shape functions are used to interpolate nodal displacements $\{\delta_e\}$ to continuous displacements internal to the element. Thus the kinetic energy becomes

$$T_e = \frac{1}{2}\{\dot{\delta_e}\}^{\mathrm{T}}[M_e]\{\dot{\delta_e}\}, \tag{3.9}$$

and the potential energy becomes

$$U_e = \frac{1}{2}\{\delta_e\}^{\mathrm{T}}[K_e]\{\delta_e\}. \tag{3.10}$$

If the governing equations for the element are known, variational calculus can be used to determine the kinetic and potential energy.

The current Timoshenko beam and frame elements are based on the work of *Friedman and Kosmatka* (1993). Timoshenko beam theory differs from Euler-Bernoulli beam theory (used in the regular beam elements) in that while plane sections remain planar, they are not required to remain normal to the beam reference line by incorporating shear deformation. The equations of motion for Timoshenko beam theory

are shown in Equations (3.11) and (3.12).

$$\rho A\ddot{w} + \frac{\partial}{\partial x}\left[kGA\left(\frac{\partial w}{\partial x} + \psi\right)\right] = 0, \tag{3.11}$$

$$\rho I\ddot{\psi} - \frac{\partial}{\partial x}\left[EI\frac{\partial \psi}{\partial x}\right] + kGA\left(\frac{\partial w}{\partial x} + \psi\right) = 0, \tag{3.12}$$

where ρ, E, and G are the material density, Young's modulus, and shear modulus; A and I the cross-sectional area and area moment of inertia; and k is a factor for the shear stiffness, with $k = 10(1+\nu)/(12+11\nu)$ (from *Friedman and Kosmatka* (1993)) for this work (ν is Poisson's ratio). The displacement w is interpolated with cubic shape functions, and rotation ψ with quadratic shape functions.

Quadrilateral plate elements are developed using an isoparametric basis: an arbitrary quadrilateral is mapped to a square in the ξ-η plane defined by $-1 \leq \xi \leq 1$ and $-1 \leq \eta \leq 1$. Bi-cubic shape functions are used for interpolation of the displacement w, which satisfies the linear plate equation:

$$\rho h\ddot{w} + D\nabla^4 w = 0, \tag{3.13}$$

where ρ is the matrial density, D is the bending stiffness term with $D = Eh^3/12/(1+\nu^2)$, h is the plate thickness, and ∇^4 is the bi-harmonic opperator, $\nabla^4() = \nabla^2(\nabla^2())$. Gaussian quadrature with three-by-three points is used to perform the integration for the stiffness matrix and four-by-four points for the mass matrix. Triangular elements are created as degenerated quadrilaterals - the third and fourth nodes are the same. However, the triangular elements are not as accurate as quadrilaterals.

Quadrilateral shell elements use the plate elements described above combined with membrane elements described in *Iura and Atluri* (1992). The membrane component includes the so-called drilling degree of freedom - rotation about the element normal. The drilling stiffness is important for linking shell elements that are not on the same

plane, such as along a curved surface. The strain energy of the element is described by:

$$U_m = \int \left[\frac{E}{2(1-\nu^2)} \left(\left(\frac{\partial u}{\partial x} \right)^2 + \left(\frac{\partial v}{\partial y} \right)^2 + 2\nu \frac{\partial u}{\partial x} \frac{\partial v}{\partial y} \right) + \frac{G}{2} \left(\frac{\partial u}{\partial y} + \frac{\partial v}{\partial x} \right)^2 \right] dV, \tag{3.14}$$

$$U_d = \int \left[\chi \frac{G}{2} \left(\theta + \frac{1}{2} \frac{\partial u}{\partial y} - \frac{1}{2} \frac{\partial v}{\partial x} \right)^2 \right] dV, \tag{3.15}$$

$$U_b = \int \left[\frac{Ez^2}{2(1-\nu^2)} \left(\left(\frac{\partial^2 w}{\partial x^2} \right)^2 + 2\nu \frac{\partial^2 w}{\partial x^2} \frac{\partial^2 w}{\partial y^2} + \left(\frac{\partial^2 w}{\partial y^2} \right)^2 + 4(1-\nu) \left(\frac{\partial^2 w}{\partial x \partial y} \right)^2 \right) \right] dV, \tag{3.16}$$

where U_b, U_m and U_d are the bending, membrane, and drilling strain energies. The in-plane displacements are u and v, the out of plane displacement is w, and θ is the in-plane rotation. The factor χ is used to scale the drilling stiffness, and according to *Iura and Atluri* (1992) should be between 0 and 100, with $\chi = 1$ typically used. The kinetic energy of the shell element is given by:

$$T = \int \frac{\rho}{2} \left[u^2 + v^2 + k_z \theta^2 + w^2 \right] dV, \tag{3.17}$$

where k_z is the radius of gyration of the element about its normal. Bi-linear shape functions are used for the in-plane degrees of freedom and bi-cubic for the out-of-plane degrees of freedom.

In segmented ship experimental models, the shell of the model consists of rigid sections and the structure is provided by a beam, known as a backbone or backspline. To compare the present method with such experiments, a consistent numerical modeling approach is required. Therefore, elements are created which simply project the motion of the structure onto a line or plane. These are labeled "transfer elements". The displacements are projected in a linearized fashion in order to properly transfer the mode shapes. As an example, the transfer equations for an Euler space frame

(includes axial deformation, bending in two directions, and torsion) are show here:

$$\begin{Bmatrix} d_x(x,y,z,t) \\ d_y(x,y,z,t) \\ d_z(x,y,z,t) \\ \theta_x(x,y,z,t) \\ \theta_y(x,y,z,t) \\ \theta_z(x,y,z,t) \end{Bmatrix} = \begin{Bmatrix} u(x,t) - \frac{dv(x,t)}{dx}y - \frac{dw(x,t)}{dx}z \\ v(x,t) - \phi(x,t)z \\ w(x,t) + \phi(x,t)y \\ \phi(x,t) \\ -\frac{dw(x,t)}{dx} \\ \frac{dv(x,t)}{dx} \end{Bmatrix}, \tag{3.18}$$

where d_x, d_y, and d_z are the projected displacements in the x, y, and z directions; θ_x, θ_y, and θ_z the projected rotations; $u(x,t)$ is the axial displacement of the frame; $v(x,t)$ is the y displacement; $w(x,t)$ is the z displacement; and $\phi(x,t)$ is the torsional rotation. The x, y, and z axes here are the local axes for the frame element. The displacements are subsequently rotated into the global coordinate system for the transfer element. As an example of how the transfer elements are used, Figure 3.2 shows how a segmented box barge is modeled. The backbone is modeled with space frame elements, and the barge is meshed with transfer shell elements.

In addition to the finite elements, simple spring and mass elements are available. The springs can either be translational springs that connect two nodes or rotational springs that add stiffness to one node. Both point and distributed masses are available, with the ability to offset the mass from the node it is connected to. This offset causes additional rotational inertia at the node, as well as coupling between translational and rotational degrees of freedom.

The finite elements, as well as springs and masses, are used to generate global mass and stiffness matricies $[M]$ and $[K]$, but currently not a damping matrix. These are used in the matrix equation of motion for the degrees of freedom $\{\delta\}$:

$$[M]\{\ddot{\delta}\} + [K]\{\delta\} = \{F\}. \tag{3.19}$$

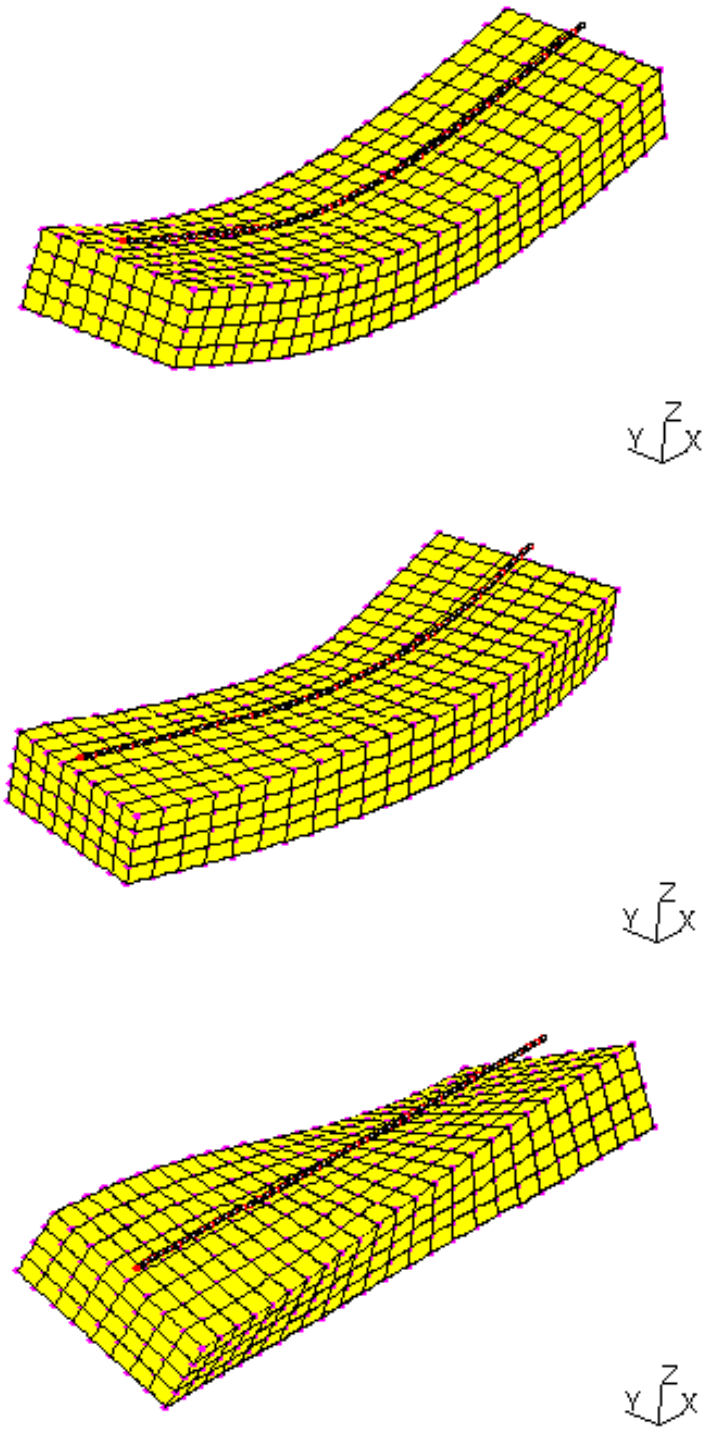

Figure 3.2: Example of transfer elements for a segmented box barge, showing vertical bending (top), horizonal bending (middle), and torsional (bottom) mode shapes. The backbone is orange and the transfer elements are yellow.

The assumption of harmonic motion in vacuum leads to the eigenvalue problem

$$[K]\{\Phi\} = \omega^2[M]\{\Phi\}, \tag{3.20}$$

where the eigenvector $\{\Phi\}$ is a mode shape. If all of the mode shapes are combined into one matrix $[\Phi]$, the left hand side of the equation of motion can be diagonalized by:

$$[\Phi]^{\mathrm{T}}[M][\Phi]\{\ddot{q}\} + [\Phi]^{\mathrm{T}}[K][\Phi]\{q\} = [\Phi]^{\mathrm{T}}\{F\}, \tag{3.21}$$

using $\{\delta\} = [\Phi]\{q\}$. Comparing this to Equation (3.6), the mode shapes must be scaled such that $[\Phi]^{\mathrm{T}}[M][\Phi] = [I]$ and $[\Phi]^{\mathrm{T}}[K][\Phi] = [\omega_n^2]$. A damping matrix is not included in the current finite element analysis, but could be as long as the damping is proportional to the mass and stiffness matricies. Currently, damping is added only to the coupled model. Internal structural damping can be approximated by viscous damping, as mentioned above.

The Java application uses the dense and sparse matrix libraries `lapack` and `arpack` modified for use with Java, offered by Netlib. The eignvalue solver `DSYGV` from `lapack` is used for the dense matricies, and the routines `DSAUPD`, `DSEUPD`, and `DAXPY` from `arpack` to extract eignvalues and eignvectors for sparse matricies. The calculated eigenvalues and eigenvectors are used to generate the natural frequencies and mode shapes of the structure. The application then writes out the structural information in the proper format for the coupled FSI solver. This is one of the main advantages of using the Java application: there is control over the interaction between the FEM and CFD codes.

3.4 Rigid Body Motion

The rigid body motion of the vessel is treated differently from the structural deformation to allow for large displacements and rotations for the rigid body while

maintaining the small displacement approximations for the deformation. The time discretization of the rigid body motion is achieved with either second-order backwards differencing or first or second-order symplectic integration, which conserves energy and is well suited for long-time integration. The discrete equations for translational motion with first order time discretization are:

$$\vec{v}^{n+1} = \vec{v}^{n} + \Delta t^{n+1} \frac{\vec{F}^{n}}{m}, \tag{3.22}$$

$$\vec{x}^{n+1} = \vec{x}^{n} + \Delta t^{n+1} \vec{v}^{n+1}, \tag{3.23}$$

and with second-order discretization:

$$a_0 \vec{v}^{n+1} + a_1 \vec{v}^{n} + a_2 \vec{v}^{n-1} = \frac{\vec{F}^{n}}{m}, \tag{3.24}$$

$$a_0 \vec{x}^{n+1} + a_1 \vec{x}^{n} + a_2 \vec{x}^{n-1} = \vec{v}^{n+1}, \tag{3.25}$$

where n and $n-1$ denote values at the previous time steps, $n+1$ denotes a value at the new time step, $\vec{x}$ is the position, $\vec{v}$ is the velocity, $\vec{F}$ is the external force (from the CFD solution), m is the mass, and the coefficents a_0, a_1, a_2, and Δt^{n+1} are the same as in Equation (3.8). The update equations for the rotational degrees of freedom are (first-order):

$$\vec{\omega}^{n+1} = \vec{\omega}^{n} + \Delta t^{n+1} [I_{\mathrm{CM}}]^{-1} \vec{M}^{n}, \tag{3.26}$$

$$\vec{\theta}^{n+1} = \vec{\theta}^{n} + \Delta t^{n+1} \vec{\omega}^{n+1}, \tag{3.27}$$

and the second-order equations are:

$$a_0 \vec{\omega}^{n+1} + a_1 \vec{\omega}^{n} + a_2 \vec{\omega}^{n-1} = [I_{\mathrm{CM}}]^{-1} \vec{M}^{n}, \tag{3.28}$$

$$a_0 \vec{\theta}^{n+1} + a_1 \vec{\theta}^{n} + a_2 \vec{\theta}^{n-1} = \vec{\omega}^{n+1}, \tag{3.29}$$

where $\vec{\theta}$ is the vector of rotations, $\vec{\omega}$ the rotational velocities, $[I_{\mathrm{CM}}]$ the inertia tensor about the center of mass, and $\vec{M}$ the external moment.

The advantage to second-order time integration is an increase in accuracy over first-order for a given time-step size. The disadvantages are the extra variables to store (Δt^n, $\vec{x}^{n-1}$, etc.) and the need for an additional inital condition. The extra memory to store is very small, one scalar and four vectors, and thus does not pose problems. The additional initial condition is not usually a problem, as the body is usually starting from rest (in which case the state is constant before the start) or the initial transient response is not the primary objective, rather the fully developed solution is of interest. Therefore, second-order integration is used for the rigid-body motion in this work.

3.5 Coupling of Fluid and Structure Domains

3.5.1 Under-Relaxation and Iterative Algorithm

The fluid, rigid body, and structure domains are numerically solved in a tightly-coupled algorithm. At each time step the fluid and structure domains are solved sequentially in an iterative manner. During each iteration, the rigid body position and structural deformation are updated using the fluid stress from the previous iteration. Then, the fluid variables are solved using updated rigid body position and structural deflection. Due to the differing time scales of the hydroelastic problems that are considered in this work, and the segregated nature of the FSI equations, iteration and under-relaxation are necessary to ensure convergence to a solution. Two types of under-relaxation are used in this work, explicit and inertial.

The explicit under-relaxation method employed in this work uses the parameter β_r to control the change in the state vector X at an intermediate iteration as:

$$X_{i+1}^{n+1} = (1 - \beta_r) X_i^{n+1} + \beta_r \tilde{X}_{i+1}^{n+1}, \tag{3.30}$$

where $\tilde{X}$ is the unrelaxed update, n is the time step, and i is the iteration counter.

If only explicit under-relaxation is used, the selection of the under-relaxation parameter and number of iterations is important so that convergence is achieved with a minimal number of iterations. The tightly-coupled algorithm is very similar to many present in the literature, and selection of the under-relaxation parameter for hydroelastic problems is similar to the procedure described in *Causin et al.* (2005), where they provide an algorithm for hemodynamics.

The description of the procedure to select the under-relaxation parameter is most clearly developed by considering a single degree-of-freedom in the structural equations-of-motion (Equation 3.6). X denotes the state vector of a single degree-of-freedom, which consists of the modal coordinate and velocity, $X = \begin{bmatrix} q & \dot{q} \end{bmatrix}^T$. The update to the next time step (from n to $n+1$) without relaxation is given in Equation 3.31:

$$\tilde{X}^{n+1} = [H]X^n + \begin{pmatrix} 0 \\ \Delta t f \end{pmatrix}, \tag{3.31}$$

where f is the modal force and $[H]$ is a matrix that maps the state values from the previous time step to the current time step. $[H]$ is determined by the time-discretization scheme.

The selection of the under-relaxation parameter is very important with respect to the convergence and accuracy of the algorithm. As β_r becomes smaller, a greater number of iterations over the fluid-structure system become necessary to reach a converged solution at the new time level. Thus it is important to find the stability limit $\beta_r \leq \beta_{max}$, and set β_r close to the limit. Also, it is important to know how many iterations are required such that the solution at the new time level is converged.

The optimal value of the under-relaxation factor can be estimated with information about the stability of the update equation for the state vector (Equation 3.30). The modal force is considered to be composed of both an added-mass component

and a purely time-dependent force, as shown in Equation 3.32. Here, γ is the modal-added-mass coefficient.

$$f = -\gamma\ddot{q} + \tilde{f}. \tag{3.32}$$

The modal acceleration in Equation 3.32 is approximated with a finite difference as $\ddot{q} \cong (\dot{q}_i^{n+1} - \dot{q}^n)/\Delta t$. This approximation is only first-order accurate, but its use is only for the purpose of estimating the required value of the under-relaxation factor, and is good for small Δt.

This expression for the modal force may be combined with Equations 3.31 and 3.30 to yield the under-relaxed update equation:

$$X_{i+1}^{n+1} = (1-\beta_r)X_i^{n+1} + \beta_r \left([H']X^n + \begin{bmatrix} 0 & 0 \\ 0 & -\gamma \end{bmatrix} X_i^{n+1} + \begin{pmatrix} 0 \\ \Delta t\tilde{f} \end{pmatrix} \right). \tag{3.33}$$

Note that $[H]$ becomes $[H']$ with the contribution from the velocity at the old time level present in the approximation of the acceleration. To determine the stability of the method, the terms from the previous iteration (X_i^{n+1}) are collected into a matrix, shown in Equation 3.34. The eigenvalues of this matrix must have a magnitude less than one for the iteration to be stable.

$$X_{i+1}^{n+1} = \begin{bmatrix} 1-\beta_r & 0 \\ 0 & 1-(1+\gamma)\beta_r \end{bmatrix} X_i^{n+1} + \beta_r \left([H']X^n + \begin{pmatrix} 0 \\ \Delta t\tilde{f} \end{pmatrix} \right). \tag{3.34}$$

This gives a requirement on the under-relaxation factor of $0 \leq \beta_r \leq 2/(1+\gamma)$.

This procedure now transfers the burden of determining the required under-relaxation factor to the task of estimating the largest value of the modal-added-mass coefficient, γ. In the example of two-dimensional wedge-shaped sections, ideal-fluid calculations are performed for a vibrating beam structure in a deeply submerged fluid. The first mode shape provides the largest added-mass coefficient because there are

cancellation-like effects at the higher modes. Typical values for γ for the first mode shape of a pin-pin beam submerged in water range from a factor of 6 to 20 of the structural modal mass. This leads to the requirement for the maximum β_r to be in the range of 0.28 to 0.095.

The other under-relaxation method used in this work is labeled inertial under-relaxation. This method is similar to methods presented by *Sun and Faltinsen* (2011) and *Young et al.* (2012). As shown above, solving for the fluid added mass explicitly on the right-hand-side of the equation of motion of the structure causes instability in the FSI system. Therefore, inertial under-relaxation applies an estimate of the added mass force to the left and right-hand-sides of the equation. On the left-hand-side the effective mass of the system is increased with an estimate of the added mass. This same estimated added mass is used on the right-hand-side with an estimate of the acceleration ($\{\ddot{q}_{\text{est}}\}$). The equations of motion for the structural system become:

$$([I] + [\Gamma_e])\{\ddot{q}\} + [2\zeta\omega_n]\{\dot{q}\} + [\omega_n^2]\{q\} = \{f\} + [\Gamma_e]\{\ddot{q}_{\text{est}}\} \tag{3.35}$$

where $[\Gamma_e]$ is the estimated modal added mass matrix. If this matrix is not diagonal, the degrees of freedom become coupled and must be solved together. This additional expense is not large compared to the cost of solving the fluid system, even if a large number ($\mathcal{O}(100)$) of modes are used.

If inertial under-relaxation is used in conjunction with explicit under-relaxation, the effect on stability can be seen with a modified requirement on the under-relaxation factor. The equation of motion for a single degree of freedom system with inertial under-relaxation is given by

$$(1 + \gamma_e)\,\ddot{q} + 2\zeta\omega_n\dot{q} + \omega_n^2 q = f + \gamma_e\ddot{q}_{est}. \tag{3.36}$$

The iteration update equation is still the same as before with explict under-relaxation,

given by Equation 3.30. Equation 3.31 changes to Equation 3.37.

$$\tilde{X}^{n+1} = [H]X^n + \begin{pmatrix} 0 \\ \Delta t \frac{f+\gamma_e \ddot{q}_{est}}{1+\gamma_e} \end{pmatrix}. \tag{3.37}$$

The force is again decomposed into an added mass component and everything else, as in Equation 3.32, and the same approximation is applied to the acceleration. The new relaxed update equation becomes:

$$X_{i+1}^{n+1} = (1-\beta_r)X_i^{n+1} + \beta_r \left([H']X^n + \begin{bmatrix} 0 & 0 \\ 0 & -\frac{\gamma-\gamma_e}{1+\gamma_e} \end{bmatrix} X_i^{n+1} + \begin{pmatrix} 0 \\ \Delta t \frac{\tilde{f}}{1+\gamma_e} \end{pmatrix} \right). \tag{3.38}$$

Collecting the terms for the the previous iteration (X_i^{n+1}) yeilds:

$$X_{i+1}^{n+1} = \begin{bmatrix} 1-\beta_r & 0 \\ 0 & 1-\left(1+\frac{\gamma-\gamma_e}{1+\gamma_e}\right)\beta_r \end{bmatrix} X_i^{n+1} + \beta_r \left([H']X^n + \begin{pmatrix} 0 \\ \Delta t \tilde{f} \end{pmatrix} \right). \tag{3.39}$$

The stability requirement that the magnitudes of the eigenvalues of the update matrix must be less than or equal to one yeilds:

$$0 \leq \beta_r \leq \frac{2}{1+\frac{\gamma-\gamma_e}{1+\gamma_e}}. \tag{3.40}$$

In this form it appears that the difference between the actual and estimated added mass is what drives stability. However, if the numerator and denomiator of the right hand term are multiplied by $1+\gamma_e$, the requirement becomes:

$$0 \leq \beta_r \leq \frac{2\,(1+\gamma_e)}{1+\gamma_e+(\gamma-\gamma_e)} = \frac{2\,(1+\gamma_e)}{1+\gamma}. \tag{3.41}$$

This limit suggests that inertial under-relaxation can only stabilize the system, and if the estimated added mass is chosen properly, no explicit under-relaxation is re-

	Implicit pos.	Implicit vel.	Explicit pos.	Explicit vel.
itr. 1	-1.84482	-0.160532	-1.91301	-0.244504
itr. 2	-1.84483	-0.160897	-1.91370	-0.253739
itr. 3	-1.84483	-0.161056	-1.91380	-0.235781
itr. 4			-1.91382	-0.226829
itr. 5			-1.91382	-0.223298
itr. 6			-1.91382	-0.222018

Table 3.2: Convergence of box heave motion at $t = 1$ s using different relaxation methods.

quired and fewer iterations can be used. Another way to examine the inertial under-relaxation stability limit is to examine it without explicit under-relaxation. Therefore, taking the above requirement with $\beta_r = 1$, the requirement $\gamma_e \geq (\gamma - 1)/2$ is obtained.

As a demonstration of the different relaxation techniques, a simple case of a box dropped into water is used. A coarse mesh of 26,000 cells is used for the evaluation. Second order time integration is used for this demonstration. Figure 3.3 shows three snapshots of the box as it is dropped into the water, using inertial under-relaxtion and three iterations. This simulation is compared to one with explicit under-relaxation and six iterations. The heave motion of the box is compared between the two simulations in Figure 3.4. As can be seen, the simulation with inertial under-relaxation damps out more rapidly than that with explicit. The cpu time with explicit under-relaxation (4328 s) is about double that with implicit under-relaxation (2094 s), as would be expected with twice as many iterations per time-step. Table 3.2 shows the convergence of the motion (position and velocity) for the two methods at time $t = 1$ s, when the added mass should be greatest. For both methods, the position has clearly converged within six significant figures. For the velocity, the difference between the second to last and last iterations is about 0.1% with implict under-relaxation and 0.6% with explict under-relaxation. Therefore, even with half as many iterations, the simulation with implicit under-relaxation has converged better.

The explicit under-relaxation strategy is used in the early results with the FSI

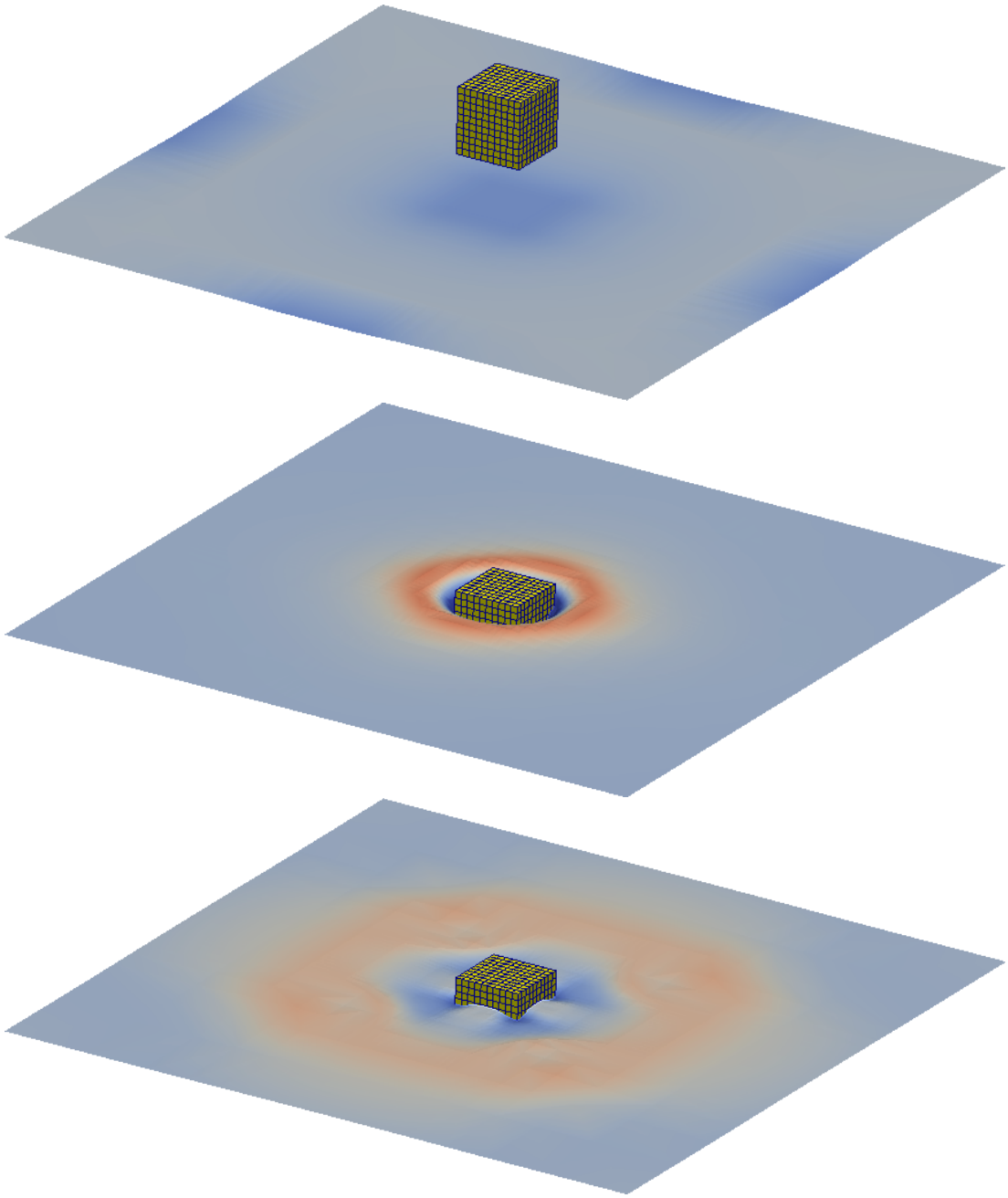

Figure 3.3: Test box dropping into the water and subsequently floating.

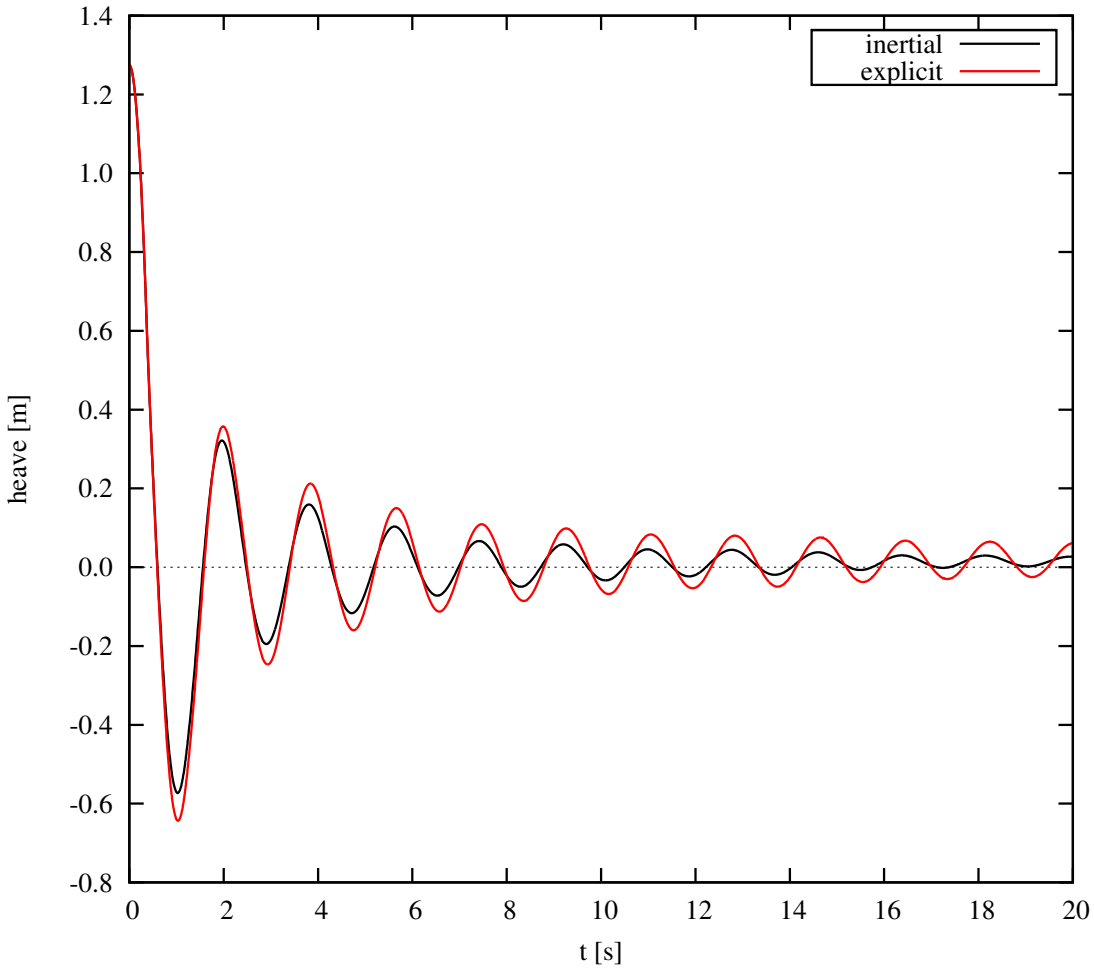

Figure 3.4: Comparison of box heave time-series using different relaxation methods.

solver, inertial under-relaxation in later results. The results presented in Chapter IV for an elastic wedge are obtained with the explicit under-relaxation method. Explict under-relaxation is also used for the initial simulations of the box barge in Chapter V. The refined box barge simulation, and the JHSS simulations from the same chapter are obtained with the inertial under-relaxation method.

3.5.2 Exchange of Data on the Mutual Interface

The fluid-structure interaction occurs along a mutual interface where the two domains of continuous variables meet. The current method implements procedures, similar to those in the papers by *Maman and Farhat* (1995) and *Farhat et al.* (1998), that do not require identical discretization of each of the fluid and structural domains on the mutual interface. The ability to have different discretization of each domain is very powerful, as the structural and fluid discretizations are usually performed by different people in different programs, and the locations where each discipline focuses are not neccessary the same.

The structural equations of motion require information about the fluid stress on the boundary. The fluid force at the finite element nodes is computed using a three-point Gauss integration rule for the beam elements (3×3 for plate elements). The fluid stress at each Gauss point is found by taking a distance-weighted average of the fluid pressure at the four fluid faces which are closest to the integration point. An illustration of this matching is shown in Figure 3.5.

The fluid domain requires information about the structural velocity and displacement. The velocity and displacement of the fluid boundary at the fluid-cell-face center along the mutual interface is found using the structural-element shape function. The formulation of the fluid boundary condition and mesh deformation strategy is described in detail in Section 3.5.3.

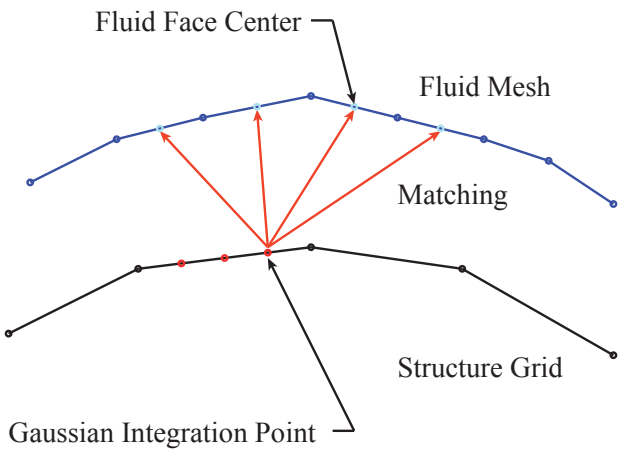

Figure 3.5: Illustration of matching between structure grid and fluid mesh.

3.5.3 Fluid-Boundary Condition on the Mutual Interface

Two forms of the fluid boundary condition are commonly used for fluid-structure interaction analysis. The no-slip condition states that the fluid velocity is equal to the structural velocity on the mutual interface:

$$\vec{u}(\vec{x}_b, t) = \vec{u}_b(\vec{x}_b, t), \tag{3.42}$$

where $\vec{u}_b$ is the body velocity and $\vec{x}_b$ is the position of the structure. The structural velocity is applied to the fluid boundary in one of two ways in this work. In the first method the mesh is deformed to exactly follow the structural mesh. This is denoted as satisfying the exact no-penetration body-boundary condition.

The second method to determine the boundary condition for the fluid domain is to apply the structural velocity on its undeformed position. This method has successfully been used for aeroelastic simulations (*Yang et al.* (2004)). The approximation is justified based on the assumption of small structural deformation, a concept that is consistent with the modal representation of the structure.

For either boundary condition, the velocity on the fluid boundary (whether de-

formed or not) is the sum of the rigid body velocity and the structural velocity. The velocity at any point on the body is therefore given by:

$$\vec{v}(\vec{x}) = \vec{v}_R + \vec{\omega}_R \times (\vec{x} - \vec{x}_{CM}) + \sum_{i=1}^{N} \Phi_i(\vec{x})\dot{\delta}_i, \tag{3.43}$$

where $\vec{x}$ is the point, $\vec{v}_R$ and $\vec{\omega}_R$ are the rigid body translational and rotational velocities, $\vec{x}_{CM}$ is the position of the center of mass, Φ_i is the i^{th} mode shape, and $\dot{\delta}_i$ is the modal velocity of the i^{th} mode.

While the exact boundary condition is more accurate in formulation, the implementation of this condition requires deformation of the CFD mesh. This is an expensive and not necessarily robust process. The approximate boundary condition does not require expensive mesh deformation strategies and retains the original mesh quality. The approximate boundary condition is shown in the results section to be accurate and provide to significant computational savings for the present analysis.

The large-amplitude motion of the body is applied by translating and rotating the fluid mesh as a solid body. This solid body transformation of the mesh allows for the cell quality to remain constant. The disadvantage to this method is that to maintain a refined region of mesh near the free-surface will require more cells, as the mesh can move significantly with respect to the free-surface.

CHAPTER IV

Hydroelastic Wedge Entry and Exit

In this chapter, three different hydrodynamic problems related to two-dimensional wedge impact and exit are studied. These results were originally published in *Piro and Maki* (2011, 2013). The two-dimensional wedge shape is a geometrically simple model of a ship section, but the flow around it contains many of the complexities associate with the full problem of a ship in a seaway. These complexities include a high speed jet root, overturning free-surface, and large flexural added mass. The two-dimensional wedge is used to first validate the FSI algorithm, and then study a new problem.

The first problem studied is the constant velocity impact of an elastic wedge. This problem is useful to study the convergence of the solution with respect to the number of structural elements, number of structural modes, and number of fluid cells. The results from the present method are validated by comparison with the theory of *Korobkin et al.* (2006).

The second problem is the entry (impact) and exit of a rigid wedge, and the third problem is the entry and exit of an elastic wedge. For this third problem, no other known results are available; hence, the rigid case is studied to ensure the fluid solution is accurately solved for with the present tool.

The problem of the entry and exit of an elastic wedge is studied for a wide range of

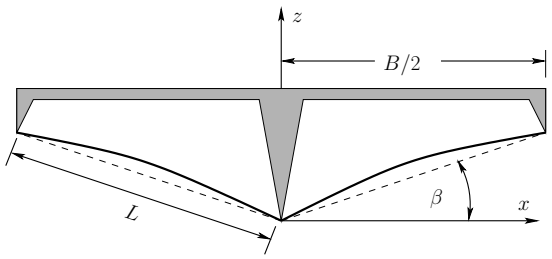

Figure 4.1: Elastic wedge model.
Elastic wedge model used in simulations

structural stiffness. This elucidates the regimes in which hydroelasticity is important, and allows for detailed evaluation of several FSI approximations that are used in the practice of ship structural design.

All of the simulations in this chapter are performed using the wedge model shown in Figure 4.1. The geometry of the wedge is defined by the distance from the keel to the chine L, the geometric half beam $B/2$, and the deadrise angle of the undeformed wedge β. The structure is considered to be a Euler-Bernoulli beam with pinned boundary conditions at the keel and the chine.

4.1 Constant Velocity Hydroelastic Wedge Impact

In this section the constant velocity impact of an elastic wedge is studied. First, analysis is focused on the discretization of the structural and fluid domains. Then, the deflection of the structure is compared with the published results of *Korobkin et al.* (2008).

The problem is a 10 deg deadrise wedge, with length $L = 0.5$ m. The impact velocity is $V = 4$ m/s, into water of density of $\rho_w = 1000$ kg/m^3. The structure is steel, characterized by the modulus of elasticity $E = 210$ GPa, and mass density $\rho_s = 7850$ kg/m^3. The beam has thickness $h = 18$ mm. In the present method, the air phase is included in the fluid-dynamic simulation. The air density is 1.5 kg/m^3. The kinematic viscosity of the fluid is 1×10^{-6} m^2/s in water, and 1.5×10^{-5} m^2/s

in air. These values correspond to a case that could be studied experimentally and closely resemble the problem studied in *Korobkin et al.* (2006).

This case is chosen because it results in sufficiently large structural deformation such that hydroelasticity is important. The importance of hydroelasticy to a particular slamming event for wedge-shaped bodies can be estimated using a so-called "hydroelasticity factor." A popular version is that which is proposed in *Faltinsen* (1999), where R_F is defined as

$$R_F = \frac{\tan\beta}{V}\sqrt{\frac{Eh^3}{12\rho_w L^3}}. \tag{4.1}$$

This quantity represents the ratio of the loading period to the dry-structural period. A value of less than two indicates that fluid-structure interaction may be important for the structural response. The given parameters lead to a value of $R_F = 1.26$, which suggests that hydroelastic effects are important.

4.1.1 Convergence of Finite-Element Discretization

The convergence of the finite element description of the structure is examined by calculating the natural frequencies for a given number of elements. This is done for a pinned-pinned beam with the dimensions that are used for the impact simulations.

The Grid Convergence Index (GCI) of the *ASME* (2008) standards is used to provide a quantitative measure of the uncertainty in the numerical result (this quantity represents a percentage of uncertainty). The beam is disretized with 10, 20, 50, 100, and 200 elements. The first 20 natural frequencies are examined to determine the convergence of the structure, the results of which are summarized in Table 4.1. The ASME procedure also calculates the observed order-of-accuracy of the numerical method; in this case it is 0.93 for mode 5 (slightly less than linear convergence).

Examination of the results shows that the number of elements that are required

N	Mode 1	Mode 5	Mode 10	Mode 15	Mode 20
50	0.0000	0.0237	0.2370	1.8246	381.96
100	0.0000	0.0004	0.0057	0.0306	0.0726
200	0.0000	0.0000	0.0006	0.0031	0.0107

Table 4.1: ASME Grid Convergence Index (in percent) with different numbers of elements (N)

to achieve a given level of uncertainty is dependent on the number of modes that are used. For example, using 50 elements yields uncertainty of less than 1% if only 10 modes are used, but for 20 modes, 100 elements are required for similar accuracy. Therefore, 100 elements are used to model the beam for the results presented in this chapter.

4.1.2 Modal Convergence

The number of mode shapes required to accurately represent the structure is determined using two methods. The first analyzes the modal force that is generated from a rigid-wedge impact, and the second examines the maximum deflection of the elastic wedge calculated with different numbers of mode shapes.

The time series of the modal force for each of the first five modes from the rigid wedge impact is shown in Figure 4.2. The energy spectra of each time series is found by performing a fast Fourier transform. This is combined with the transfer functions of the modes to obtain response spectra for the modal amplitudes. The energy contained in the different mode shapes is compared by integrating the response spectra. In Table 4.2 the energy is expressed as a percentage of the total energy in all of the mode shapes that are examined. Although this analysis is done for rigid-body impact, it is expected that the modal breakdown of the forcing will be strongly related to that of an elastic body, as is shown next.

Hydroelastic impact is then simulated with different numbers of modes. Figure 4.3a shows the time series of the deflection of the middle of the beam w_{mid}. A

Mode #	% Total Response Energy	Cumulative Energy
1	96.065	96.065
2	3.212	99.277
3	0.523	99.800
4	0.114	99.914
5	0.040	99.952
10	0.002	99.996
15	0.000	99.999
20	0.000	100.000

Table 4.2: Modal response energy - rigid impact.
Energy in modal response of a beam to rigid wedge impact

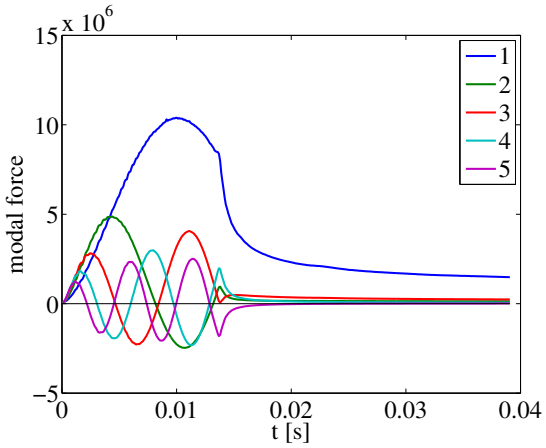

Figure 4.2: Modal force for 18mm plate.
Modal force for 18mm plate - modes 1 to 5 - rigid wedge constant velocity impact

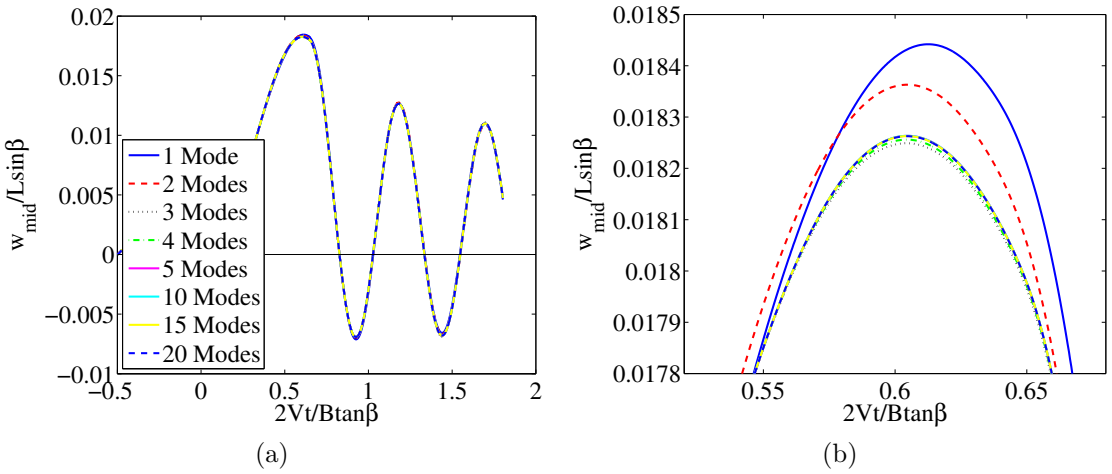

Figure 4.3: Deflection with different numbers of modes.
Deflection time series using different numbers of mode shapes: (a) for entire simulation and (b) near time of maximum deflection

close-up of the response is shown in Figure 4.3b. It is clear that five modes are very accurate to describe the deflection of the beam.

The maximum deflection, $w_{\max}$, and the time of occurrence of the maximum deflection, $t_{\max}$, are analyzed further to more clearly study the modal convergence. The results are included in Table 4.3 and plotted in Figure 4.4. It is seen that the two quantities no longer vary for the number of modes that are 5 or greater. It is noted that the time-of-occurence for 20 modes does change slightly with respect to that of 5 to 15 modes. This is explained by the fact that the variation is of the order of the time-step size. Based on the results of both the spectral energy using the rigid-wedge force, and the simulations with varying numbers of modes, five mode shapes and 100 elements are selected to describe the structure for this problem.

4.1.3 CFD Grid Convergence

A grid convergence study is performed by simulating the constant-velocity impact of the elastic wedge using three grids. The fluid domain discretization results in 50, 100, and 200 cells along the wedge. Table 4.4 summarizes the discretization of

N	$w_{\max}$ [mm]	$t_{\max}$ [ms]
1	1.60121	13.2913
2	1.59436	13.1321
3	1.58445	13.1221
4	1.58507	13.1122
5	1.58570	13.1221
10	1.58571	13.1221
15	1.58565	13.1221
20	1.58564	13.1321

Table 4.3: Modal convergence of deflection.
Convergence of maximum deflection for different numbers of mode shapes

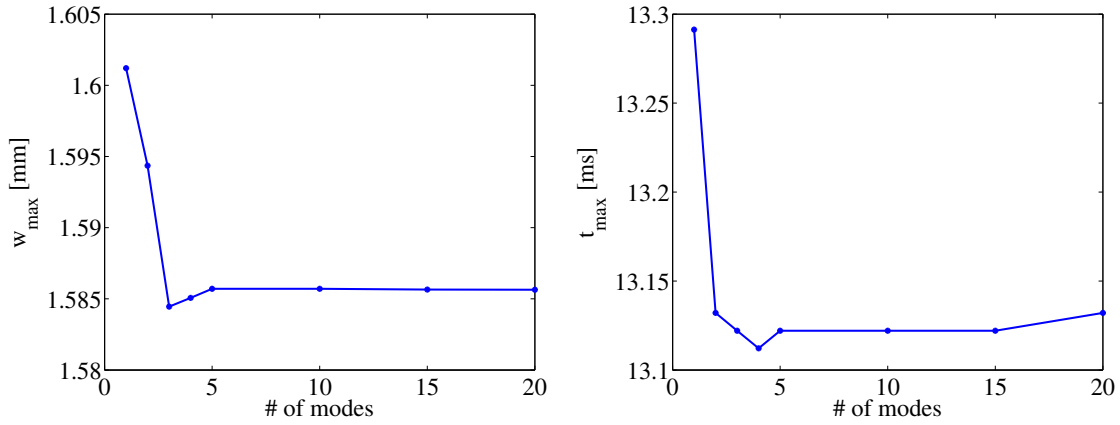

(a) (b)

Figure 4.4: Modal convergence for magnitude and time of maximum deflection.
Convergence of modal description of structure: (a) for maximum deflection and (b) for time of maximum deflection

Grid	# of cells in fluid	# of cells on body	Exact BC	Approx. BC
1	7,300	50	1.6531	1.6495
2	29,200	100	1.6322	1.5857
3	116,800	200	1.6061	1.5581

Table 4.4: Fluid grid convergence
Maximum deflection (mm) for three fluid grids

the fluid domain and the results of the grid-convergence study. The convergence of both the exact body boundary condition and the approximate boundary condition is examined. The solution variable that is used in the calculation of the GCI is the maximum deflection at the midpoint of the beam $w_{\max}$. The GCI on the fine grid is approximately 1.6% for the exact boundary condition, and 4.8% for the approximate boundary condition.

4.1.4 Comparison with Previous Numerical Simulations

Figure 4.5 shows a comparison of the deflection time series at the center of the beam for the two different boundary conditions together with the results from the theory of *Korobkin et al.* (2006). The deflection using the approximate boundary condition agrees well with that using the exact body boundary condition. The difference between the maximum deflection predicted by either boundary condition is 0.22%. The current simulations predict a lower deflection than the results from *Korobkin et al.* (2006). This is most likely due to the use of the Wagner impact theory, which is known to overpredict the force on the wedge when the deadrise angle departs appreciably from zero, up to 17% for a 10° wedge based on formulas in *Korobkin* (2004). The predicted time to maximum deflection is quite similar between the results of *Korobkin et al.* (2006) and the current simulations. Note that the current method can easily predict the response after the time of maximum force while the hydrodynamic force model used in the method presented in *Korobkin et al.* (2006) is no longer valid;

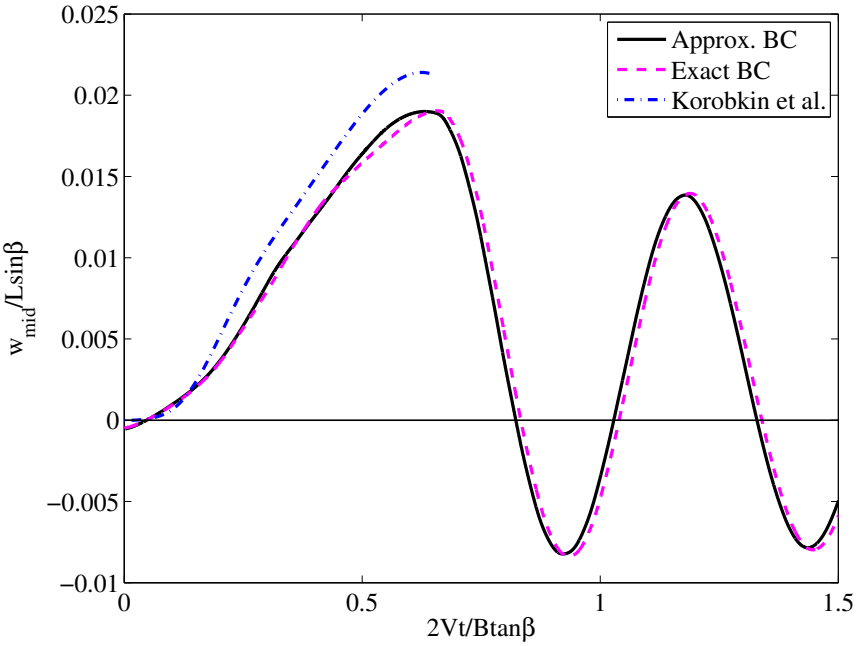

Figure 4.5: Deflection comparison for rigid wedge impact.
Comparison of deflection of center of beam for fine grid

as such their method is not plotted after this instant in time.

4.2 Entry and Exit of a Rigid Wedge

In this section, the entry and exit of a rigid wedge is studied. First the flow-field is summarized by examining the pressure field and free-surface elevation. Next, the wetted length and vertical force is compared to impact theory using the wetted-length models of von Karman and Wagner.

The entry and exit of the body is described by vertical motion with constant acceleration. The origin of the time coordinate is aligned with the instant at which the keel of the wedge touches the calm-water plane. The equation for the vertical displacement (similar to *Faltinsen* (1999)) is

$$y(t) = \frac{1}{2}V_1 t^2 + V_0 t. \tag{4.2}$$

Case	$y_{\min}/L\sin\beta$	V_0 [m/s]
1	0.5	4
2	0.5	8
3	1.0	4
4	1.0	8

Table 4.5: Entry and exit cases

Four cases are selected with two values of the velocity at time of zero V_0, and two levels of maximum immersion of the wedge into the water $y_{\min}$. The cases are summarized in Table 4.5. The values of V_0 are chosen to correspond with the analysis of the constant-velocity impact studies in the earlier sections of the paper. The values of the maximum immersion are chosen to correspond to either a "chines dry", or "chines wet" scenario. Note that in Table 4.5 the quantity $y_{\min}/L\sin\beta$ is a dimensionless maximum immersion, which is defined as A. When this quantity is equal to one, the chine reaches the calm-water plane. Due to the piling up of water, these cases are "chines wet". For $A = 0.5$, the jet root does not arrive to the chine, and the cases are "chines dry".

The vertical force on the full wedge is non-dimensionalized using impact velocity V_0, the beam B, and water density ρ_w, as shown in Equation 4.3:

$$F_y^* = \frac{2F_y}{\rho_w V_0^2 B}. \tag{4.3}$$

Time is made dimensionless by using the scale of the time to maximum immersion $t_0 = -V_0/V_1$.

The wetted length c is computed in the present simulations as the distance from the keel to the point on the body of maximum pressure. While the jet root is attached to the body, this quantity is easily determined. After the jet root leaves the body, it is assumed that the wetted length is the length of the beam L. The theoretical

wetted length is expressed as Equation 4.4 (see *Faltinsen* (2005) p. 309):

$$Mc(t) = \int_0^t V(\tau)d\tau = V_0 t + \frac{1}{2}V_1 t^2. \tag{4.4}$$

The constant M is $2\pi^{-1}\tan\beta$ for the Wagner model and $\tan\beta$ for the von Karman model. Both the Wagner and von Karman models use linear potential flow with a linearized free-surface boundary condtion, but Wagner theory includes the free-surface pile-up and jet along the wedge.

The flow-field resulting from the entry and exit of the wedge-shaped body is shown in Figure 4.6. In the left column, the chines-dry Case 2 is shown. The first image shows a flow-field that is commonly seen during impact, with a thin jet and large pressure very close to the jet root, and a pile-up of water. At the time of maximum immersion ($t/t_0 = 1$), the pressure is negative along the body, and the free-surface elevation is still very similar to that seen in impact. As the body begins the exit from the water, the pressure remains negative, and the free-surface shows a depression between the far-field and the body. As time continues, the pressure increases and the depression grows. Simultaneously, the contact point of the free-surface on the body moves upward with the body. The behavior in Case 4 is similar to Case 2 in that during the exit stage a significant depression is seen in the free surface between the body and the jet of water that escaped from the body during impact.

Figures 4.7a and 4.7b show the comparison of the wetted length from the present simulations and the two impact theories. The wetted length compares exceptionally well between Wagner theory and the numerical simulations during the entry phase. The wetted length from von Karman theory is lower than that of the simulations because it does not account for the pile up of the water.

The plot of the force time series for Case 1 is shown in Figure 4.8a. Also in this figure, the force predicted from impact theory with the Wagner and von Karman

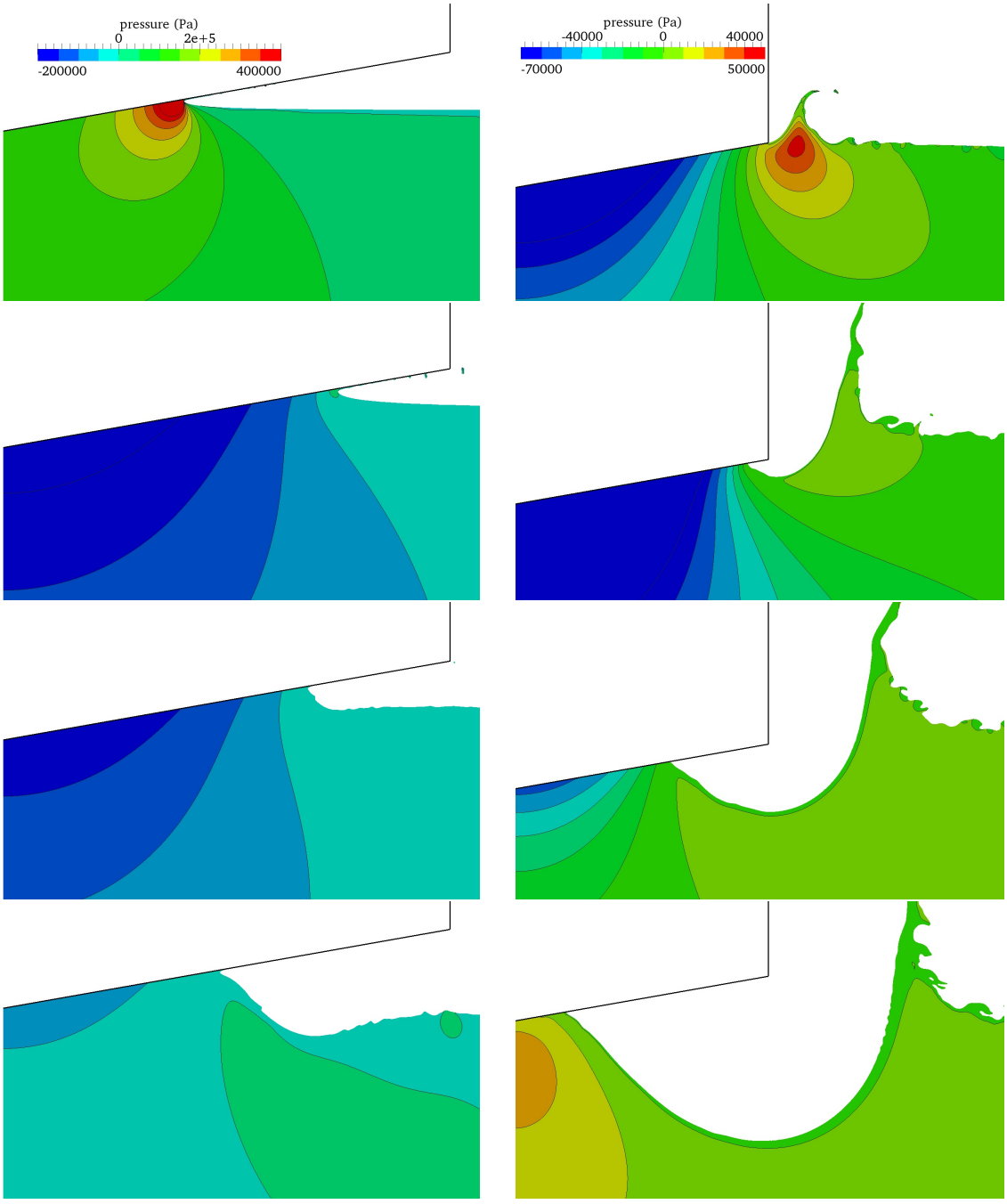

Figure 4.6: Pressure contours for Cases 2 and 4.
Pressure contour for Case 2 (left column) and Case 4 (right column). Top row $t/t_0 = 0.4$, second row $t/t_0 = 1.0$, third row $t/t_0 = 1.6$, bottom row $t/t_0 = 2.1$.

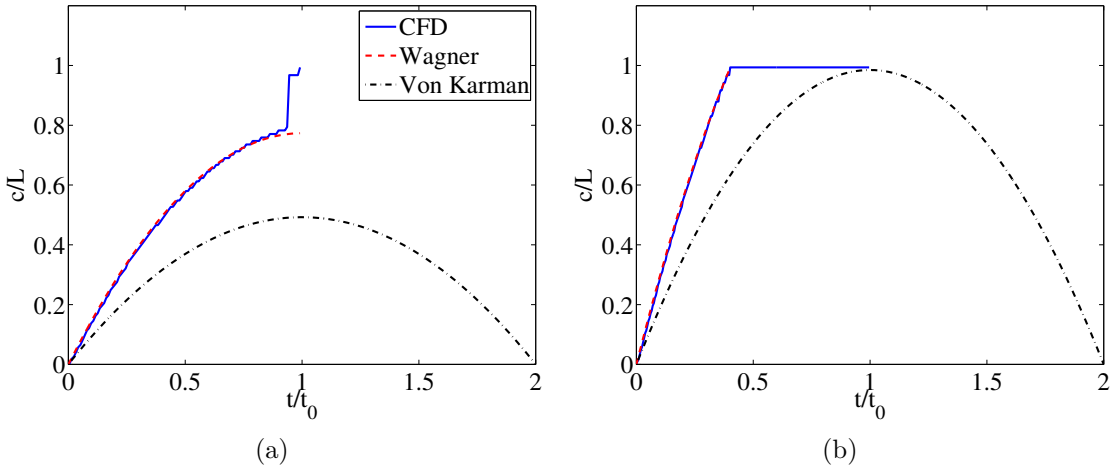

Figure 4.7: Wetted length comparision: entry and exit.
Wetted length comparison: (a) for Case 1 and (b) for Case 3

wetted length models is shown. The vertical force from the impact theory is given by (see *Faltinsen* (2005) p. 307):

$$F_y = \rho\pi V c\frac{dc}{dt} + \rho\frac{\pi}{2}c^2\frac{dV}{dt}. \tag{4.5}$$

The force has two components: a slamming term which is proportional to the velocity and the added-mass term that is proportional to the acceleration. The Wagner theory is only valid when the wetted length is increasing; thus, the time series of the Wagner force is shown when the following two conditions are met: $t < t_0$ and $c < B/2$.

Figure 4.8a shows that the Wagner theory over-predicts the slamming force by about 25% for the chines-dry case. This is similar to the constant-velocity wedge-impact scenario.

Figure 4.8b shows the vertical force for Case 3 ($A = 1$ with chines wet). Similar to Case 1, the Wagner theory slightly over-predicts the results from the present simulation during the chines-dry stage of the entry. The von Karman force is substantially lower than the prediction from the present simulation during entry, although during exit, the force magnitude is much more similar. Recall that *Dessi and Mariani* (2006)

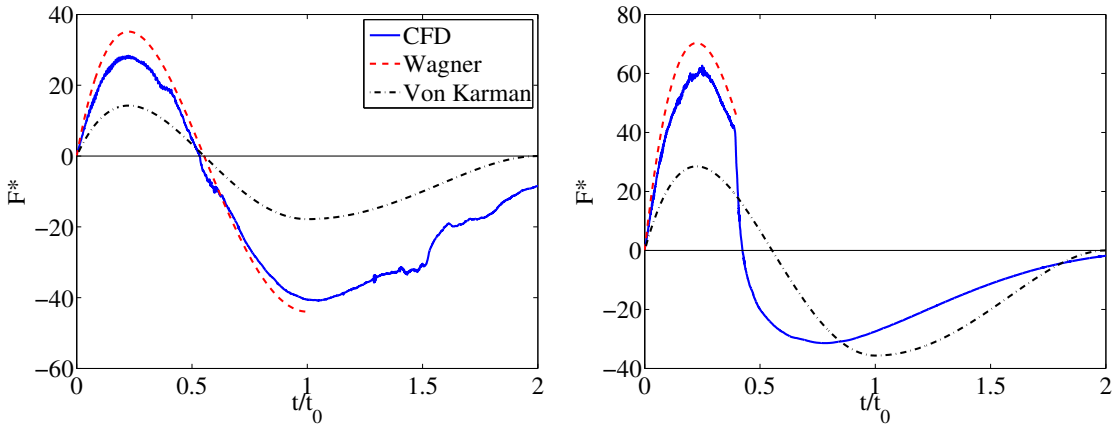

Figure 4.8: Force comparision: entry and exit.
Non-dimensional force time series: (a) for Case 1 and (b) for Case 3

suggest the use of von Karman theory to predict the force during the exit phase, which seems reasonable according to the presented results.

4.3 Entry and Exit of a Hydroelastic Wedge

In this section the entry and exit of a hydroelastic wedge is studied. The primary focus of this exercise is on the deflection and stress that develops in the structure during the entry and exit event. This is useful for the purposes of design and identification of the maximum stress developed in a ship structure during operation in a seaway. To describe and analyze the reaction of the structure and its influence on the hydrodynamic solution, the modal force is also examined.

The geometry is identical to that described in Section 4.1. The vertical motion of the body is that of Cases 2 and 4 from Section 4.2. To vary the influence of hydroelastic effects, 13 different values of the plate thickness are studied for each motion case. The plate thickness varies from 6 to 50 mm. The plate length is 0.5 m and thus the thicknesses range from about 1% to 10% of the length. The stiffness of the thickest plate is representative of the structure near a transverse stiffener.

According to the discretization study on the constant-velocity-impact problem, the structure is composed of 100 elements. Five modes are retained based on the observation that this number describes 99.95% of the response energy. The fine fluid grid is used with the approximate boundary condition.

The results that follow show three different methods to predict the elastic response of the beam. The tightly-coupled (TC) procedure developed in this paper is compared to two approximate methods that are commonly used for industrial applications, called rigid-quasi-static (RQS) and rigid-dynamic (RDyn).

The hydroelastic approximations used to evaluate the hydroelastic solver are illustrated through the equation-of-motion of a single degree of freedom, δ. This could be an equation for one of the modes. The exact expression that governs a mode is given by Equation 4.6, with relation to a representive mass m, representative stiffness k, and forcing f. The forcing is a function of the motion of the structure, as well as time. Our tightly-coupled method solves this equation.

$$m\ddot{\delta} + k\delta = f(\ddot{\delta}, \dot{\delta}, \delta, t) \tag{4.6}$$

The first approximation is called rigid/quasi-static (RQS), in which the forcing is not a function of the motion of the structure (rigid structure for fluid simulations); it is only a function of time. Also, in the RQS approximation, the flexural mass is neglected. This results in the equation of motion given by Equation 4.7, where δ_{RQS} is the solution of this approximate equation and $f_R(t)$ is the fluid force that does not have the influence of structural deflection. It is common practice for design purposes to perform a RQS analysis of a ship structure, and apply a "dynamic amplification factor" to account for error in neglecting flexural mass and the influence of the structural deformation on the external forcing. This factor often comes from the dynamic overshoot of a single degree of freedom system subject to a square wave loading. It

is commonly accepted that the maximum value of the factor is two, as in *Heller and Jasper* (1960).

$$k\delta_{\mathrm{RQS}} = f_R(t) \tag{4.7}$$

The next approximation is called rigid-dynamic (R-Dyn), in which the forcing is not a function of the structural motion, but the dynamics of the structure are included. The resulting equation of motion is given by Equation 4.8, where δ_{RD} is the solution of this equation. This approximation is the same as the the one-way coupled simuations with dry frequencies in *Maki et al.* (2011). It is useable as long as wetted mode shapes and frequencies that are appropriate for the loading are selected.

$$m\ddot{\delta}_{\mathrm{RD}} + k\delta_{\mathrm{RD}} = f_R(t) \tag{4.8}$$

Figures 4.9 to 4.12 show time series of deflection of the middle of the plate for thicknesses of 12, 18, 32, and 50 mm. The plots show the results of the TC, along with the RQS and RDyn solutions. Note that the horizontal axis starts for time less than zero, and that the structure has negative deflection before it impacts the water at time equal to zero. This is due to the fact that the body is in constant upward acceleration, which produces a body force and deflection.

Comparison of the TC and RDyn solutions clearly shows the effect of added mass on frequency of oscillation. That is, the frequency of oscillation predicted by the RDyn approximation is too high, which is because the flexural added mass is neglected. The deflection that is predicted with the RQS approximation shows no oscillation because the structure only reacts statically to the fluid force generated by the motion of a rigid structure.

One of the principal complications of hydroelastic entry and exit when compared to many fluid-structure interaction problems is the time-dependent wetted surface of the structure. The tightly-coupled method accurately accounts for this phenomenon,

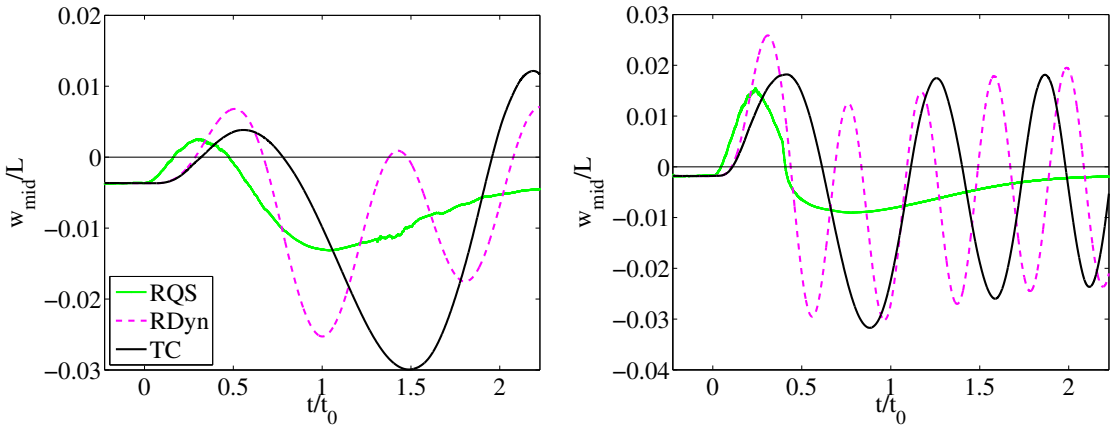

Figure 4.9: Beam deflection for 12 mm beam
Deflection at center of beam with $h = 12$ mm: (a) for motion Case 2 and (b) for Case 4

which can be observed in Figure 4.11b. In this figure, it can be seen that the RDyn solution is oscillating as a dry structure. At time of $t/t_0 \approx 1$, the structure is maximally wetted, and the frequency of oscillation is lowest in the TC solution. As time approaches $t/t_0 \to 2$, the structure exits the water (this is not to say that it is completely dry; see Figure 4.6), and the frequency of oscillation approaches that of the dry beam.

In general, it is seen that the maximum deflection is always underpredicted by the RQS approximation. This quality leads itself to be well suited for a treatment that uses a factor of safety to account for modeling errors. On the other hand, the RDyn approximation may over or under predict the maximum deflection.

The next quantity examined is the modal force time series, shown in Figure 4.13. Motion Case 2 is on the left and Case 4 on the right. The modal force shown here is calculated with the rigid-body pressure and the modal matrix corresponding to the plate thickness of 50 mm. This is the modal force time history used to determine the response in the RQS and RDyn approximations. It is seen that the magnitude of the forcing of mode 1 in Case 4 is about twice the value in Case 2 for $t/t_0 < 0.5$.

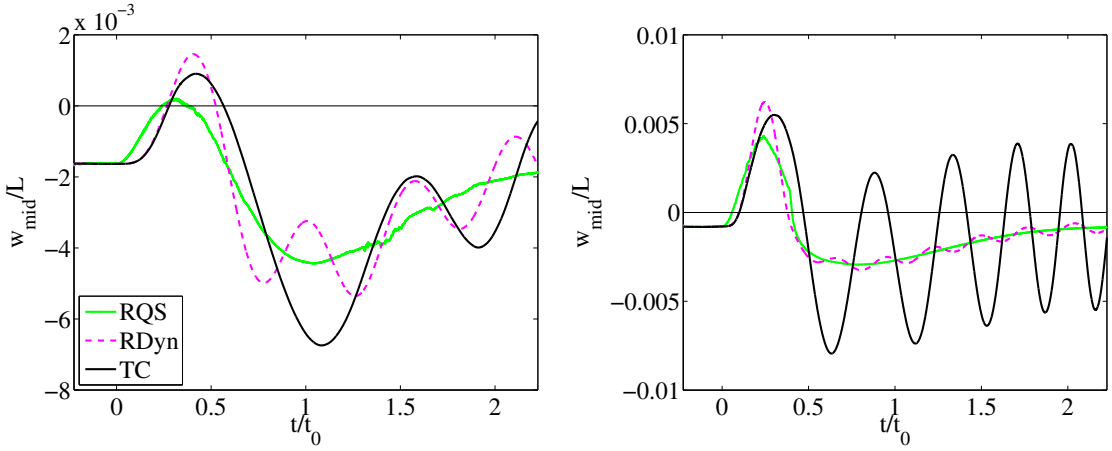

(a) (b)

Figure 4.10: Beam deflection for 18 mm beam
Deflection at center of beam with $h = 18$ mm: (a) for motion Case 2 and (b) for Case 4

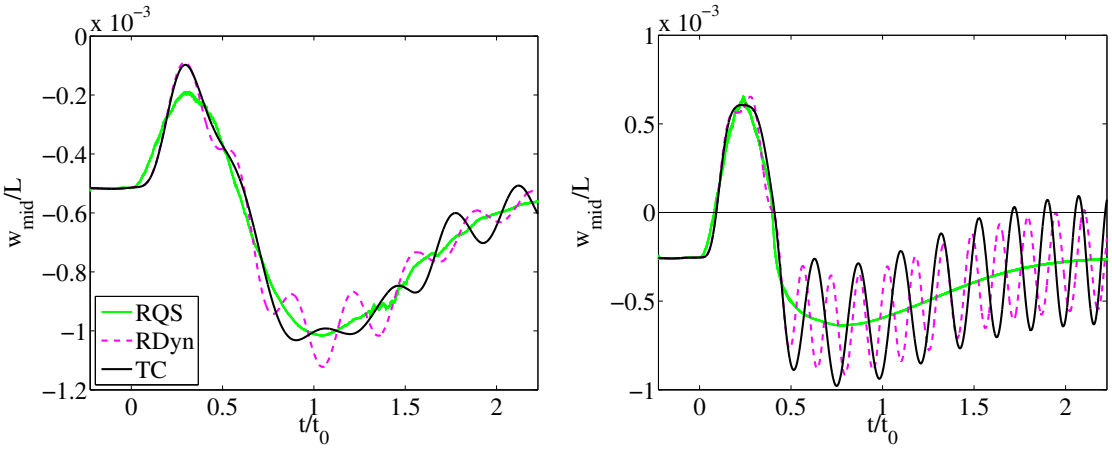

(a) (b)

Figure 4.11: Beam deflection for 32 mm beam
Deflection at center of beam with $h = 32$ mm: (a) for motion Case 2 and (b) for Case 4

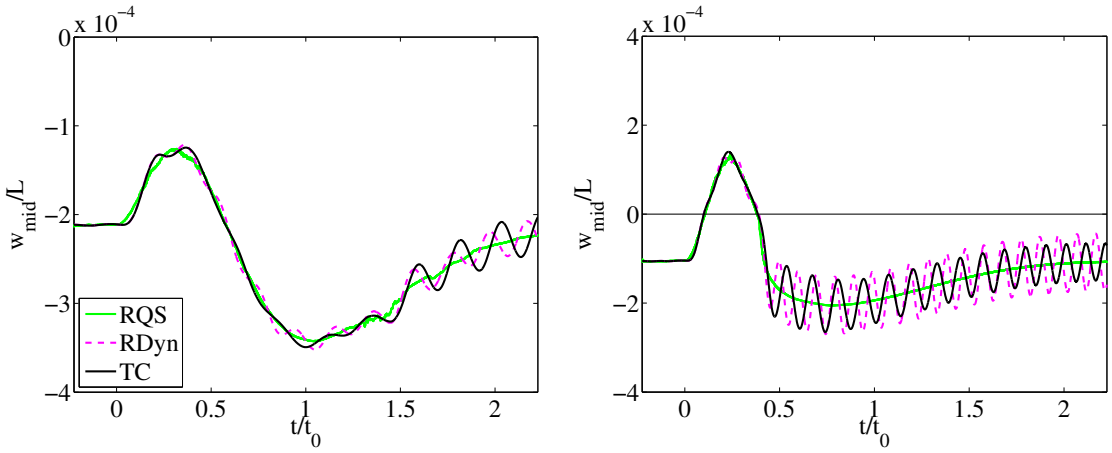

Figure 4.12: Beam deflection for 50 mm beam
Deflection at center of beam with $h = 50$ mm: (a) for motion Case 2 and (b) for Case 4

Also, the rise and fall of the positive force occurs over a shorter time period for the chines-wet Case 4.

To more clearly understand the error associated with each approximation, the maximum absolute value of stress predicted by each of the methods is examined. The comparison of stress is made using the ratio of the tightly-coupled result divided by the approximate result. This ratio can be thought of as the amplification factor that would scale the approximate result to that predicted by the more accurate method.

A plot of the stress ratio for the RQS is shown in Figure 4.14. Each value of plate thickness has a different result, which is plotted in one of two ways. In Figure 4.14a the hydroelasticity factor is computed using the velocity scale of $V_0/2$. In Figure 4.14b each value of plate thickness corresponds to a different value of t_0/T_n, where T_n is the first natural period of the dry structure.

The maximum stress from the tightly-coupled simulations is always greater than that from the RQS calculations (the stress ratio in Figure 4.14a is always greater than one). The purpose of the hydroelasticity factor is to identify when hydroelastic effects are important for the structural response. Recall that for constant-velocity impact,

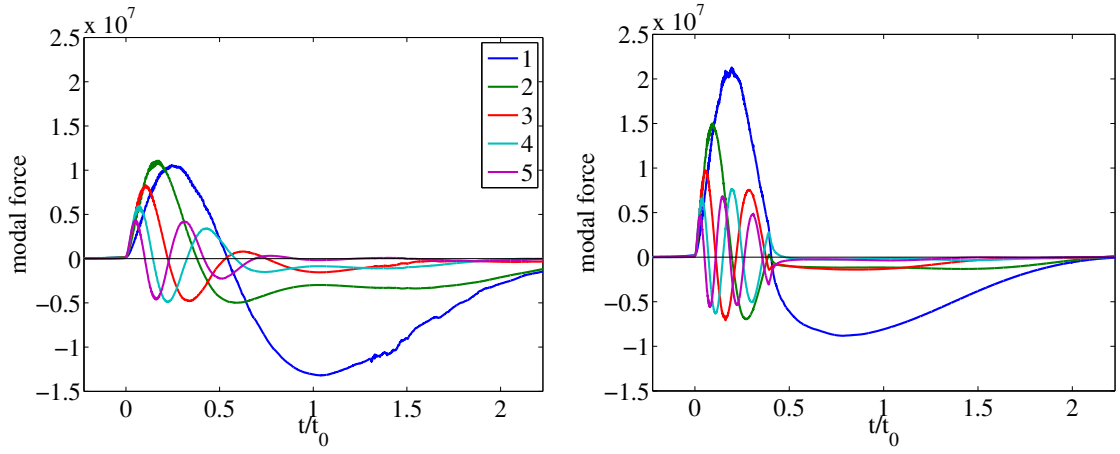

Figure 4.13: Modal force for 50 mm beam
Modal force time series for $h = 50$ mm: (a) for motion Case 2 and (b) for Case 4

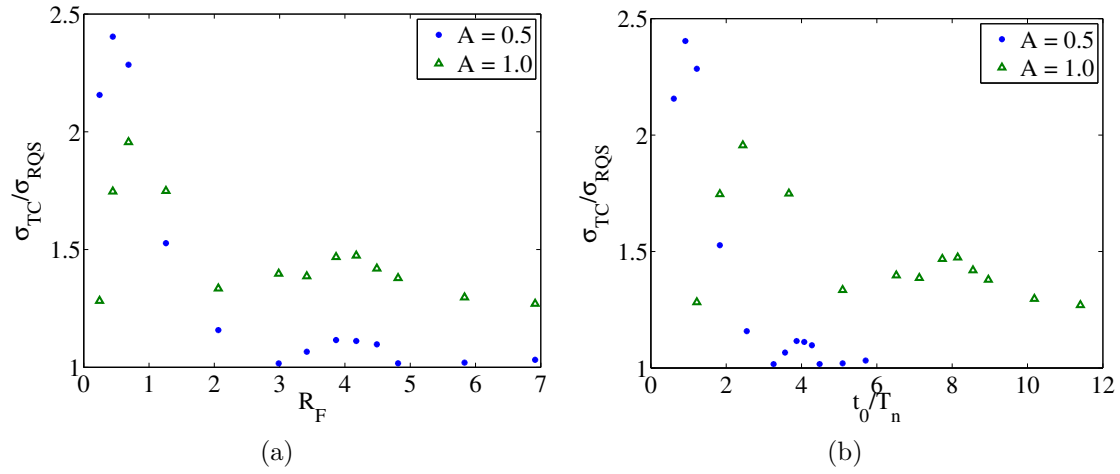

Figure 4.14: Maximum stress ratio: RQS
Comparison of maximum stress ratio for RQS approximation: (a) versus R_F and (b) versus t_0/T_n

hydroelastic effects are important when the factor is less than 2. Note that the factor is clearly defined for the constant velocity problem. In the case of linearly-varying velocity, one half of the velocity at the instant of impact (which is the average velocity during the immersion phase) is used. The values of plate thickness that produce a $R_F < 2$ show large influence of hydroelastic effects in the large stress ratio for both cases ($A = 0.5, 1.0$). For $A = 1.0$ the maximum ratio is near two, while for the "chines dry" case of $A = 0.5$, the maximum ratio is near 2.5.

For values of $R_F > 2$, the stress ratio becomes smaller. When $A = 0.5$, the ratio approaches 1, while for the $A = 1.0$, it decreases more slowly and does not appear to approach 1 over the range of plate thickness studied herein. The reason why the stress ratio for $A = 1.0$ and large R_F is appreciably greater than 1 can be seen in the time-series of displacement in Figure 4.12b. Here, consider that the jet root escapes from the chine at $t/t_0 \approx 0.4$; this time is considered to be the end of the "impact stage". During this stage, the deflections predicted by each approximation and the TC method are all quite similar, and if the stress ratio were to be computed using this segment of the response, it would be close to 1. Figures 4.14 and 4.15 show the stress ratio calculated using the maximum of the absolute value of stress over the entire time series. For $h = 50$ mm and $A = 1.0$, the ringing after the impact stage produces the largest absolute value of stress in the TC response. Thus, the value of stress ratio that is greater than 1 is a result of the stress in the ringing after the impact stage.

Now, it remains to understand why the stress ratio is close to 1 for this thickness of plate ($h = 50$ mm) for the chines-dry but not in the case of the chines-wet body trajectory ($A = 1.0$). First, examination of Figure 4.13 shows that the modal force for mode 1 and Case 4 is larger during the impact stage and returns to zero more quickly during the exit stage, when compared to the behavior for Case 2. Thus the excitation of the first mode occurs more rapidly, and the ringing is fully developed

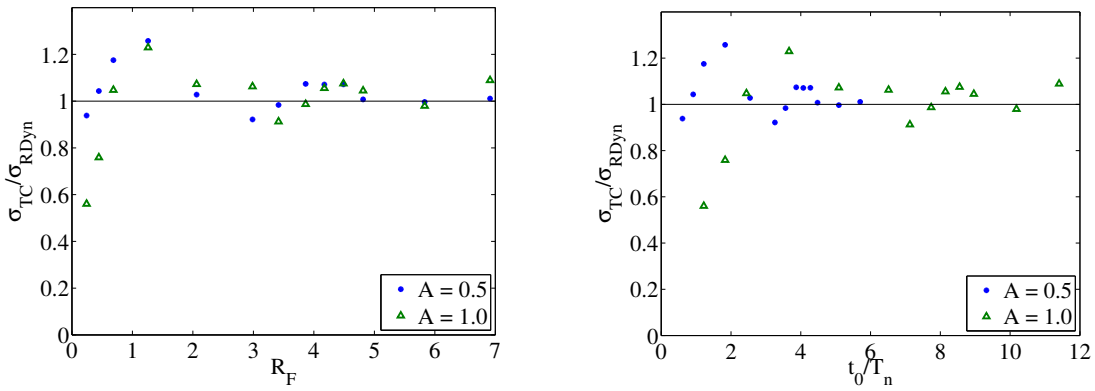

Figure 4.15: Maximum stress ratio: RDyn
Comparison of maximum stress ratio for RDyn approximation: (a) versus R_F and (b) versus t_0/T_n

over a shorter time span after initial contact with the water. This is confirmed in the examination of the time series shown in Figure 4.12. Here, it is seen that the ringing in the TC response for Case 2 is still developing at the end of the time series that is shown, whereas for the Case 4, the amplitude of the ringing is already developed by $t/t_0 \approx 1$.

The ratio of stress between the RDyn and TC approaches is examined next. Figure 4.15 shows the ratio plotted versus R_F on the left and t_0/T_n on the right. Here, it is seen that the over or under prediction by the approximate method is smaller than the over-prediction for the RQS approximation. Also, the over prediction by the RDyn approximation occurs for small R_F or t_0/T_n, or for cases in which the loading period is small with respect to the structural time scale. The under prediction occurs when the loading is more closely aligned with the structural time scale.

In Figure 4.15b, the influence of the chines wet or chines dry motion is visible in the range $t_0/T_n < 2$. For cases in which the chine is dry, the loading period is more closely described by the time to maximum immersion than in the case when the chine wets. This can be confirmed by inspection of Figures 4.8a and 4.8b. Also, the dry period T_n is closer to the wetted period when the chine is dry, because the body is

only partially immersed. When the chine wets, the wetted period is larger than for the dry case.

A final observation can be made by comparing Figures 4.14 and 4.15. The differences in the stress ratio between these two figures are due to the omission of the structural inertia term in the RQS-equation-of-motion. It can be seen that the inclusion of this term acts to bring the stress ratio closer to 1, particularly near $R_F \approx 1$.

4.4 Summary

In this chapter a two-dimensional wedge-shaped section has been used to evaluate the FSI solver. Convergence has been shown for the structural grid, fluid grid, and number of modeshapes required for the slamming problem. This convergence information is important to assure the accurate resolution of the slamming portion of global whipping response. The present method is then validated against analytical results for the constant-velocity wedge impact problem. Finally, the new problem of constant-acceleration elastic wedge entry and exit is studied, with emphasis on understanding the importance of the fluid-structure coupling.

CHAPTER V

An Elastic Ship in Waves

This chapter provides validation of the the current fluid-structure interaction solver for problems of elastic ships in waves. Validation of wave generation and propogation is first performed as waves are the main input for the system. Next, the rigid body motion solver is evaluated using the test problem of a Wigley hull in regular, head seas and is compared with experiments. Two different ship models are used to evaluate the current method for elastic ships. The first model is a segmented box barge operating in regular, oblique seas with zero-forward speed. The second model is the Joint High Speed Sealift (JHSS) model tested at NSWCCD operating with forward speed in regular, head seas. The JHSS model is then used to analyze the effectiveness of the same hydroelelastic approximations used in the previous chapter.

5.1 Wave Generation and Propogation

The wave generation library `waves2Foam` described in *Jacobsen et al.* (2012) is used in the current work. The library is evaluated here for both generation (at the inlet) and dissipation (at the outlet) of two-dimensional waves. Then a study is performed on the effect of discretization on wave propagation.

5.1.1 Two-dimensional Wave Generation and Damping

The `waves2Foam` library uses boundary conditions, as well as regions of the domain called relaxation zones, to generate and damp waves. The relaxation zones work by applying a weighted average of the calculated and target values of a flow quantity:

$$\phi = (1 - \sigma(\vec{x}))\phi_{\text{calc}} + \sigma(\vec{x})\phi_{\text{target}}, \tag{5.1}$$

where ϕ is the flow quantity (either $\vec{u}$ or α) and $\sigma(\vec{x})$ is a weighting factor that spatially varies within the relaxation zone. In the original implimentation, σ ranges from 0 to 1, with 0 at the edge of the relaxation zone interior to the domain, and the maximum value of 1 at the external boundary of the zone. The maximum value of σ has been made adjustable in this work. The variation of sigma in the relaxation zone is given by:

$$\sigma(\vec{x}) = \sigma_{\text{max}} \frac{\exp(\chi^{3.5}) - 1}{\exp(1) - 1}, \tag{5.2}$$

$$\chi = \frac{(\vec{x} - \vec{x}_{\text{int}}) \cdot \vec{d}}{(\vec{x}_{\text{ext}} - \vec{x}_{\text{int}}) \cdot \vec{d}}, \tag{5.3}$$

where σ_{max} is the adjustable scaling added in this work, $\vec{x}_{\text{int}}$ and $\vec{x}_{\text{ext}}$ are the interior and exterior bounds of the relaxation zone, and $\vec{d}$ is a unit vector aligned with the wave direction that points from the interior to exterior of the fluid domain. For inlet (generation) relaxation zones $\vec{d}$ points upstream and for outlet (dissapation) zones $\vec{d}$ points downstream.

The target quantities ϕ_{target} are determined using a selected wave theory. The `waves2Foam` library has implimented several wave theories for regular and irregular waves. For regular waves, the options include linear waves, Stokes waves (2^{nd} and 5^{th} order), cnoidal waves, and stream function waves. Unless noted otherwise, linear waves are used in the generation zone in this work. A steady current option is also available, which can be used in the dissipation zones. For a ship with forward speed in

a seaway, the library allows for superposition of waves and current. To obtain a more accurate wave, a combined linear wave and current wave theory has been created, with the free-surface elevation and velocity given by:

$$\eta(\vec{x},t) = \frac{H}{2}\cos(\omega t - (\vec{k}\cdot\vec{x}) + (\vec{k}\cdot\vec{u}_c)t + \phi), \tag{5.4}$$

$$\vec{u}(\vec{x},t) = \frac{H}{2}\omega\left(\frac{\cosh(|\vec{k}|(z+h))}{\sinh(|\vec{k}|h)}\cos\left(\omega t - (\vec{k}\cdot\vec{x}) + (\vec{k}\cdot\vec{u}_c)t + \phi\right)\right)\frac{\vec{k}}{|\vec{k}|} - \frac{H}{2}\omega\left(\frac{\sinh(|\vec{k}|(z+h))}{\sinh(|\vec{k}|h)}\sin\left(\omega t - (\vec{k}\cdot\vec{x}) + (\vec{k}\cdot\vec{u}_c)t + \phi\right)\right)\hat{z} + \vec{u}_c, \tag{5.5}$$

where H is the wave height, $\vec{k}$ is the directional wave number, ω is the wave circular frequency, z is the vertical coordinate, ϕ is a phase angle, and $\vec{u}_c$ is the current velocity.

5.1.2 Wave Generation and Damping Evaluation

The important parameters of the relaxation zones in `waves2Foam` are their length in the wave direction and $\sigma_{\max}$. Here the effect of the length of the upstream (generation) and downstream (damping) relaxation zones on accuracy is studied, along with the maximum σ value for the upstream zone. The parameters are studied in a two-dimenional wave tank, shown in Figure 5.1. The accuracy of wave generation is assessed as the mean squared error between the measured and the analytical (second-order Stokes Theory) free surface at a point downstream of the upstream relaxation zone. The accuaracy of the wave damping is assessed by the mean square error of the free surface at a point a tenth of a wavelength upstream of the domain outlet boundary.

Table 5.1 shows the results for wave length $\lambda = 3$ m, wave height $H = 0.1$ m, and domain length 18 m, with the mean squared error non-dimensionalized by wave height squared. Figure 5.3 shows the same information in graphical form. L_u is

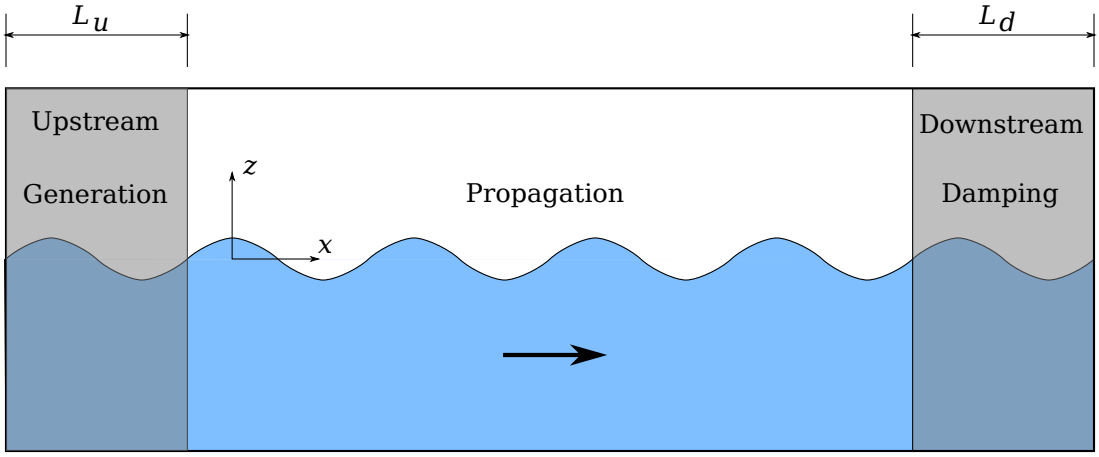

Figure 5.1: Illustration of two-dimensional wave tank used for wave generation and damping assessment. The upstream and downstream relaxation zones are highlighted in gray.

the length of the upstream relaxation zone, and L_d is the length of the downstream relaxation zone. As expected, the mean squared error decreases for increasing length of relaxation zone and increasing $\sigma_{\max}$. In these tests, when examining one parameter, the other two are held at their maximum value.

The scaling σ acts as a type of relaxation factor, and thus when the iterative mesh motion solver is used, $\sigma_{\max}$ should be less than one. Through experimentation, a limit of $\sigma_{\max} n < 1$ has been determined to provide accurate and stable solutions, where n is the number of iterations.

5.1.3 Two-dimensional Wave Propagation

The effect of the discretization on the propogation of two dimensional waves is studied. A damping coefficient ζ is calculated for the waves such that they decay with a $e^{-\zeta\omega t}$ envelope, where ω is the wave frequency. The waves are examined in a simplified domain one wavelength wide, using cyclic boundary conditions to propogate the wave. The domain is down in Figure 5.4. The results for a wave with

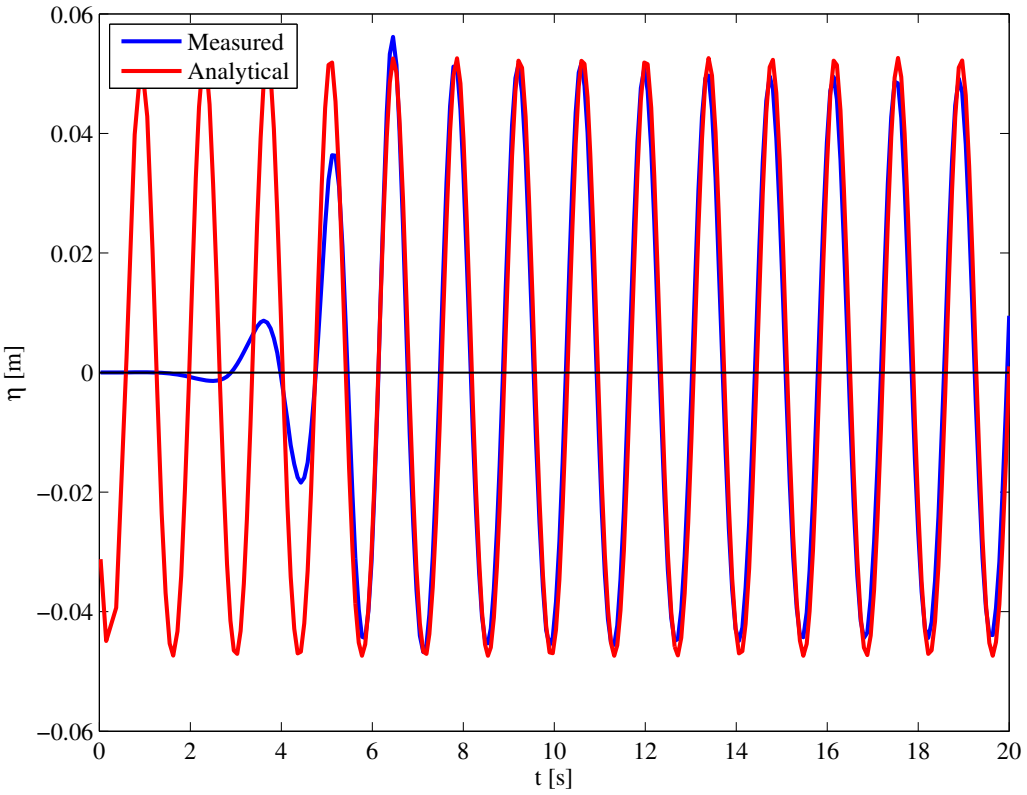

Figure 5.2: Example time series of wave generation assesment. For this figure, $L_u/\lambda = L_d/\lambda = 2.0$ and $\sigma_{max} = 1.0$.

L_u/λ	M.S.E./H^2
0.5	1.401e-02
1.0	9.823e-03
1.5	6.577e-03
2.0	3.689e-03
L_d/λ	M.S.E./H^2
0.5	6.970e-07
1.0	5.861e-10
1.5	3.153e-11
2.0	4.050e-12
$\sigma_{\max}$	M.S.E./H^2
0.1	1.540e-02
0.5	6.647e-03
1.0	3.689e-03

Table 5.1: Assessment of accuracy of wave generation and damping.

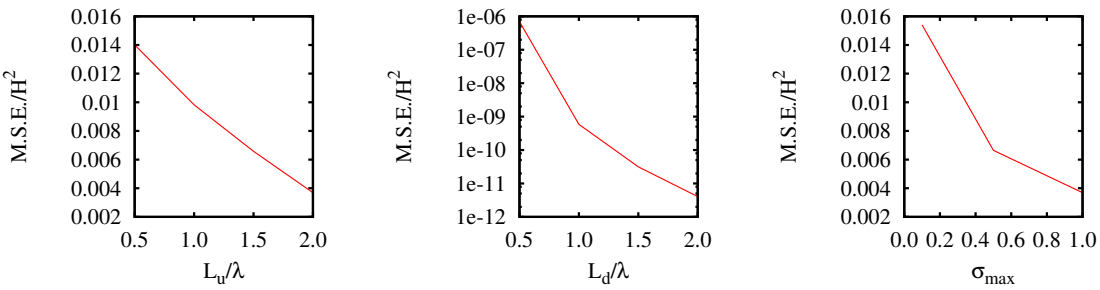

Figure 5.3: Accuracy of wave generation and damping

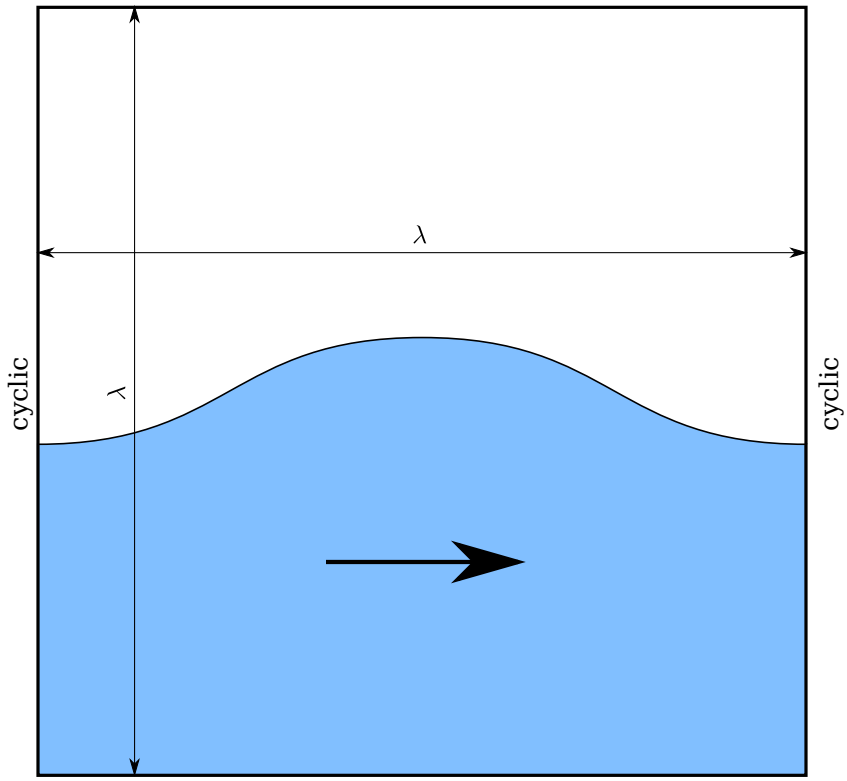

Figure 5.4: Illustration of two-dimensional single wave domain.

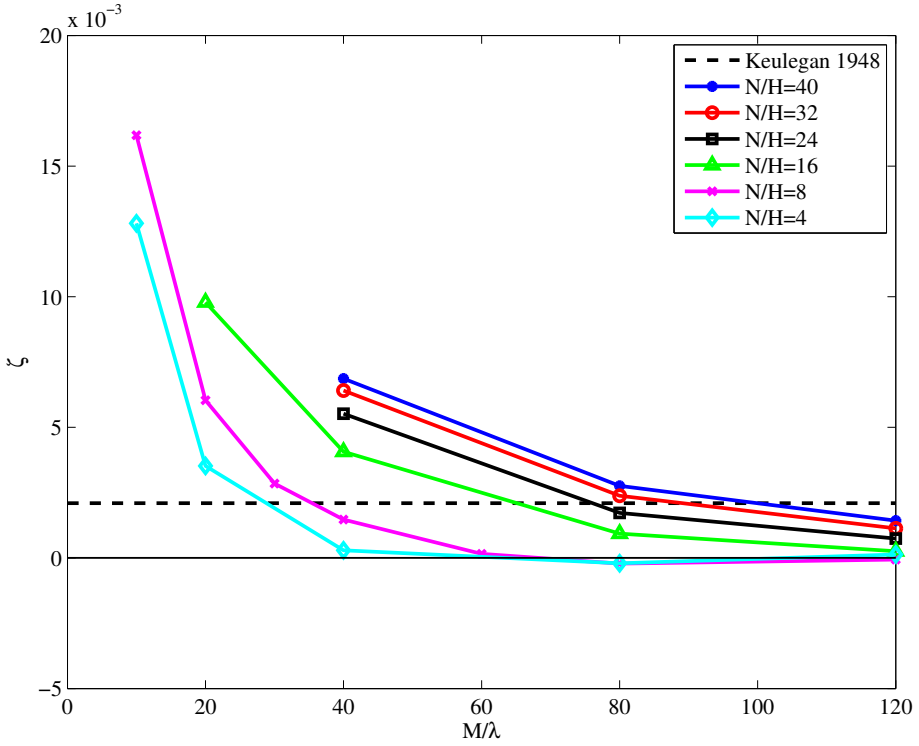

Figure 5.5: Wave damping as a function of number of points per wavelength (M/λ) and points per wave height (N/H).

$\lambda = 1.0$ m and H=0.04 m is shown in Figure 5.5. The damping coefficient is shown for different numbers of points per wavelength (M/λ) and points per wave height (N/H). Increasing the number of points per wavelength clearly reduces the damping ratio, while increasing the number of points per wave height increases the damping ratio. However, for a given number of points per wavelength, the damping ratio appears to be converging for greater numbers of points per wave height. With enough points per wave length, the damping ratio is always less than the analytical value from *Keulegan* (1948). From this study, it is determined that to propogate waves with minimal numerical dissipation, the limit on number of points per wavelength should be M/$\lambda \geq 40$.

5.2 Wigley Hull Seakeeping

The rigid body motion solver is characterized by studying a Wigley hull in regular, head seas. A Wigley hull is mathematically defined below the waterline ($z = 0$) by Equation 5.6, with the y coordinate a function of the x and z coordinates.

$$y = \pm\frac{B}{2}\left(1 - \left(\frac{2x}{L}\right)^2\right)\left(1 - \left(\frac{z}{T}\right)^2\right). \tag{5.6}$$

The calculated motions are compared to the experimental results of *Journée* (1992). Hull number III from the paper is used, with length $L = 3$ m, beam $B = 0.3$ m, and draft $T = 0.1875$ m. The depth is made to be 0.3 m, and the hull is wall sided above the waterline with a flat deck. The conditions shown here are for Froude number $Fn = 0.3$, wavelength $\lambda = 3$ m, and wave height $H = 0.04$ m. The slender shape of the Wigley hull sections results in values of added mass for heave and pitch that are smaller than the physical mass and under-relaxation is not necessary. Therefore, this hull provides a favorable test case for assessing the accuracy gained by iterating on the fluid-structure system. This case is also used to examine the neccessity of using second order time integration.

The amplitude and phase of the heave and pitch response are used to assess the method's accuracy. The heave motion amplitude is reported nondimensionally as $z'_a = z_a/\zeta_a$, where z_a is the heave amplitude and ζ_a is the wave amplitude, and the pitch aplitude θ_a is reported nondimensionally as $\theta'_a = \theta_a L/2\pi\zeta_a$. The phases for heave and pitch, α_z and α_θ respectively, are reported relative to the wave elevation. These amplitudes and phases are calculated by fitting a sinusoidal curve of the form $x = A\cos(\omega_e t + \phi)$ to the motion time series. The phase angles reported in *Journée* (1992) are adjusted to fall within $-180°$ to $180°$. The pitch phase angle is also adjusted by an additional $180°$ because the coordinate system described in the paper is left-handed.

The results for a relatively coarse 446,000 cell grid (40 cells along the length of the body) are summarized in Table 5.2, with the simulations denoted by the number of fluid-structure iterations (1 to 5 itr.) and order of time accuracy (1^{st} or 2^{nd}). Note that the simulations labeled "1 itr*" have one fluid structure iteration, but solve the pressure equation three times. Figure 5.6 shows example images from the simulations. Figure 5.7 shows the nondimensionalized motion time series for the three iteration, second order case, with the wave build-up and development of a steady state visible. Table 5.2 also shows the execution time for the simulations, which were preformed on 12 processors. The trend in simulation time is that the more FSI interations performed, the longer the simulation will take, as is expected.

Table 5.2 shows that the results of the simulations compare very well with the experimental data. For the simulations with at least two FSI iterations, the motions are converging with a larger number of iterations. The convergence is visible in Figure 5.8. The motion amplitudes in the second-order simulations are closer to the experimental values than the first-order. The one iteration simulations more closely match the experimental values for relative phase angle than the simulations with more iterations, but the accuracy of the amplitudes are better with more iterations. Based on the presented data, the motions are nearly converged when using three iterations. Therefore, when not using explicit under-relaxation, three FSI iterations are performed to produce the results in the following sections.

5.3 Elastic Box Barge in Oblique Seas

Validation is performed on an elastic box barge in oblique seas. The barge has zero forward speed. The current method is compared to the results presented in *Senjanović et al.* (2008). This paper presents comparison of a numerical model to experiments that are reported earlier in *Remy et al.* (2006) and *Š. Malenica et al.* (2003). The model is a segmented barge consisting of twelve pontoons and a 1 cm x

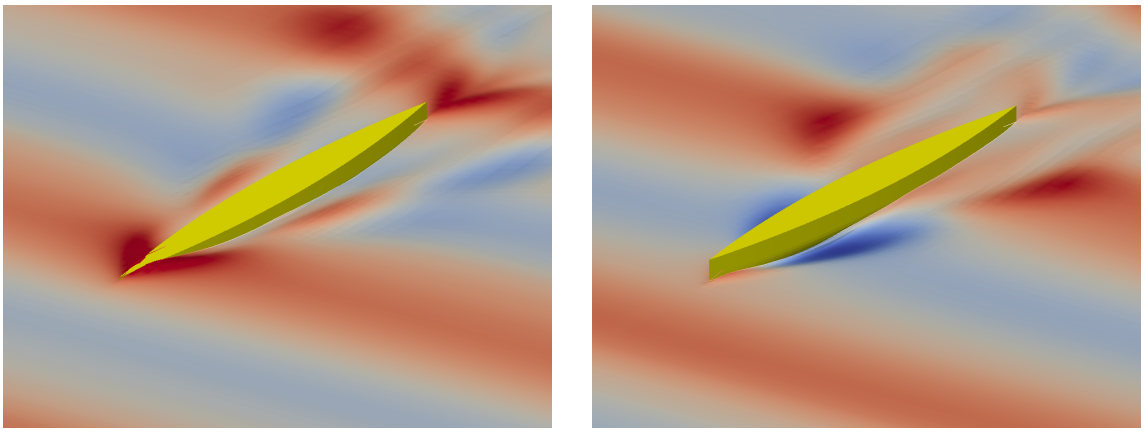

Figure 5.6: Wigley hull seakeeping in regular, head seas.

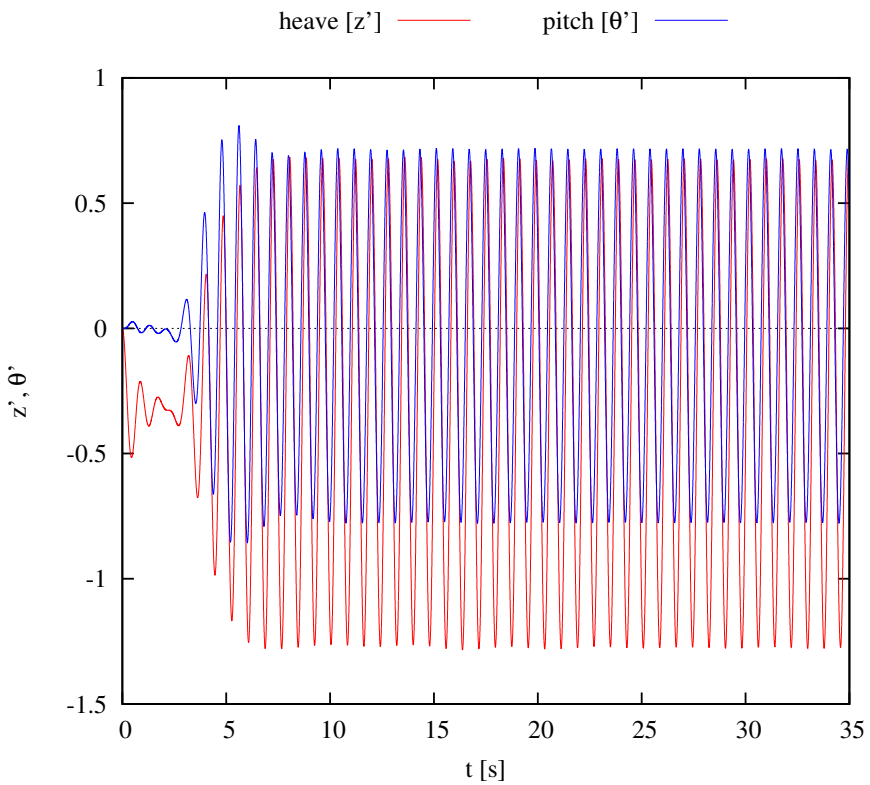

Figure 5.7: Wigley hull motions for three iteration, second order case.

	z'_a	α_z	θ'_a	α_θ	$\alpha_z - \alpha_\theta$	Time [hrs]
Experiments	0.97	$-73°$	0.75	$-39°$	$-34°$	-
1 itr* - 1^{st}	0.987	$-70.1°$	0.741	$-36.7°$	$-33.4°$	59.0
1 itr* - 2^{nd}	1.025	$-72.9°$	0.763	$-38.4°$	$-34.4°$	35.7
1 itr. - 1^{st}	0.992	$-75.0°$	0.752	$-40.5°$	$-34.5°$	16.0
1 itr. - 2^{nd}	1.018	$-76.4°$	0.763	$-41.6°$	$-34.8°$	17.0
2 itr. - 1^{st}	0.926	$-67.6°$	0.725	$-37.5°$	$-30.1°$	50.1
2 itr. - 2^{nd}	0.969	$-69.3°$	0.738	$-38.5°$	$-30.8°$	52.3
3 itr. - 1^{st}	0.950	$-70.8°$	0.733	$-39.5°$	$-31.3°$	69.1
3 itr. - 2^{nd}	0.973	$-71.7°$	0.743	$-40.5°$	$-31.2°$	69.8
4 itr. - 1^{st}	0.942	$-70.9°$	0.732	$-39.8°$	$-31.1°$	90.6
4 itr. - 2^{nd}	0.972	$-72.1°$	0.743	$-40.7°$	$-31.4°$	88.1
5 itr. - 1^{st}	0.947	$-71.2°$	0.732	$-39.9°$	$-31.3°$	103.8
5 itr. - 2^{nd}	0.973	$-72.3°$	0.743	$-40.9°$	$-31.4°$	105.2

Table 5.2: Wigley hull seakeeping response comparison: $\lambda/L = 1.0$, $H/\lambda = 1/75$, with 1^{st} and 2^{nd} order discretization, and different numbers of fluid-structure iterations. The simulations labled "1 itr*" use one fluid-structure iteration, and 3 iterations on the pressure equation.

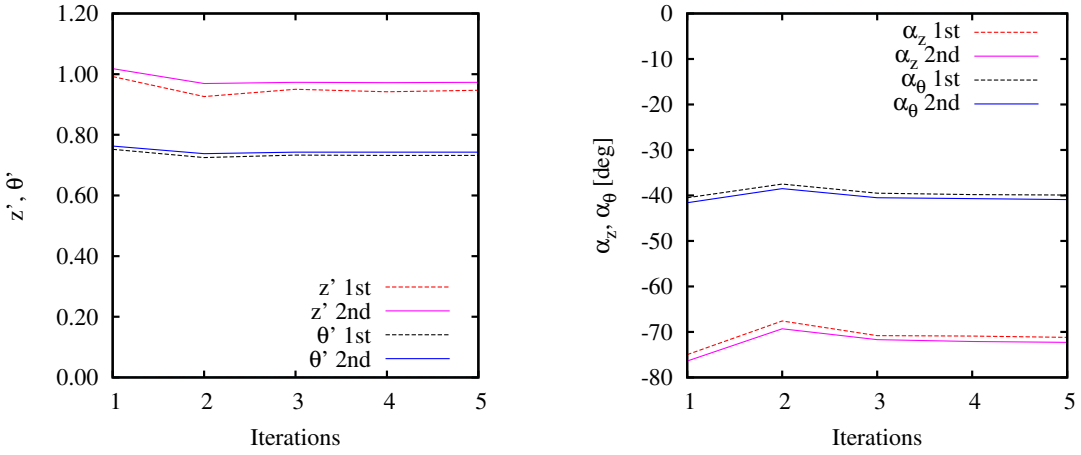

Figure 5.8: Convergence of Wigley hull motions over number of FSI iterations.

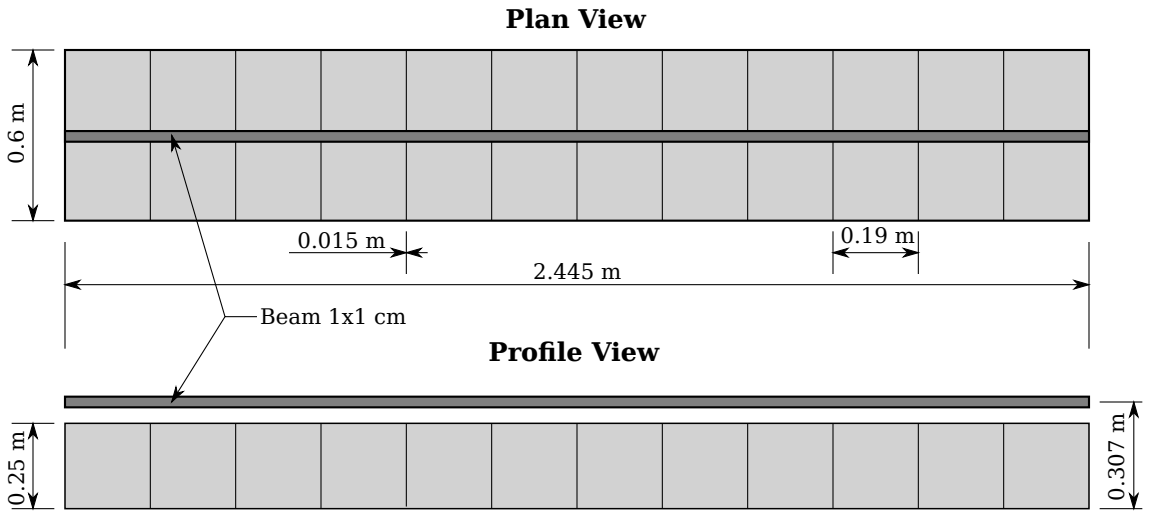

Figure 5.9: Segmented box barge in study

1 cm square bar connecting the pontoons. The bar is located above the pontoons to provide separation between the center of gravity and the shear center. This separation couples horizontal bending and torsion dynamically, similar to a container ship.

The total length of the barge is 2.445 m, consisting of 12 pontoons that are 0.19 m long separated by 0.015 m gaps. The beam is 0.6 m, the depth is 0.25 m, and the draft is 0.12 m. The center of the beam is located 0.307 m above the keel. The geometry is shown in Figure 5.9. The center of gravity is 0.163 m above the keel, giving 0.144 m of separation with the center of the beam. Figure 5.10 shows the numerical model of the barge in oblique seas, with the waves arriving from the lower right corner and propogating towards the upper left corner.

The structure of the barge is modeled as an Euler-Bernoulli beam as the beam is thin ($h/L = 1/244.5$). The material is steel ($E = 210$ GPa, $\nu = 0.3$, $\rho = 7800$ kg/m^3), giving bending stiffness $EI = 175$ N/m^2 and torsional stiffness $GJ = 115.38$ N/m^2. Point masses of 3.397158 kg, with inertia of 0.17389 kg-m^2 about the x-axis, are added at each node and offset to model the separation between the center of mass and the center of the beam. The shell consists of transfer elements, described in Section 3.3.2.

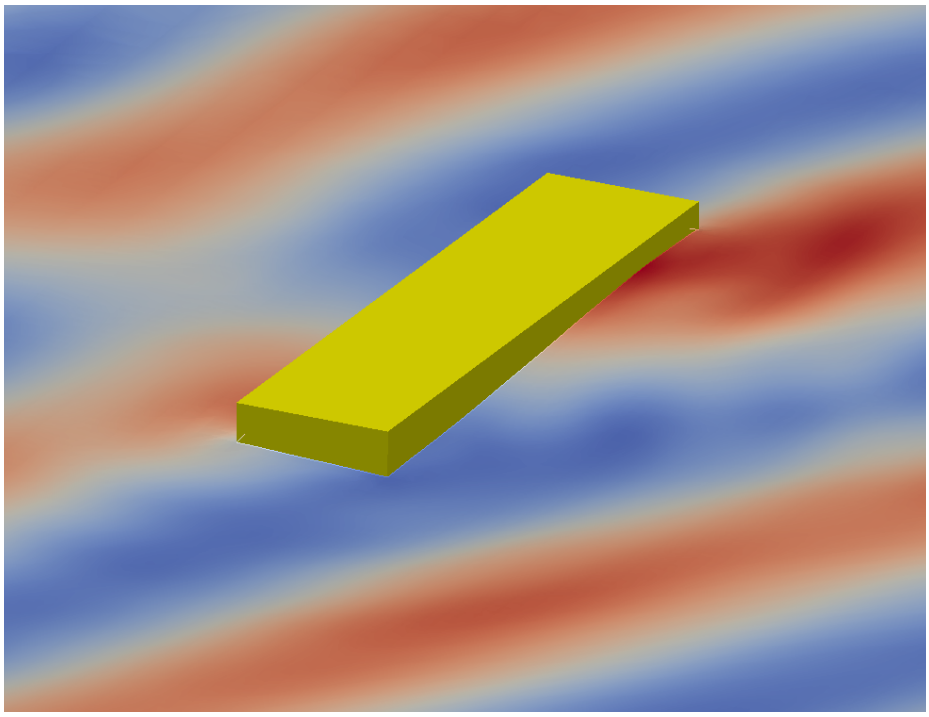

Figure 5.10: Box barge shown in oblique seas

The first three dry modes are shown in Figure 5.11. The first three dry natrual frequencies are 5.45, 5.69, and 7.27 rad/s from the current model, and the numerical values reported in *Senjanović et al.* (2008) are 5.21, 5.32, and 7.92 rad/s (the combined modes are also reported as 5.73 and 7.89 rad/s). When using the approximate body boundary condition, the change in hydrostatic pressure due to flexure is not acounted for. In these cases, springs are added to the model to represent the hydrostatics - vertical translational springs for the vertical motion and rotational springs for the roll/torsional motion.

Response amplitude operators (RAOs) of rigid body and elastic motion are compared to the results of *Senjanović et al.* (2008). The rigid body modes (heave, pitch, and roll) are obtained from the rigid body solver along with averages of the elastic motions to compare with the previously reported results. These averages are negligible in comparison to the rigid body solver motions, as would be expected. The elastic motions are described by differences in the rotations of the first and last pontoons:

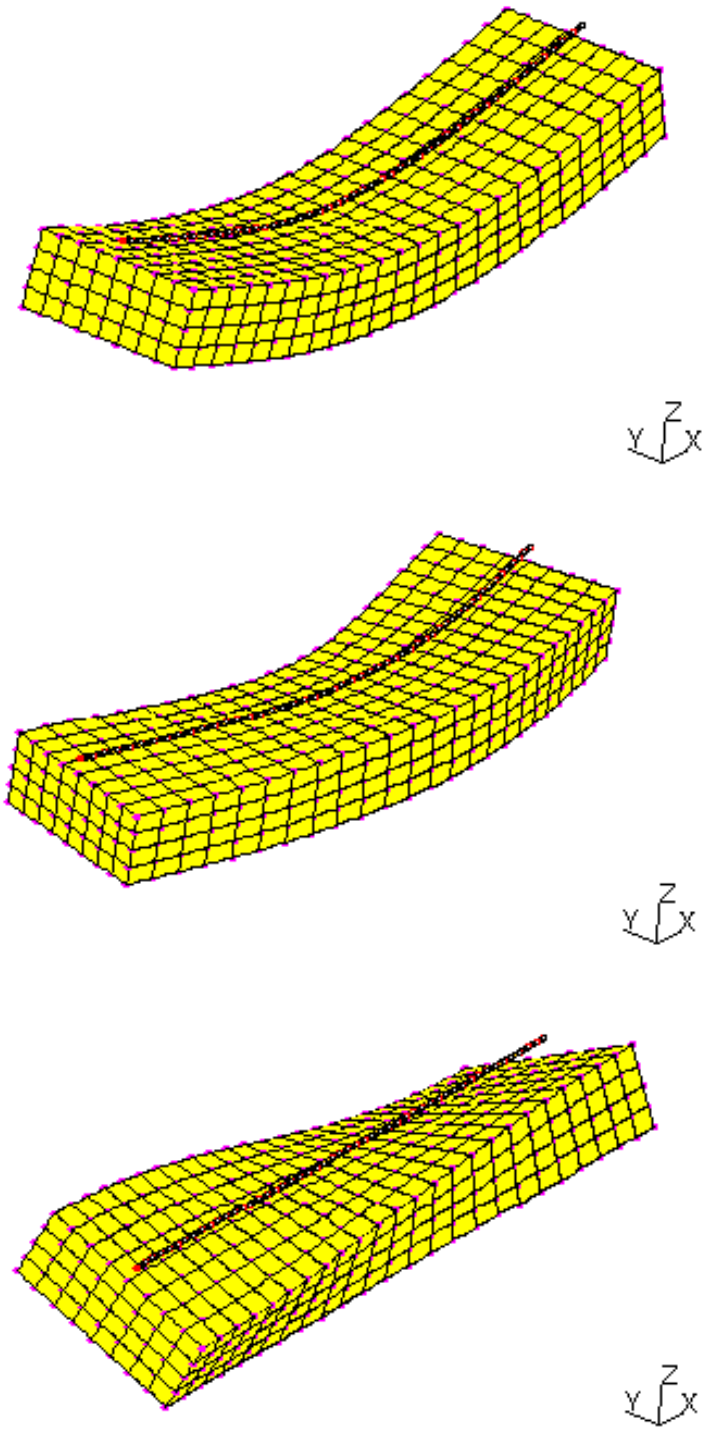

Figure 5.11: First three mode shapes of box barge. The second and thrid modes are coupled horizontal bending and torsion.

± 1.1275 m from midships. Figure 5.12 shows the RAOs from the current method compared with those previously presented as a function of wave period T.

The results marked "numerical" and "experimental" are from *Senjanović et al.* (2008). The numerical method in *Senjanović et al.* (2008) uses a modal description of the structure and linear hydrodynamics. Damping is added to the model from experience. The results from the current method are labeled "sims.", "damped sim.", and "refined sim.". The simulation labeled "damped sim." shows the effect of damping on the response while close to resonance, and the "refined sim." shows the effect of refining the model only in the transverse direction. The wave period of $T = 1.4$ s is close to the lowest combined horizontal bending and torsion frequency, resulting in resonance. The damped simulations have 3% critical damping ($\zeta = 0.03$) on the combined modes. This additional damping models the effects of the flow between the gaps in the pontoons, which should have the largest effect in the combined modes.

For the vertical, or symmetric, motions (heave, pitch, and vertical bending), there is excellent agreement between the experiments and the present method. For the antisymmetric response, the comparison is not quite as good. The roll and torsional motion can be seen to have too much damping at longer waves in the original simulations. This is due to a lack of resolution of the flow for those modes, as evidenced by the results of refined simulation (black triangles). The grid for this simulation was refined in the transverse direction to better capture the transverse flow. The roll motions show a very large improvement, while the torsion results are still over-damped. The flow induced by the torsional motion requires a very fine discretization to resolve, which is not performed in the current work.

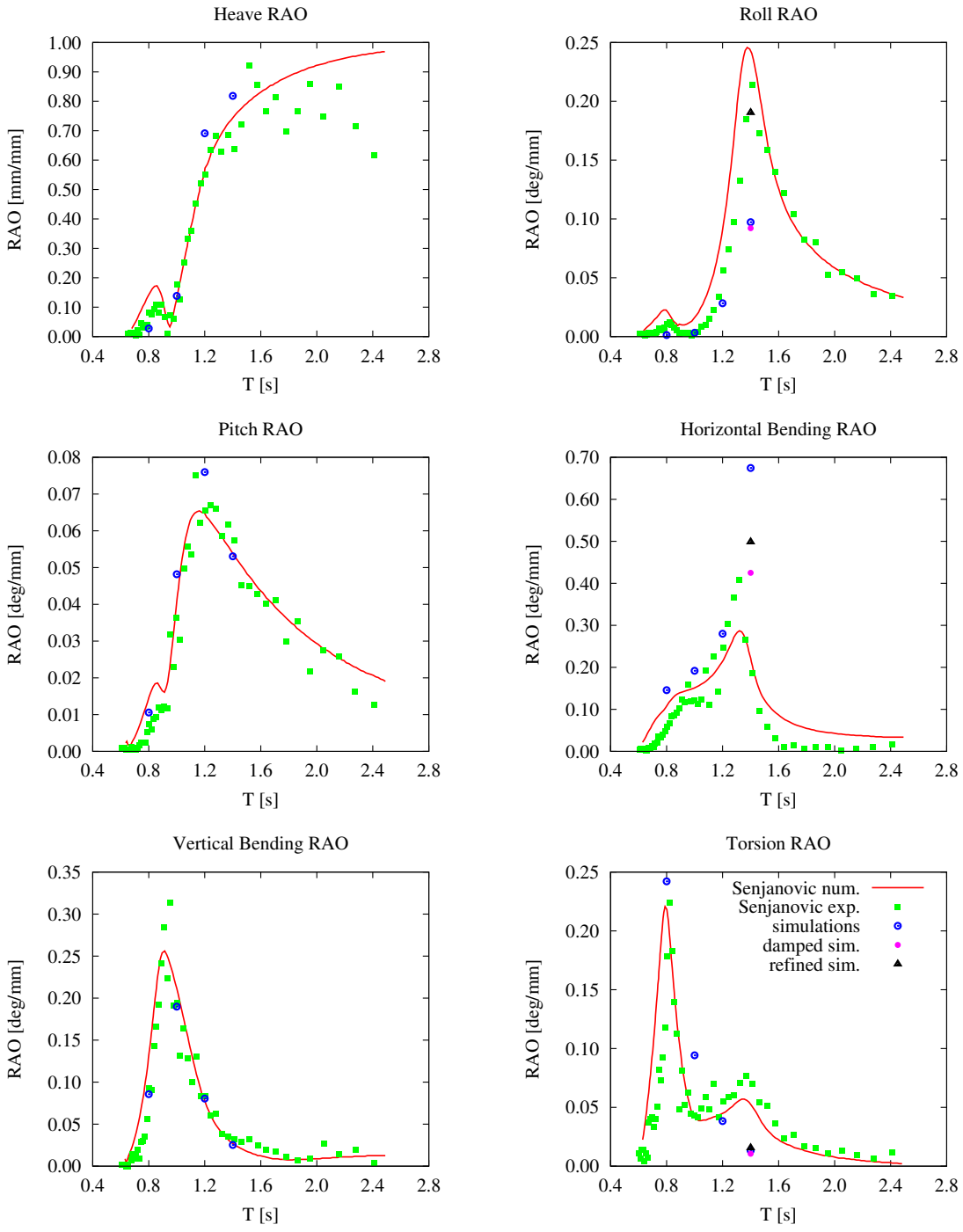

Figure 5.12: Comparison of RAOs between current simulations (open circles, dots, and triangles) and *Senjanović et al.* (2008) (solid line and filled squares). The RAOs are of heave (top left), pitch (middle left), roll (top right), vertical bending (bottom left), horizontal bending (middle right), and torsion (bottom right)

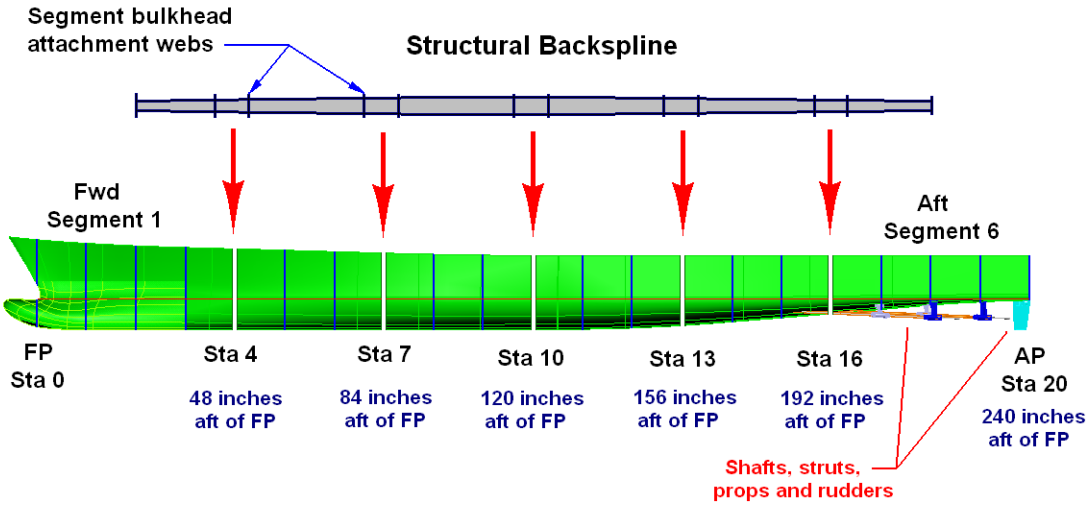

Figure 5.13: JHSS model layout.

5.4 JHSS Segmented Model in Head Seas

5.4.1 JHSS Model Tests

The Joint High Speed Sealift (JHSS) model, NSWCCD Model 5663, is a self-propelled segmented structural model that was built and tested in 2007. The model was tested in the Maneuvering and Seakeeping Basin (MASK) at the Naval Surface Warfare Center, Carderock Division (NSWCCD) in West Bethesda, MD. The structure of the model is provided by an aluminum backspline, similar to the box barge studied previously in Section 5.3. The model has $L_{pp} = 6.096$ m (240 in), with a maximum beam of 0.673 m (26.496 in) and draft of 0.180 m (7.091 in). The center of the backspline is located 0.229 m (9.0 in) above the keel. Figure 5.13 shows the model layout, with the backspline that extends between stations 2 and 18 (out of 20). More details about the model can be found in *Piro et al.* (2012).

The backspline is constructed from welded aluminum plates to generate the cross-section shape shown in Figure 5.14. The variation of the cross-section properties over the length of the backspline is described in Table 5.3. An equivalant section is

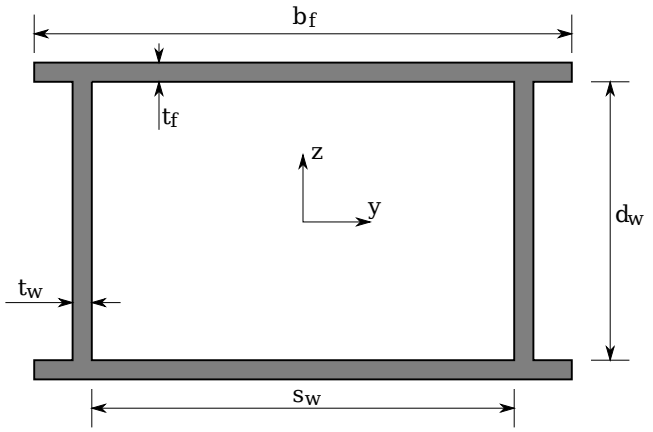

Figure 5.14: JHSS structural backspline cross-section geometry.

developed for station 2 to model the addition of reinforcing (2b) to the main section (2a).

Over 2000 tests were performed using the JHSS model. The tests examined here are the regular wave, head seas runs with forward speed. The wave length for all of the cases examined herein is equal to the length of the model: 6.096 m. The wave slopes defined as H/λ tested are 1/15, 1/30, and 1/50. The speeds are 5, 15, 25, 35, and 45 knots full scale, or 0.373, 1.119, 1.866, 2.612, and 3.358 m/s model scale. The more severe cases (1/15 wave slope or 1/30 wave slope at high speed) are of interest because of the extreme slam-induced whipping response. The cases tested here are 15 knots, 1/15 wave slope; 15 knots, 1/30 wave slope; and 35 knots, 1/30 wave slope. Figure 5.15 shows pictures of the model in Run 478 (15 kts, 1/15 wave slope) in extreme hogging and sagging conditions. The violence of the slamming events is evident in these pictures.

5.4.2 Numerical Set-up

The structural model uses beam finite elements with cross-sections that vary linearly with axial position. One element is used between each station, with a total of 18 elements. The properties of the half stations at the ends are not used because the

	Section Size [cm]					Inertias [cm4]		
Station	b_f	t_f	d_w	t_w	s_w	I_{zz}	I_{yy}	J
2a	5.226	0.4763	4.597	0.4763	4.273	39.825	36.098	62.334
2b	6.178	0.0000	6.386	0.6350	5.225	27.560	69.909	58.030
2	-	-	-	-	-	67.385	106.007	120.364
2.5	10.221	0.4763	4.896	0.4763	4.754	79.735	116.716	77.917
3	10.160	0.4763	5.316	0.4763	5.408	93.267	127.172	103.174
4	9.901	0.4763	6.244	0.4763	6.706	125.980	153.843	171.341
5	10.224	0.4763	7.042	0.4763	7.968	165.523	204.514	255.749
6	11.648	0.4763	7.654	0.4763	9.147	219.164	294.379	347.063
7	13.150	0.4763	8.190	0.4763	10.207	279.040	403.224	443.787
8	14.219	0.4763	8.646	0.4763	11.106	333.328	504.540	538.348
9	14.833	0.4763	8.975	0.4763	11.807	373.132	581.643	617.643
10	14.986	0.4763	9.133	0.4763	12.265	390.255	620.344	667.242
11	14.656	0.4763	9.089	0.4763	12.457	379.136	612.051	676.532
12	14.087	0.4763	8.813	0.4763	12.409	344.022	570.472	643.010
13	13.635	0.4763	8.249	0.4763	12.158	291.969	514.889	567.194
14	13.600	0.4763	7.375	0.4763	11.750	231.685	462.275	458.865
15	13.858	0.4763	6.414	0.4763	11.221	177.852	420.342	350.823
16	14.189	0.4763	5.651	0.4763	10.611	141.440	392.256	270.320
17	14.478	0.4763	5.058	0.4763	9.962	116.121	372.209	211.610
17.5	14.610	0.4763	4.852	0.4763	9.637	108.084	365.768	190.861
18	14.732	0.4763	4.686	0.4763	9.313	101.898	360.788	173.742

Table 5.3: Strutural properties of JHSS model backspline.

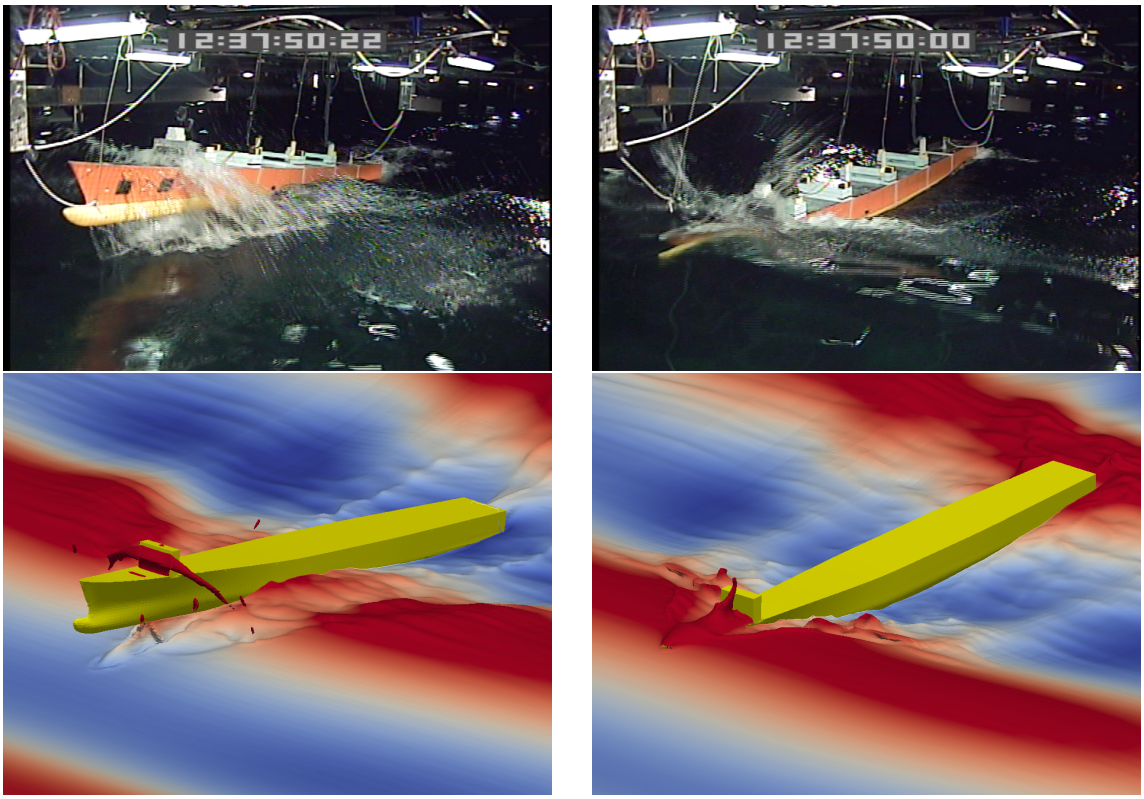

Figure 5.15: JHSS model in Run 478: 15 kts, 1/15 wave slope. Top row is from the experiments and bottom row is from the fine resolution simulations at similar times.

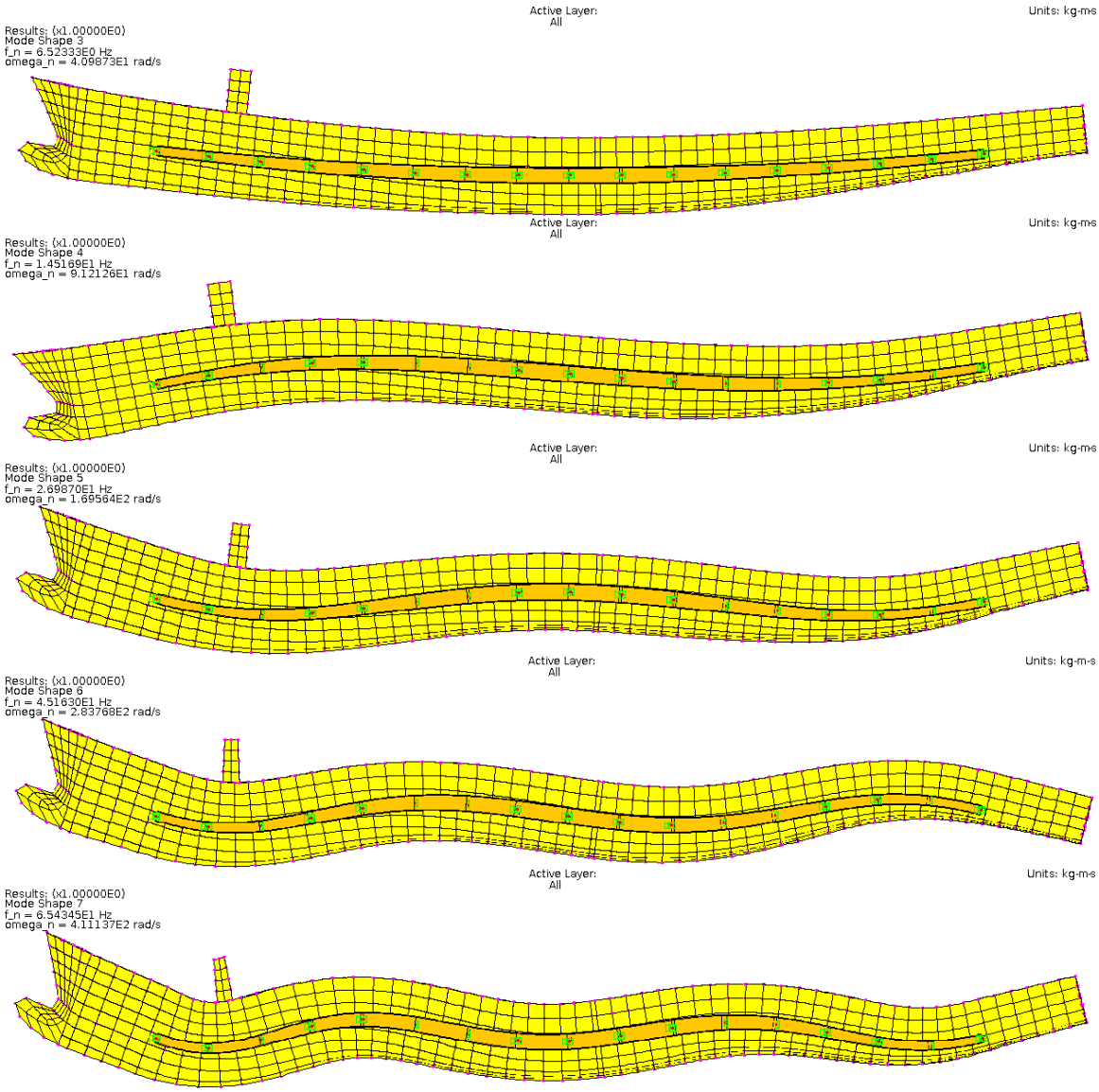

Figure 5.16: First five dry mode shapes of JHSS numerical model.

free-free boundary conditions make the stiffness at the ends of the beam less important. The shell is discretized with transfer elements. Five modes are generated from the finite-element model, as the experimental model has only six segments. The five dry mode shapes are shown in Figure 5.16.

Two computational grids with uniform cells near the vessel are used, with approximately 1.1 and 3.8 million cells. The grids have approximately 163 and 244 cells along the vessel length, and 14 and 21 cells along the depth at the bow. The back-

ground grids are generated in the `Pointwise` mesh generation program which allows for easily generated grids with larger cells farther from the body. The `snappyHexMesh` utility available in OpenFOAM is used to fit the uniform background grid to the vessel surface. Due to the symmetry of the problem, only half of the body is modeled. The domain is approximately $5.0L_{pp}$ in the longitudinal direction, $1.3L_{pp}$ in the transverse direction, and $1.0L_{pp}$ in the vertical direction for all grids. The coarse mesh on the hull is shown next to the shell mesh from the structural model in Figures 5.17 and 5.18. The fluid mesh is shown in yellow, and the structural mesh in orange.

A more efficient refinement method is sought that can combine the speed of the coarse grid simulations while maintaining the resolution of the finer grids where it is needed for slamming. Therefore, the `snappyHexMesh` utility is used to add a refinement block in the bow region of the coarse grid. Figure 5.19 shows a side view of the bow portion of the refined model. The hull is shown in orange and the centerplane in light-blue, with the cell boundaries marked in dark-blue. It is clear from the image that only the region forward of the nominal superstructure is refined. Each cell in the refined region is one-eighth the volume of a cell in the coarse grid (one-half the length in each direction), but the total number of cells is still under 1.2 million. The refined region spatially resolves the impact flow and water-on-deck more accurately, as there are now approximately 29 cells along the depth at the bow. This number is still smaller than was found neccessary for the two-dimensional wedge impact, and thus even more refinement is expected to make an effect on accuracy. The simulations are preformed in parallel, with 36 processors for the coarse and refined grids, and 72 processors for the fine grid. Run on the University of Michigan's Center for Advanced Computing cluster, the simulations on the coarse grid take between about 26 and 40 hours to run to 30 seconds of model-scale time. The simulation times on fine grid are between 34 and 233 hours for 30 seconds of simulation time. For the coarse grid refined in the bow region, the simulation times are about 24 to 86 hours. Unfortu-

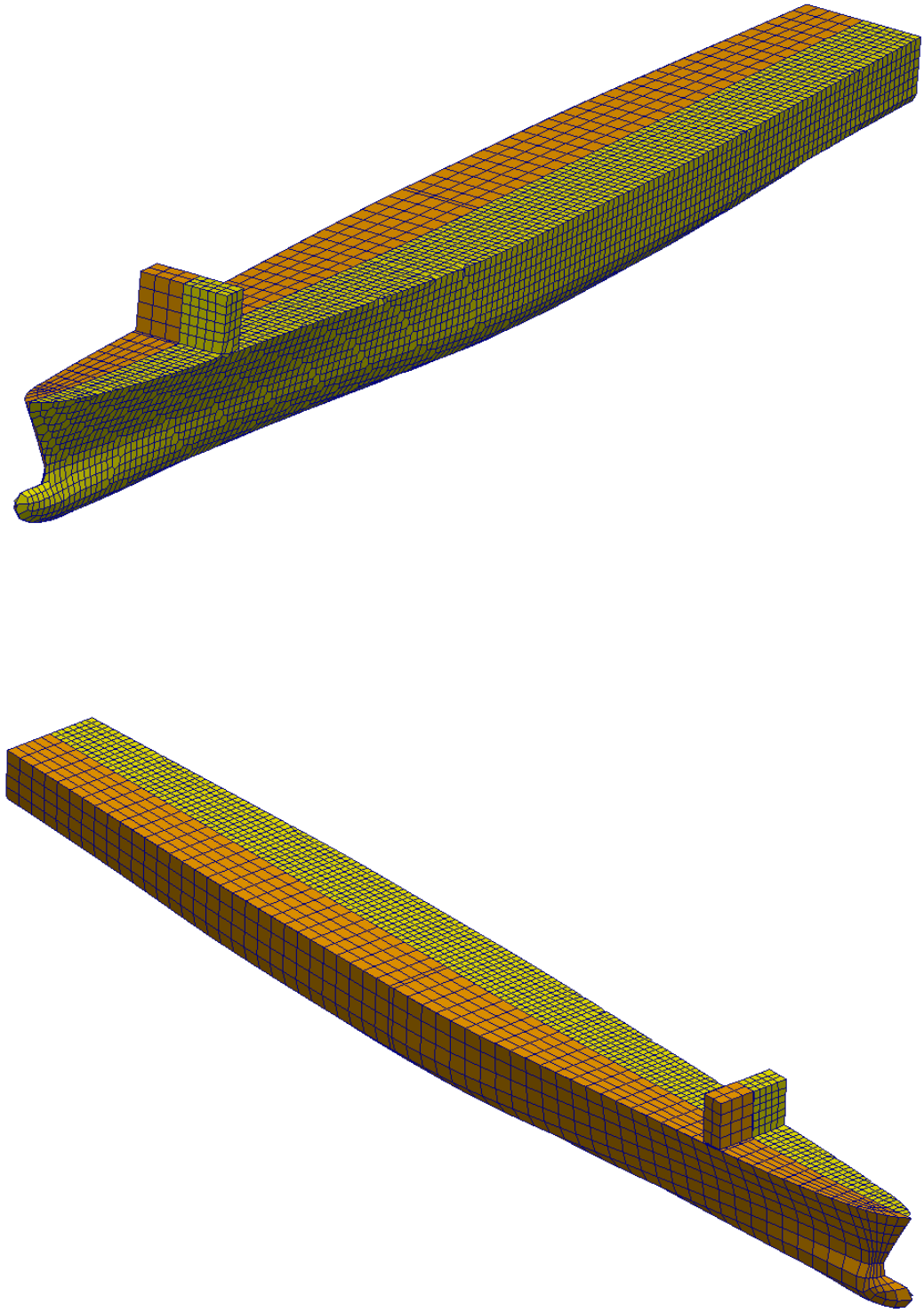

Figure 5.17: JHSS fluid and structrual meshes on hull, views from above. The coarse fluid mesh is shown in yellow and the structural mesh in orange.

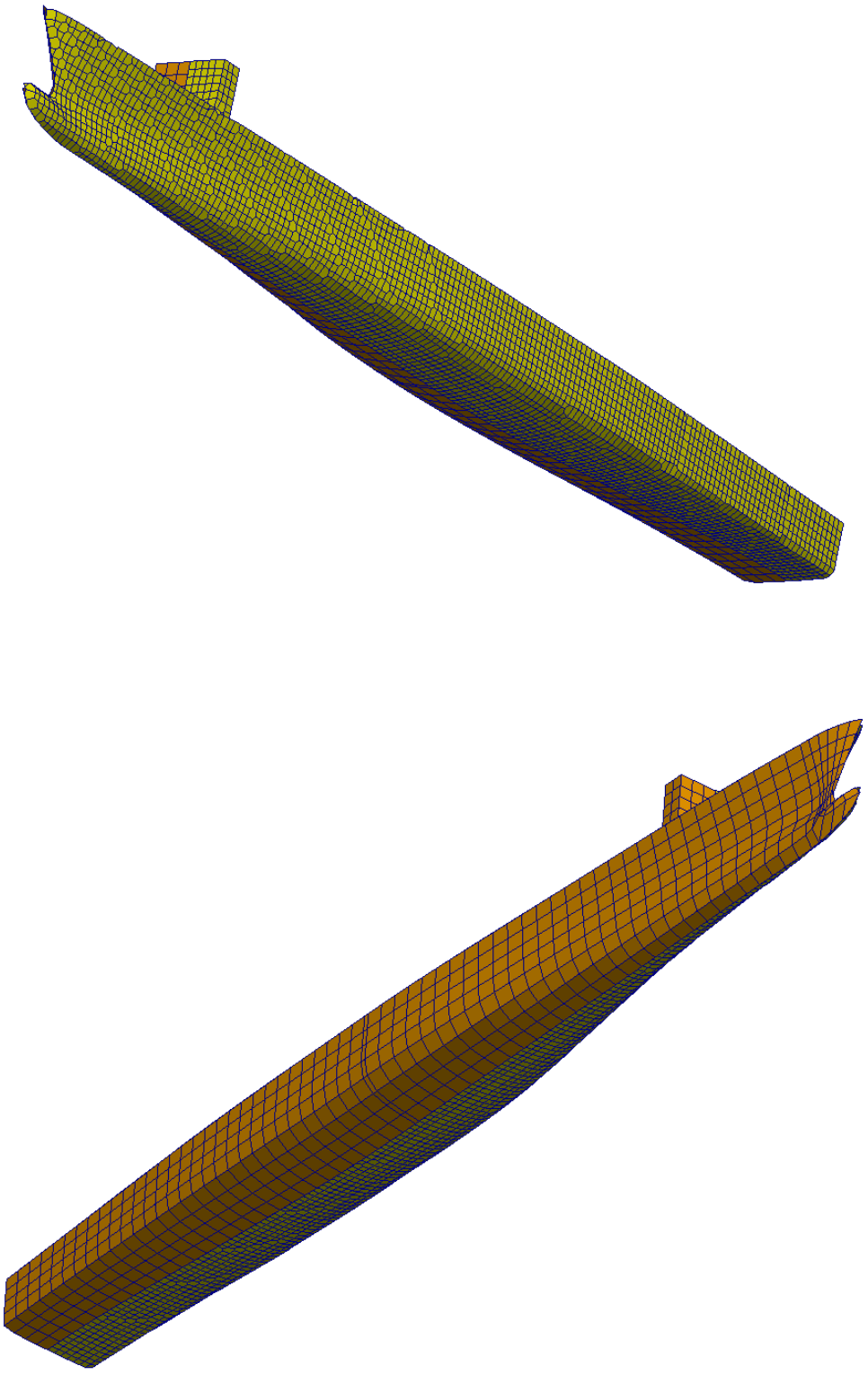

Figure 5.18: JHSS fluid and structural meshes on hull, views from below. The coarse fluid mesh is shown in yellow and the structural mesh in orange.

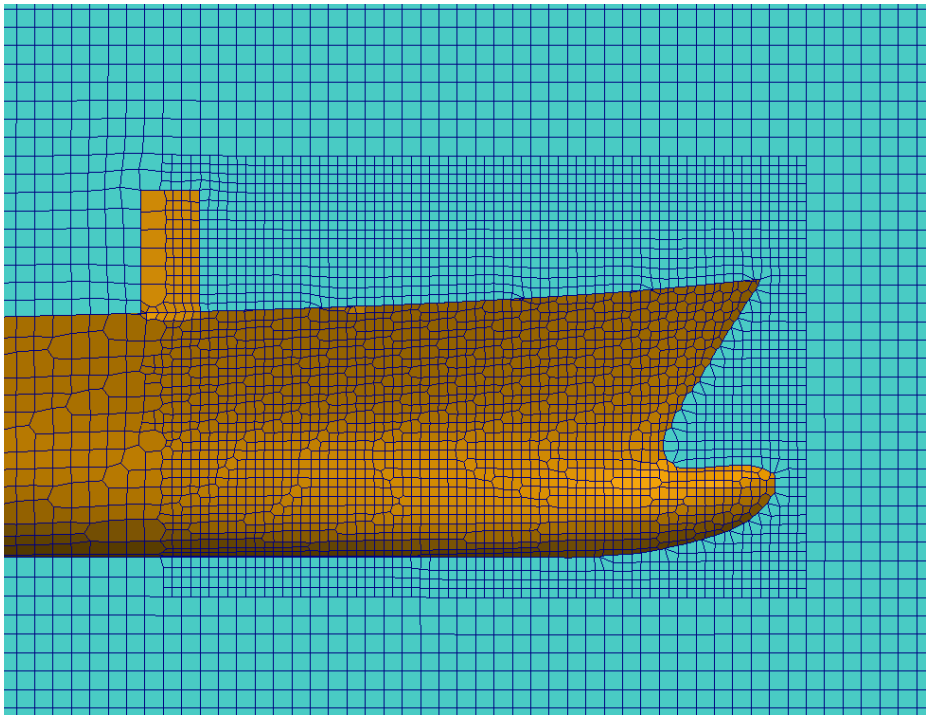

Figure 5.19: JHSS coarse grid with refinement block

natley, these simulation times are influenced by more factors than the grid size and case set-up: some computers and connections are faster than others in the cluster. Therefore, the simulation times should not be taken as fixed, repeatable values.

5.4.3 Results and Analysis

The results on the three different grids are compared. First, the green water on deck after an impact is show in Figure 5.20. The free surface (colored by elevation) is shown at the same time on each grid, with the left column showing a view off the port bow, and the right column showing a view from the top. From this figure, the resolution of the water-on-deck is visible, with the coarse grid retaining much less water-on-deck than the other two grids. Even though the motions are not much different between the coarse grid and the coarse grid refined in the bow region, the amount of the water-on-deck is much greater with refinement.

A further comparison of the three grids is shown in the seakeeping response for all

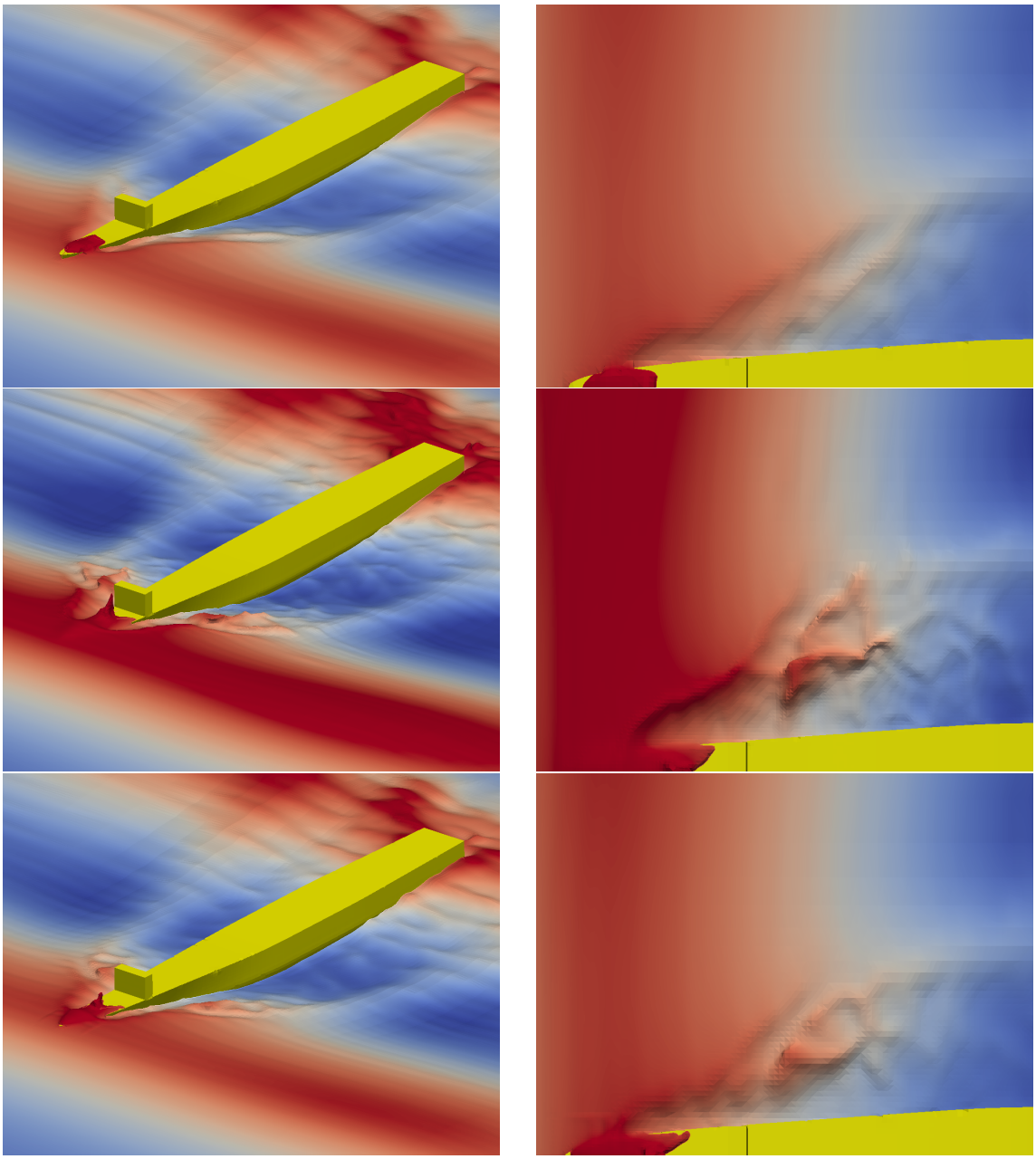

Figure 5.20: JHSS impact flow for different grids. The top row is the coarse grid, the middle row is the fine grid, the bottom row is the coarse grid with refinement. The left column contains views from the front and above, and the right column contains views for the bow from directly above.

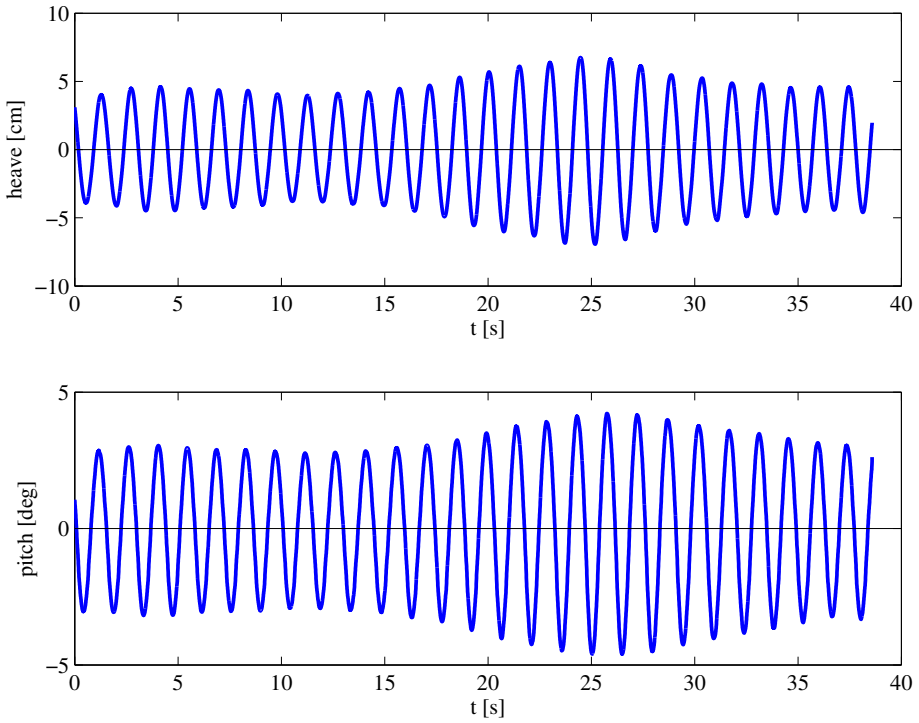

Figure 5.21: JHSS experiment: full rigid body motion time series - 15 knots, 1/30 wave slope (Run 490).

three cases. The experimental response is also shown in the same plots. To note the difficulty of the comparison between the simulations and experiments, Figure 5.21 is included, showing the full experimental time series for run 490 (15 knot, 1/30 wave slope). In this figure it can be seen that the experimental runs do not exhibit perfect steady-state behavior. Therefore, only the portions of the experimental time series that are close to steady state (0-15 s in this figure) are used in the comparisons. The comparison for the 15 knot, 1/15 wave slope case is shown in Figure 5.22, the 15 knot, 1/30 wave slope case in Figure 5.23, and the 35 knot, 1/30 wave slope case in Figure 5.24. The figures highlight the increased resolution of the waves and the motion between the coarse and fine grids. For the 35 knot, 1/30 wave slope case especially, the motions from the refined coarse grid and fine grid are very close. Also of note is that the pitch comparison is much better than heave for the lower speed runs, which underpredicts the experiments.

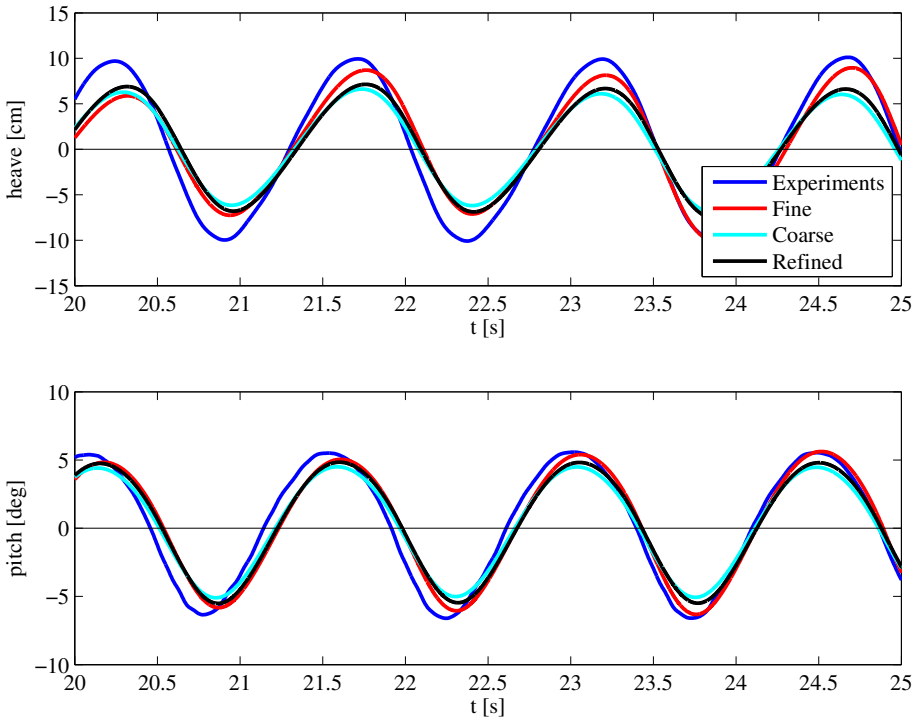

Figure 5.22: JHSS seakeeping comparison between experiments and three grids: 15 knots, 1/15 wave slope case.

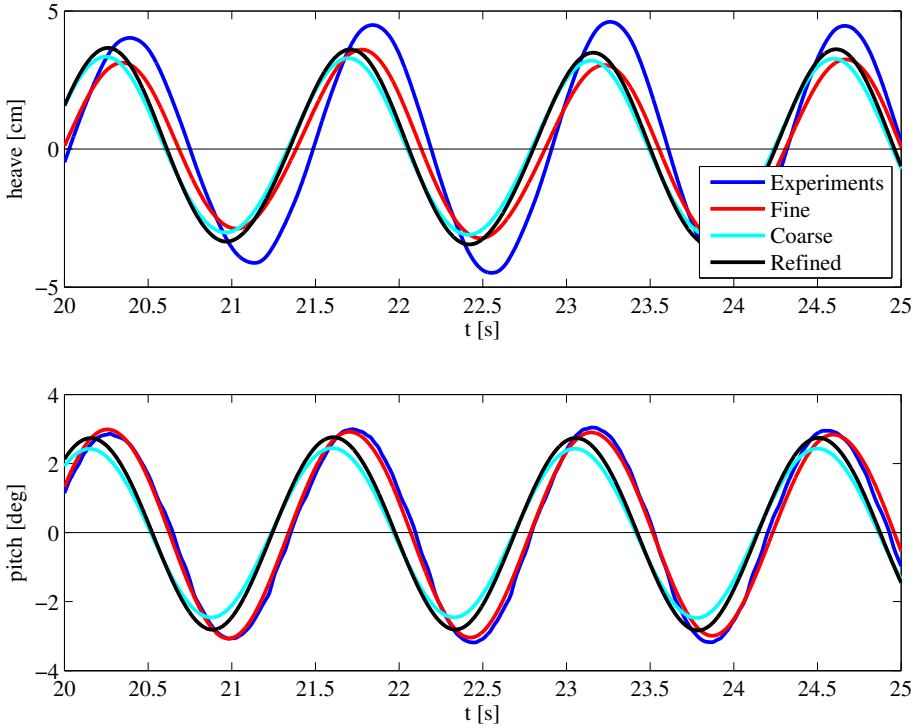

Figure 5.23: JHSS seakeeping comparison between experiments and three grids: 15 knots, 1/30 wave slope case.

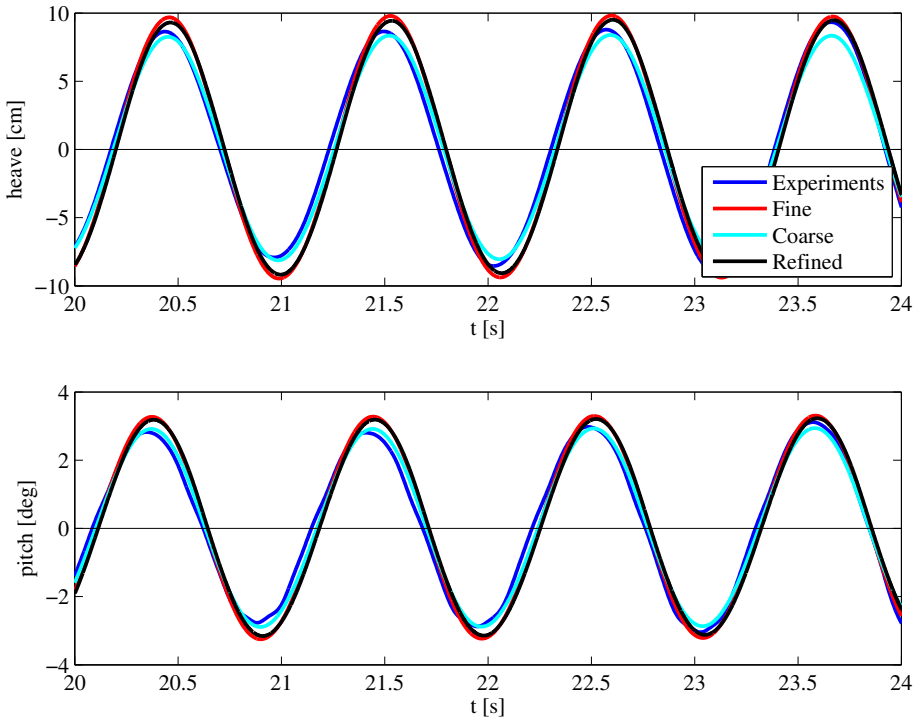

Figure 5.24: JHSS seakeeping comparison between experiments and three grids: 35 knots, 1/30 wave slope case.

Along with the rigid body motions, the vertical bending moment of the backslpine at midships is examined. The bending moment is studied both using the time series data, as well as broken down into frequency content. The frequency content is calculated using the fast fourier transform (FFT). Because the experimental model is self-propelled, the speed is not constant during the simulation, causing the encounter frequency to vary throughout each run, while the model is fixed in surge for the simulations. Experimental surge velocity information obtained by integrating accelerometer data gives the amplitude of the surge velocity to be about 0.2 m/s for run 478, 0.1 m/s for run 490, and 0.15 m/s for run 499. These surge velocities change the encounter frequency by up to ± 0.03 Hz, or about 5% of the enounter frequency for the 15 knot cases. The corresponding range of encounter period for the 15 knot cases is 1.39 s to 1.52 s. Therefore, the an exact match cannot be made between the experimental and simulation time series, but the amplitudes of the motions and

structural response should be comparable.

The results for the coarse mesh (1.1 million cells) are shown first. Midship bending moment time series are compared in Figures 5.25 to 5.27, and then FFTs in Figures 5.28 to 5.30. The time series are shown in their raw form, as well as filtered below and above 3 Hz, labeled low and high frequency, respectively.

With the coarse discretization, the wave induced bending moment is under-predicted by the simulations, similar to the heave motion under-prediction. The basic shape of the low-frequency (wave-induced) signal is captured by the simultions, but not all of the details are resolved. The high frequency time-series in Figure 5.25 shows that the slam induced impulses are not fully resolved, and that the damping is also not captured in the simulations. More structural damping is added to the finer simulations. The high frequency content of the 15 knot, 1/30 wave slope case is not captured by the simulations, shown in Figure 5.26. The high frequency results for the 35 knot, 1/30 wave slope case compare favorably to the experiments for some wave encounters, seen in Figure 5.27.

The frequency spectra are used to further examine the midship bending moment. Note for this analysis, the frequency resolution of the FFT is dependent on the length of the signal. For the 15 knot cases, the length of the experimental runs is greater than the steady portion of the simulations. For the 35 knot case, the length of the experimental data is shorter due to the limitations in the size of the basin. Therefore, the simulation FFTs are less resolved for the slower speed relative to the experiments, and more resolved for the higher speed. The low frequency response appears to be very poorly resolved, contrary to indication of the time series. For the 15 knot, 1/15 wave slope case, Figure 5.28 shows the experimental response in the frequency range of 4-5 Hz is not captured well by the simulations, and the response between 5 and 6 Hz is over predicted. This indicates a lack of resolution of the added mass as well as the damping. Figure 5.29 shows the lack of resolution of the high frequency response for

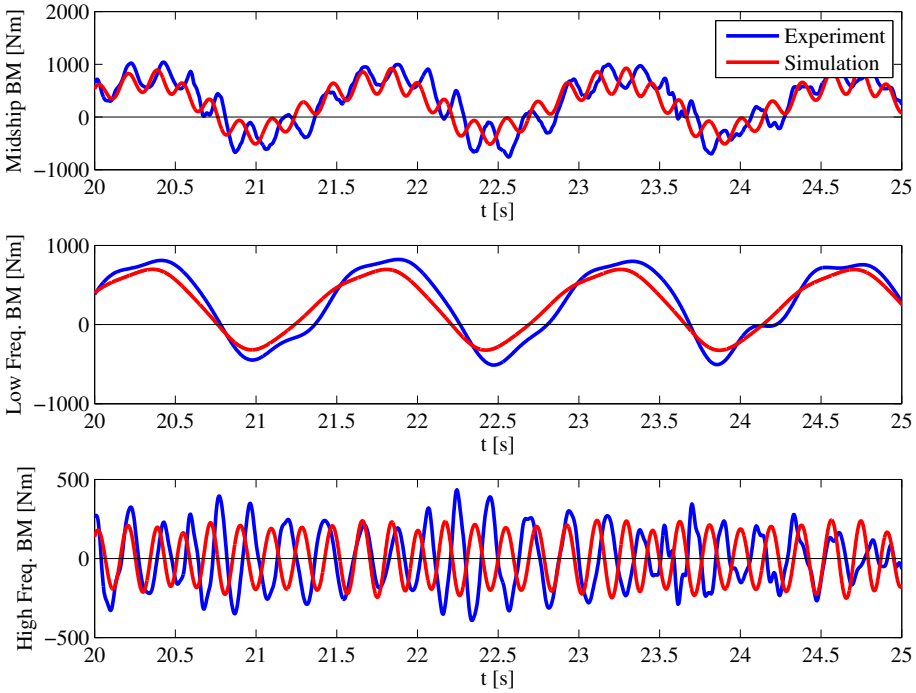

Figure 5.25: JHSS coarse grid: midship bending moment time series comparison - 15 knots, 1/15 wave slope.

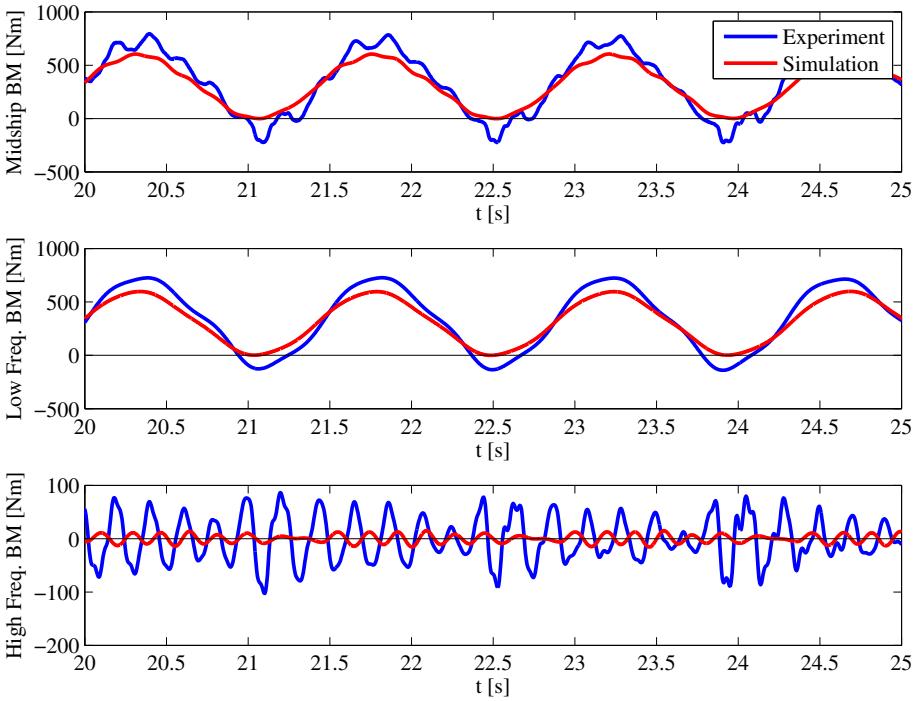

Figure 5.26: JHSS coarse grid: midship bending moment time series comparison - 15 knots, 1/30 wave slope.

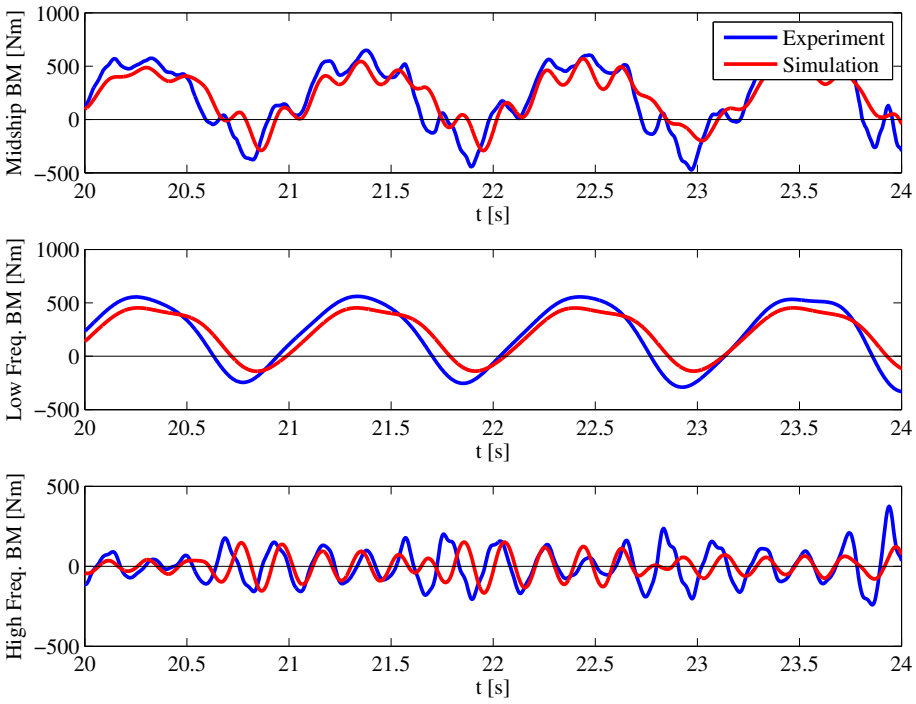

Figure 5.27: JHSS coarse grid: midship bending moment time series comparison - 35 knots, 1/30 wave slope.

the 15 knot, 1/30 wave slope case. The response is relatively well captured by the simultions for the 35 knot, 1/30 wave slope case, as evidenced in Figure 5.30.

Next the results are shown for the fine resolution mesh (3.8 million cells). Midship bending moment time series are compared to the experiments in Figures 5.31 to 5.33. The wave-induced bending moment again compares well between the simulations and experiments for all three cases. The initial amplitude of the ringing respone is comparable between the simulations and experiments for the 15 knot, 1/15 wave slope case (Figure 5.31), but there is now too much damping added to the model. Unfortunately, due to a harmonic of the forcing frequency nearly matching the first wet flexural natural frequency in simulations, the damping needed to be added to the model to prevent the resonant response growing too large. For the 15 knot, 1/30 wave slope case, shown in Figure 5.32, the ringing response is again not captured, but is larger than the high frequency response for the coarse grid. The high-frequency

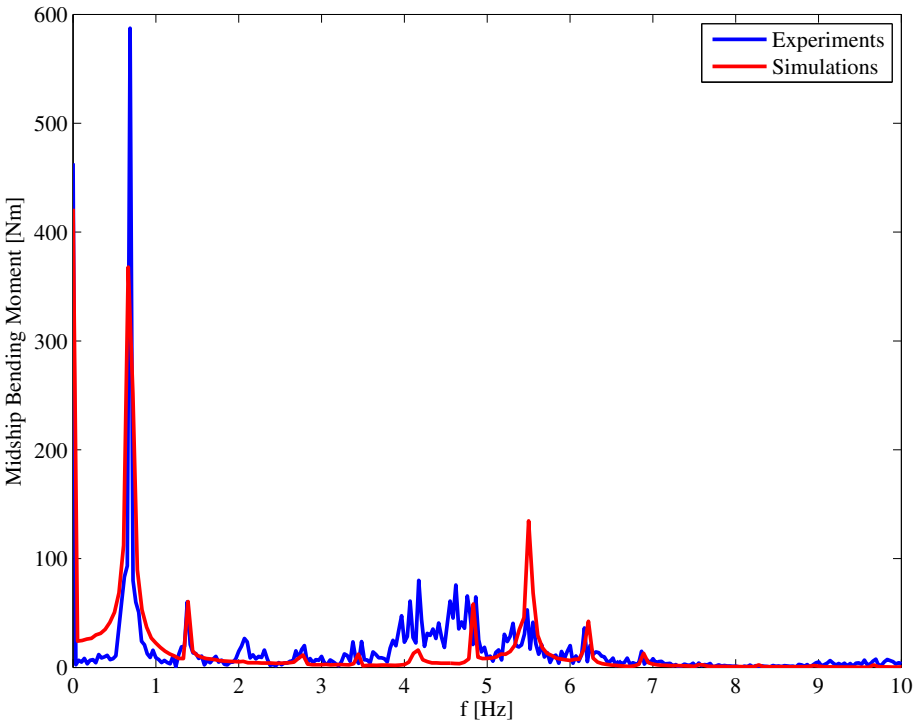

Figure 5.28: JHSS coarse grid: midship bending moment FFT comparison - 15 knots, 1/15 wave slope.

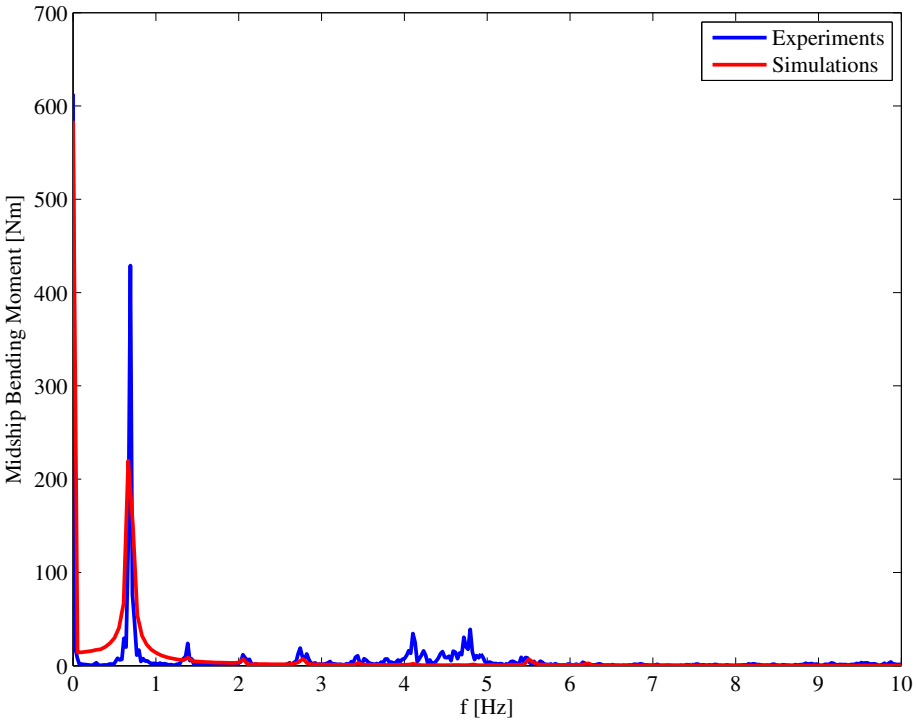

Figure 5.29: JHSS coarse grid: midship bending moment FFT comparison - 15 knots, 1/30 wave slope.

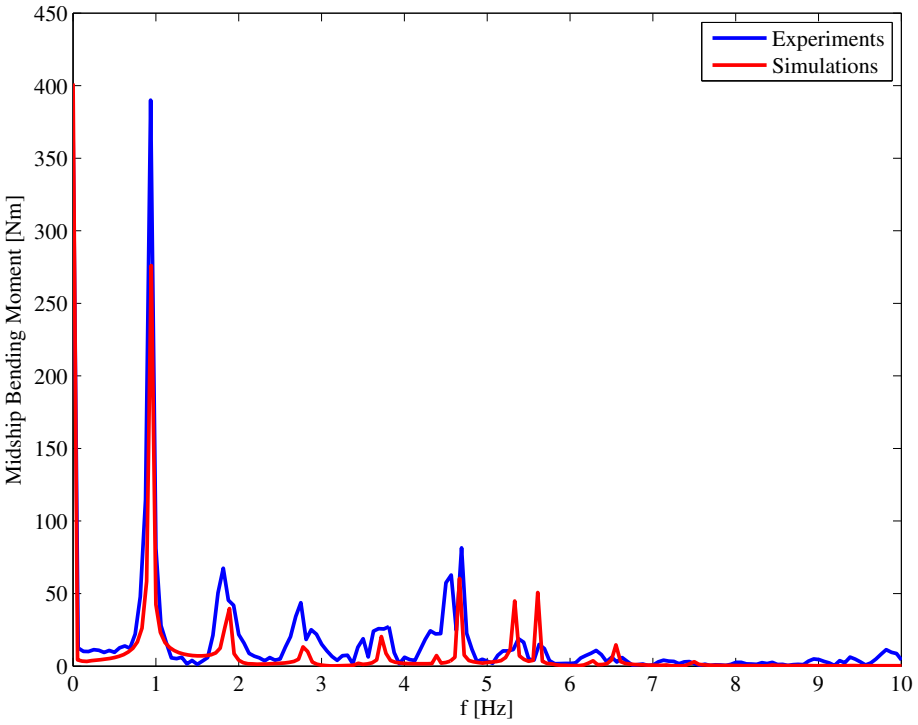

Figure 5.30: JHSS coarse grid: midship bending moment FFT comparison - 35 knots, 1/30 wave slope.

bending moment for the 35 knot, 1/30 wave slope case predicted by the simulation is close in amplitude and frequency to the experimental values for most of the range shown in Figure 5.33.

The bending moment FFTs for the medium grid are shown in Figures 5.34 to 5.36. The fine grid captures more of the 4-5 Hz range response for the 15 knot, 1/15 wave slope case, seen in Figure 5.34, than the coarse grid. The harmonics near 2 and 3 Hz are also captured more accurately. Figure 5.35 shows that for the 15 knot, 1/30 wave slope case, the 4-5 Hz response is still not captured in the simulations. The 35 knot, 1/30 wave slope case shows relatively good agreement between the simulations and experiments, though not all of the response in the 3-5 Hz range is captured, as can be seen in Figure 5.36.

The same results for the uniform grids are now examined for the refined coarse grid. The midship bending moment time series are included from Figures 5.37 to 5.39.

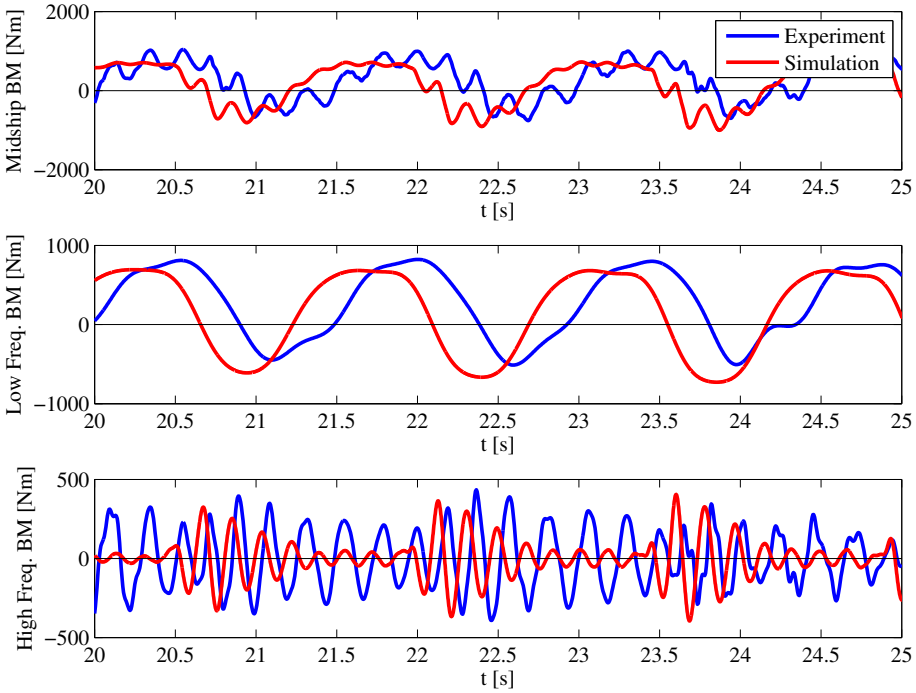

Figure 5.31: JHSS fine grid: midship bending moment time series comparison - 15 knots, 1/15 wave slope.

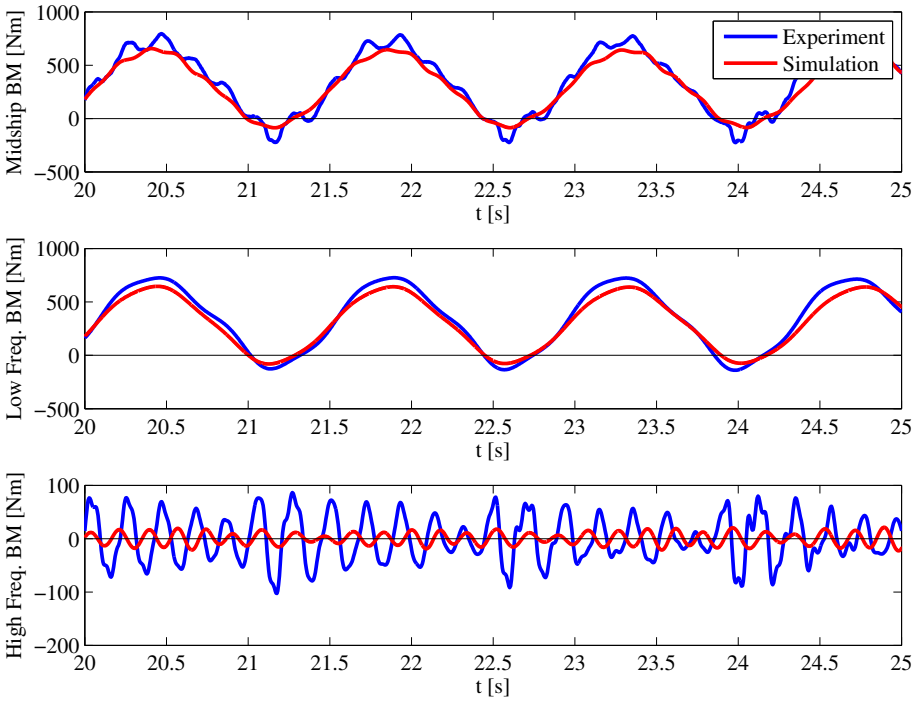

Figure 5.32: JHSS fine grid: midship bending moment time series comparison - 15 knots, 1/30 wave slope.

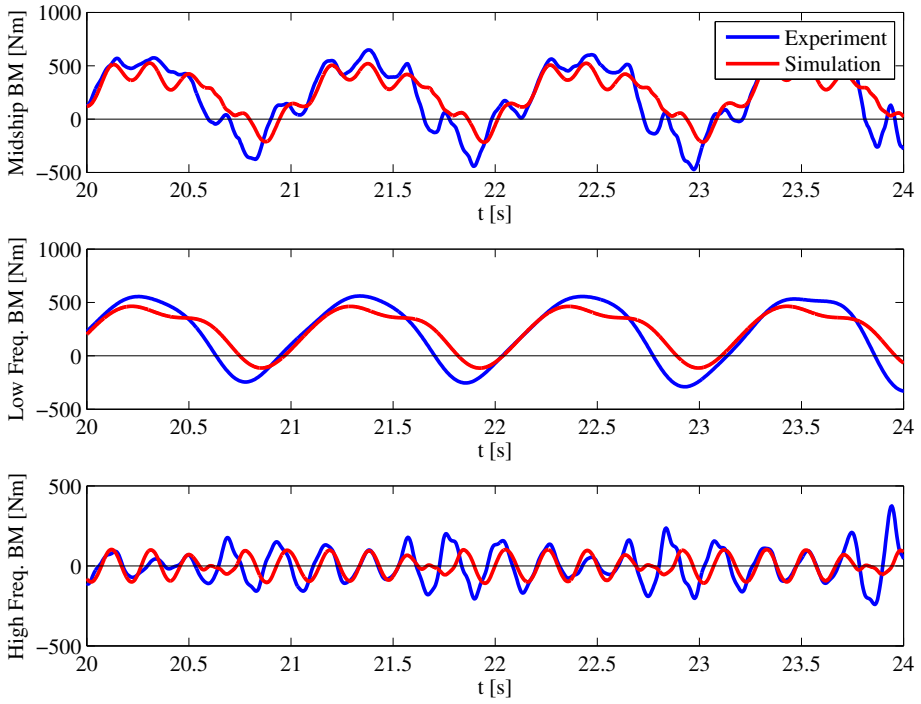

Figure 5.33: JHSS fine grid: midship bending moment time series comparison - 35 knots, 1/30 wave slope.

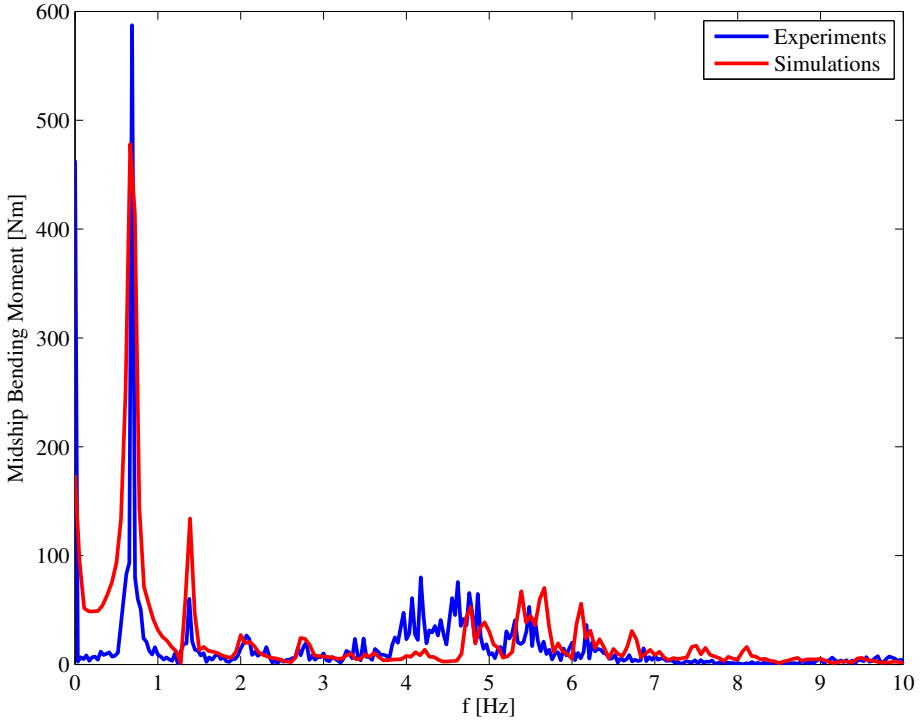

Figure 5.34: JHSS fine grid: midship bending moment FFT comparison - 15 knots, 1/15 wave slope.

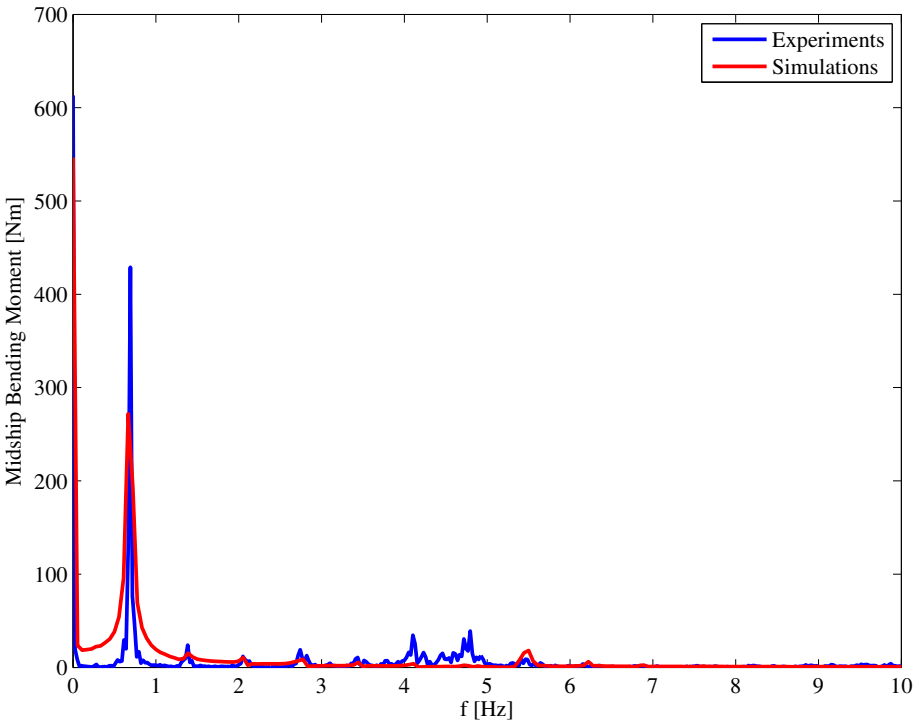

Figure 5.35: JHSS fine grid: midship bending moment FFT comparison - 15 knots, 1/30 wave slope.

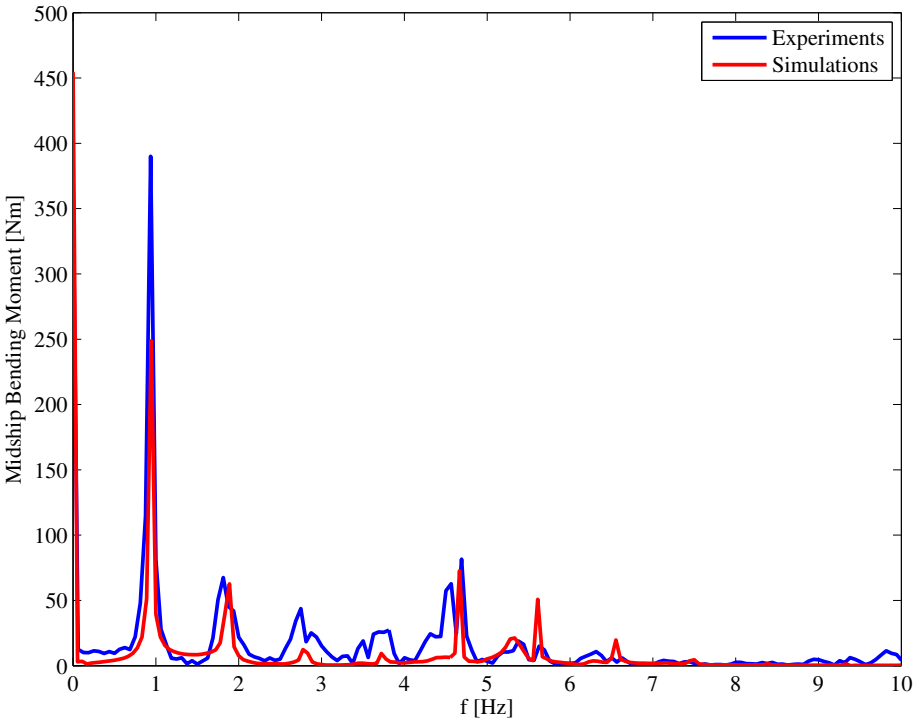

Figure 5.36: JHSS fine grid: midship bending moment FFT comparison - 35 knots, 1/30 wave slope.

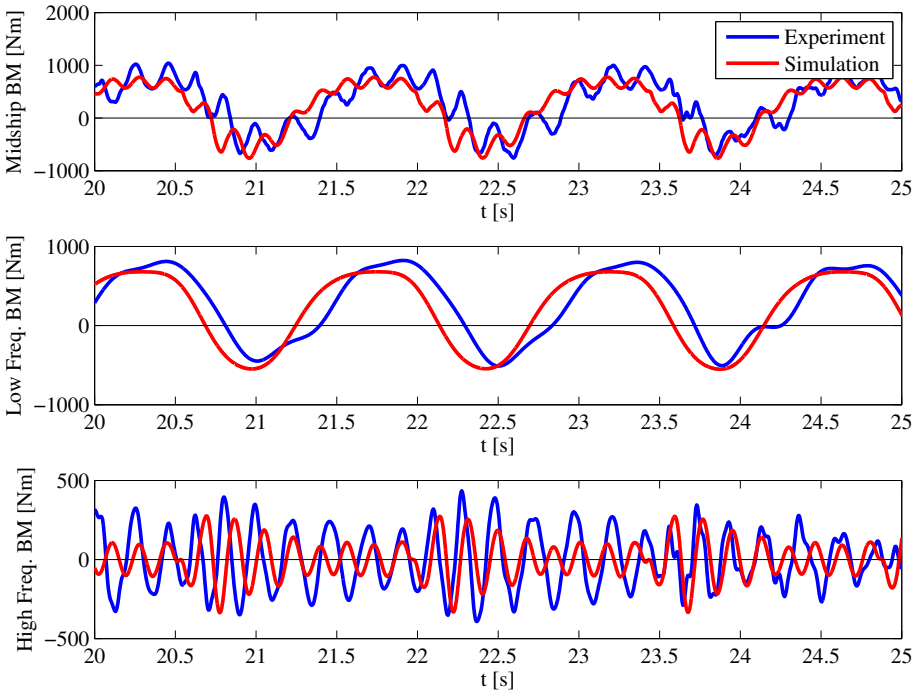

Figure 5.37: JHSS refined coarse grid: midship bending moment time series comparison - 15 knots, 1/15 wave slope.

The wave induced, low-frequency bending moment time series for the 15 knot cases are similar in shape to those of the fine grid, though with lower amplitude. This is due to the coarser discretization on the majority of the vessel and that wave excitation is a global load. The whipping response predicted for the 15 knot, 1/15 wave slope case, shown in Figure 5.37, is fairly accurate for the initial response to impact, but again damps out too quickly. The prediction for the 15 knot, 1/30 wave slope case has a larger ringing response than on the two uniform grids, but smaller than in the experiments, as seen in Figure 5.38. Figure 5.39 shows the 35 knot, 1/30 wave slope case does well predicting the amplitude of the ringing response, but not as well predicting the wave induced bending moment.

The midship bending moment frequency spectra of refined coarse grid are shown in Figures 5.40 to 5.42. The 15 knot, 1/15 wave slope case predits the first four harmonics of the bending moment quite well, while the 4-5 Hz response is not fully captured. Most of the predicted response in Figure 5.40 is focused on higher harmonics of the

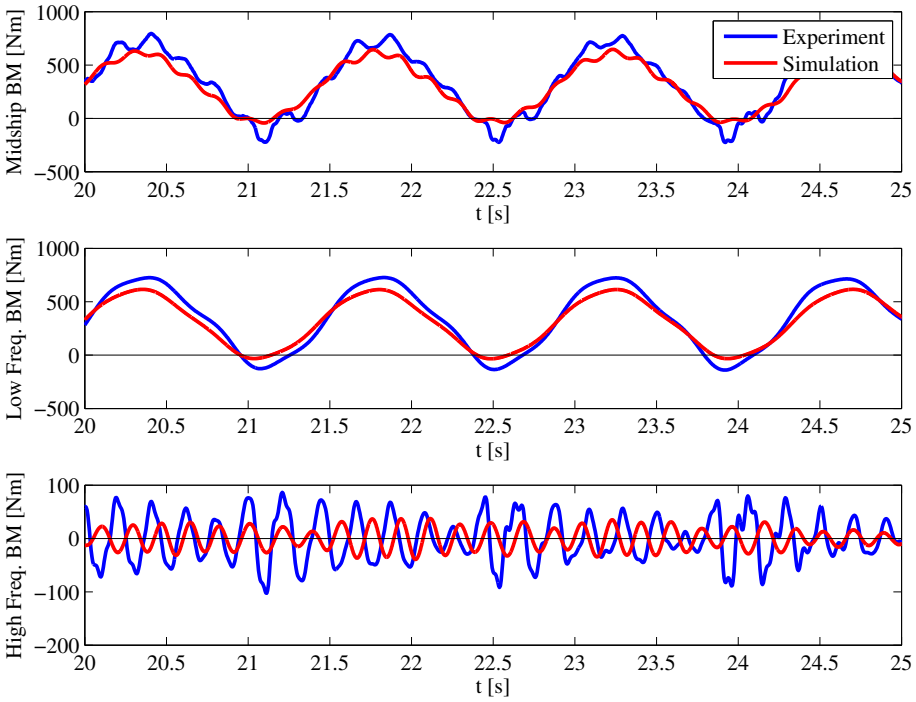

Figure 5.38: JHSS refined coarse grid: midship bending moment time series comparison - 15 knots, 1/30 wave slope.

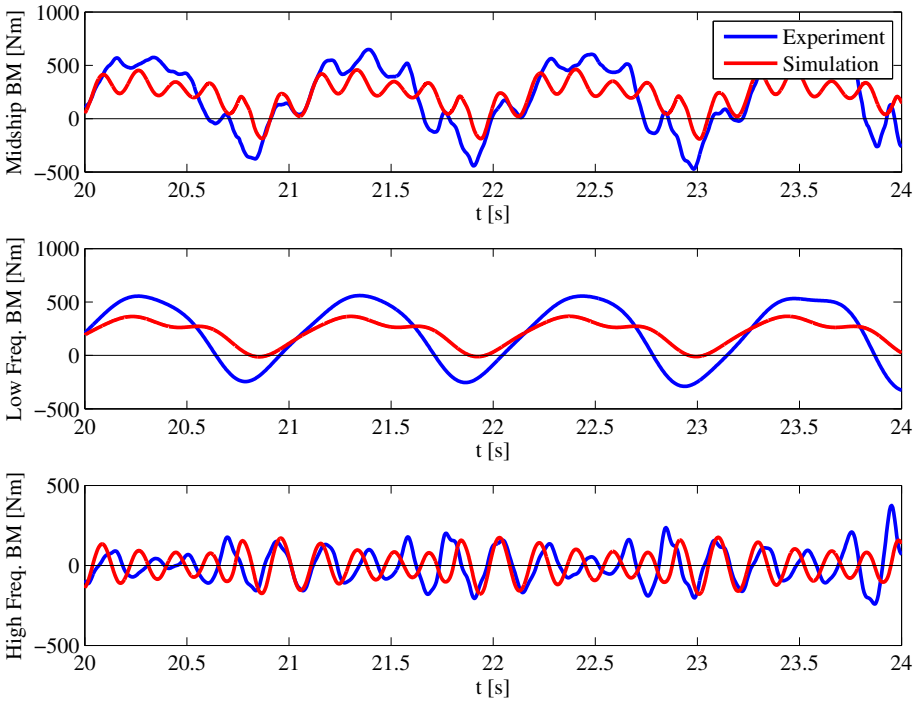

Figure 5.39: JHSS refined coarse grid: midship bending moment time series comparison - 35 knots, 1/30 wave slope.

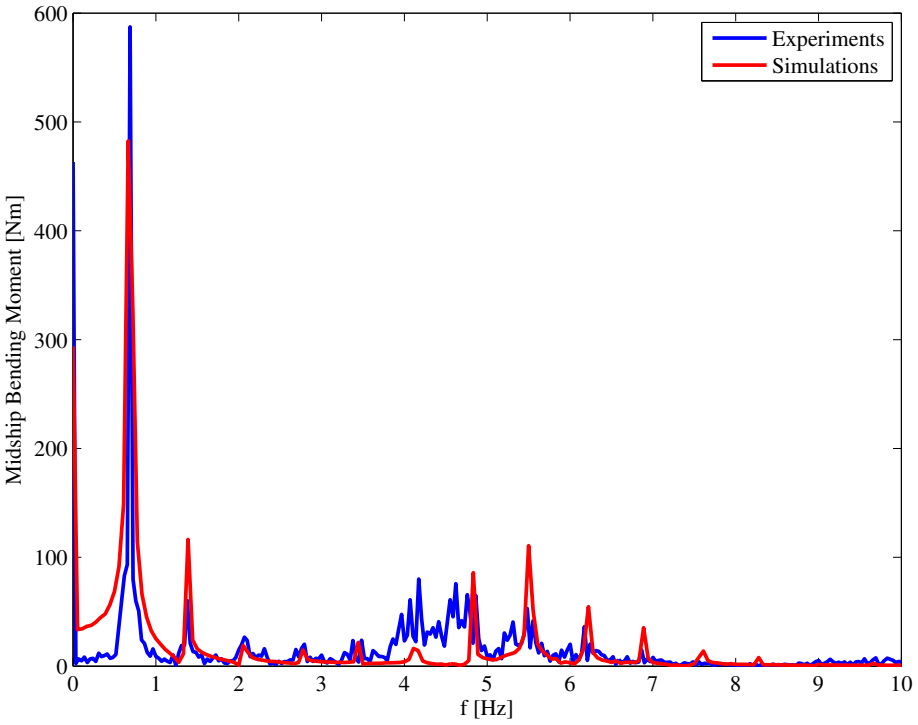

Figure 5.40: JHSS refined coarse grid: midship bending moment FFT comparison - 15 knots, 1/15 wave slope.

encounter frequency, not spread out as in the experiments. Figure 5.41 shows similar results as the uniform grids for the 15 knot, 1/30 wave slope case, even thougth the whipping response is larger. The predicted FFT for the 35 knot, 1/30 wave slope case compares well with the experiments except at the encounter frequency and the spike between 5 and 6 Hz.

The predicted seakeeping and midship bending moment results on the three different grids show that fine grid resolves the wave-induced response quite accurately. However, the slam-induced whipping response is not captured for all cases. The results for the refined coarse grid are encouraging for the use of a refinement block in the bow region. Therefore, a logical next step with the grid refinement study is to place a refinement block in the bow region of the fine grid.

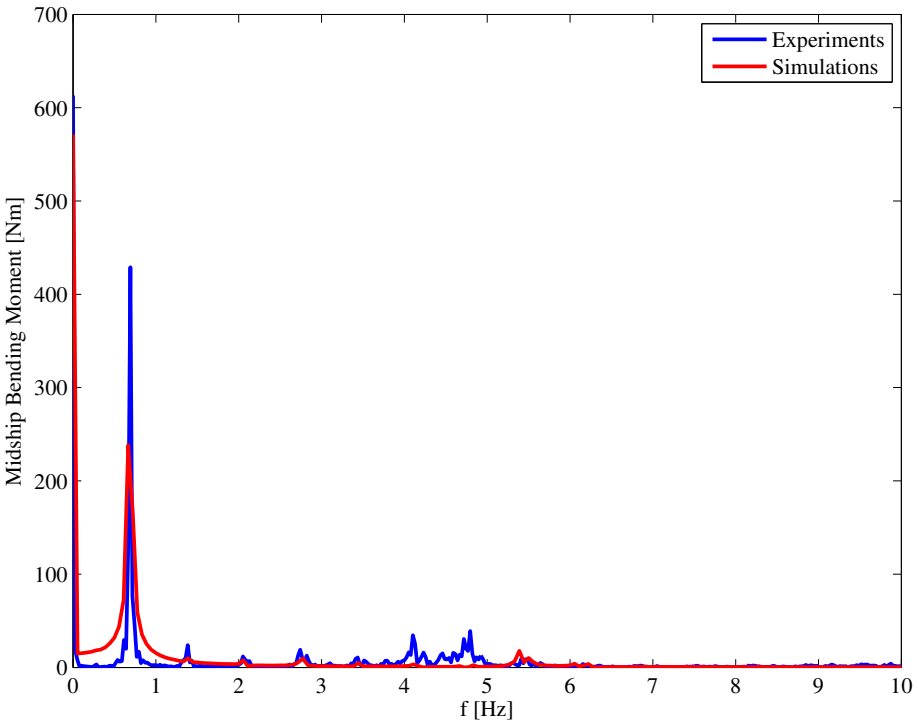

Figure 5.41: JHSS refined coarse grid: midship bending moment FFT comparison - 15 knots, 1/30 wave slope.

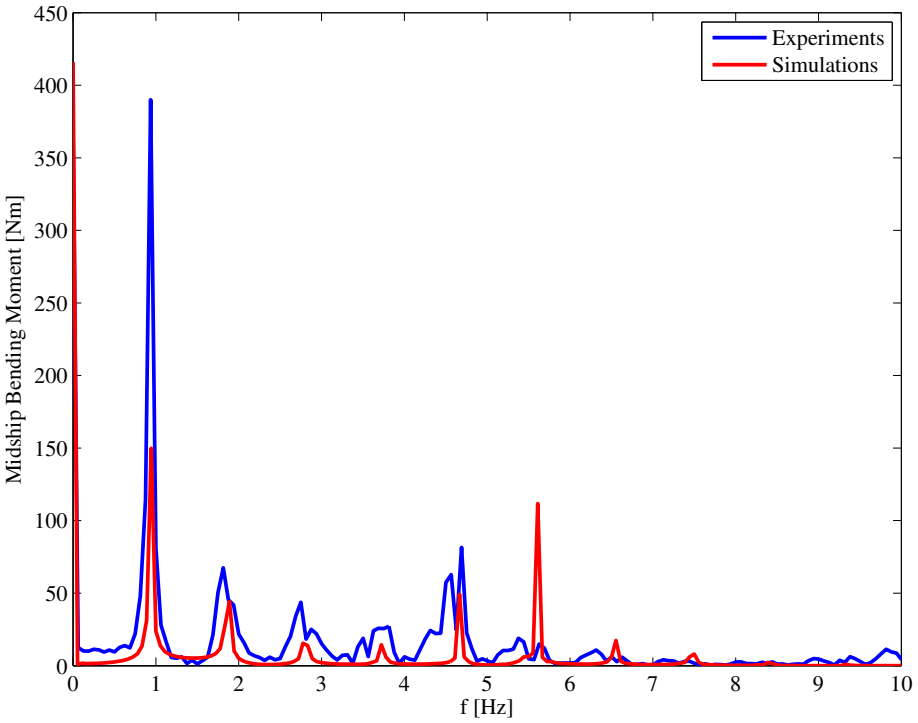

Figure 5.42: JHSS refined coarse grid: midship bending moment FFT comparison - 35 knots, 1/30 wave slope.

5.4.4 Comparison to Hydroelastic Approximations

The three cases are also used to evaluate the hydroelastic approximations described in Section 4.3. The present method is labeled as tighly-coupled (TC). The rigid/quasi-static approximation uses only the dry structure, while the rigid-dynamic approximation is shown with both the dry structure, as well as an estimate of the wet structure. The wet structure includes added mass estimated using Lewis forms, which are a strip theory approximation based on sectional area and beam-to-draft ratio. The formulas used in this work can be found in *Bishop and Price* (1979). Three-dimensional effects are not taken into account in the added mass estimate. This added mass estimate could be improved in a variety of ways, including using acoustic fluid elements, as in *Maki et al.* (2011). The comparison for the coarsest grid is shown for the three cases in Figures 5.43 to 5.45.

Figure 5.43 shows that with the current tightly-coupled simulations predict ringing at every wave encounter for the 15 knot, 1/15 wave slope case. The RQS approximation captures the low frequency wave induced bending moment but not the ringing, as would be expected. The RDyn approximation without added mass does not capture the ringing, while when including added mass prediction has a ringing amplitude similar to the tightly-coupled simulations. For the 15 knot, 1/30 wave slope case (Figure 5.44) where the tightly-coupled simulation does not exhibit ringing, the results with the RQS and RDyn approximations match well with the TC results. The RDyn approximation for the 35 knot, 1/30 wave slope case, seen in Figure 5.45, exhibits ringing when added mass is neglected, though at a higher frequency than the tightly-coupled simulation. The amplitude of the ringing is larger when using the approximation, which would give a conservative estimate of the stress in the structure.

The comparison to the approximations is shown for the fine grid in Figures 5.46 to 5.48. The 15 knot, 1/15 wave slope case shows the RDyn approximation with added

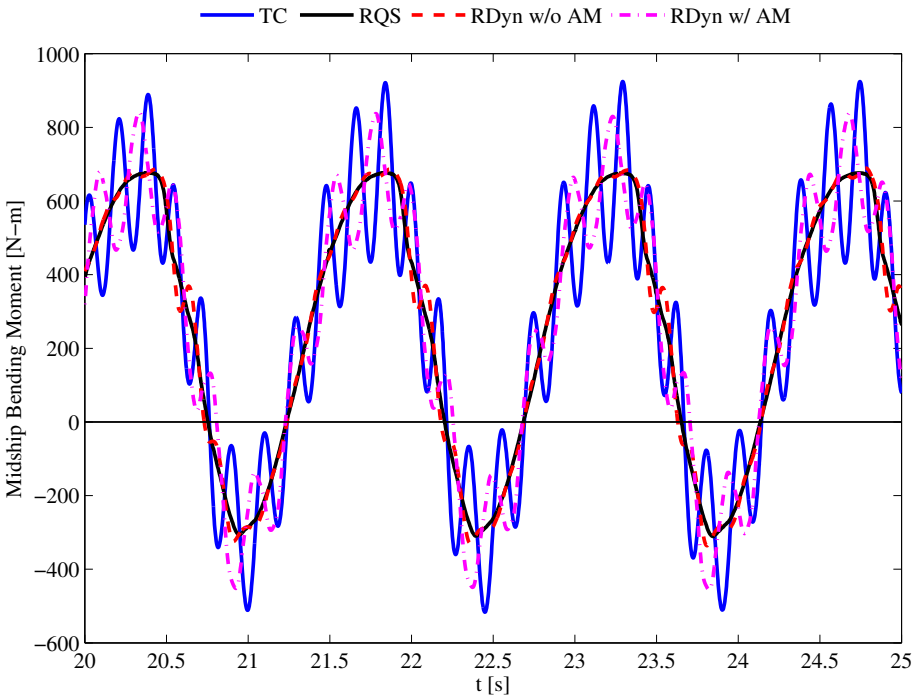

Figure 5.43: JHSS coarse grid: midship bending moment time series comparison to approximations - 15 knots, 1/15 wave slope.

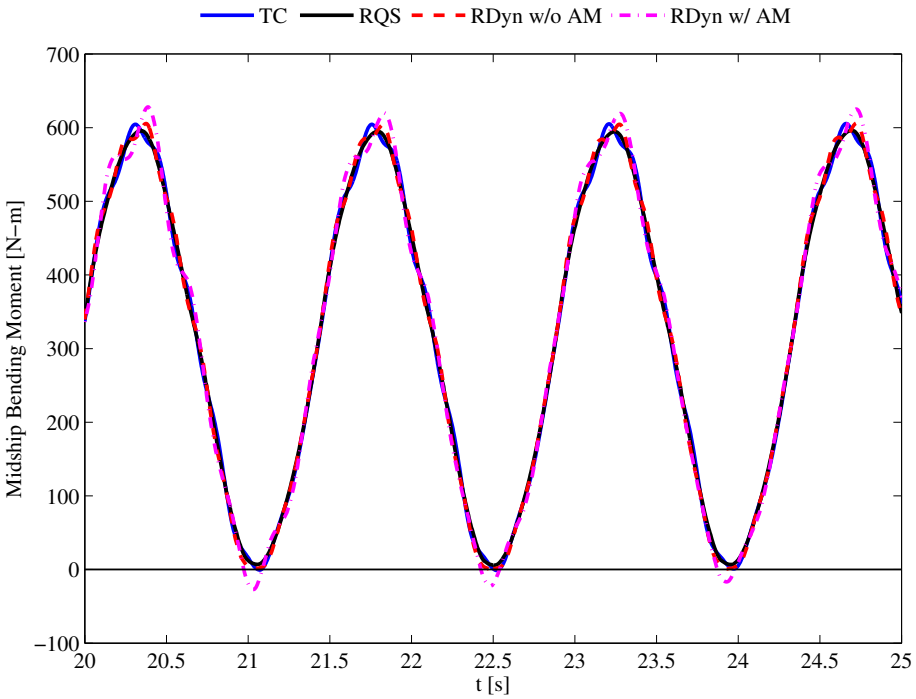

Figure 5.44: JHSS coarse grid: midship bending moment time series comparison to approximations - 15 knots, 1/30 wave slope.

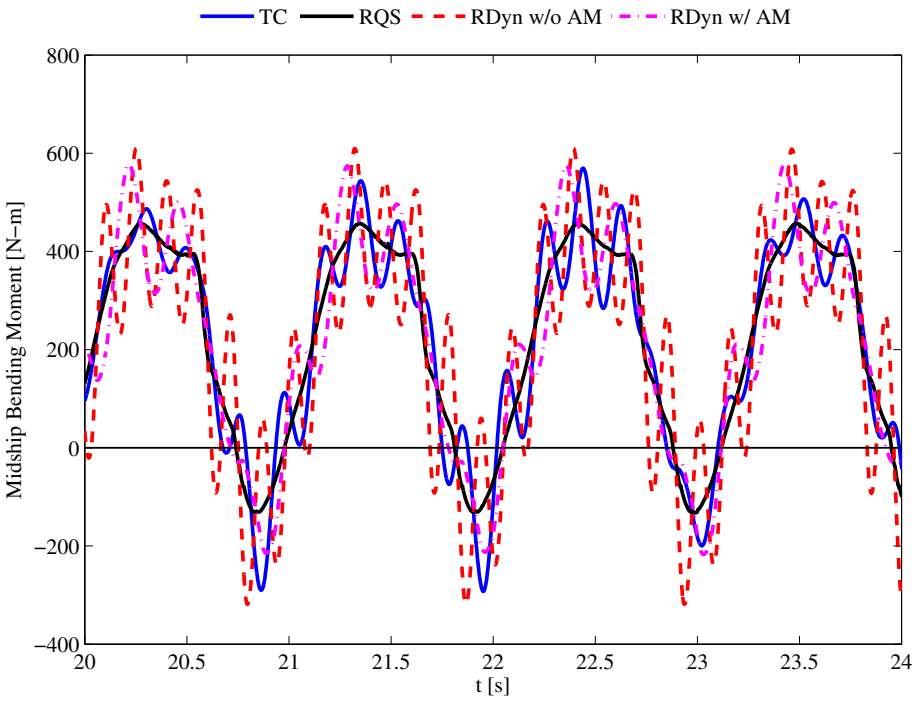

Figure 5.45: JHSS coarse grid: midship bending moment time series comparison to approximations - 35 knots, 1/30 wave slope.

mass comparing well with the tightly-coupled simulations when the bending moment is negative (sagging). The RDyn solution without added mass still does not resolve the ringing response. Note that the pressure time series is noisier for the medium grid than the coarse grid, and thus since the RQS approximation does not have any smoothing mechanisms, it is also noisy. For the 15 knot, 1/30 wave slope case, Figure 5.47 shows similar trends to the coarse grid (no whipping response), and the RQS and RDyn approximations compare well with the tightly-coupled simulations. Figure 5.48 shows the rigid-dynamic approximation again over-predicting the midship bending moment.

For the refined coarse grid, the comparison to the approximations is shown in Figures 5.49 to 5.51. For the 15 knot, 1/15 wave slope case, the rigid-dynamic approximation without added mass exibits more ringing than is seen on the coarse grid, indicating that the refinement is needed to capture the slamming loads. The 15 knot, 1/30 wave slope results in Figure 5.50 are similar to those for the fine grid. The

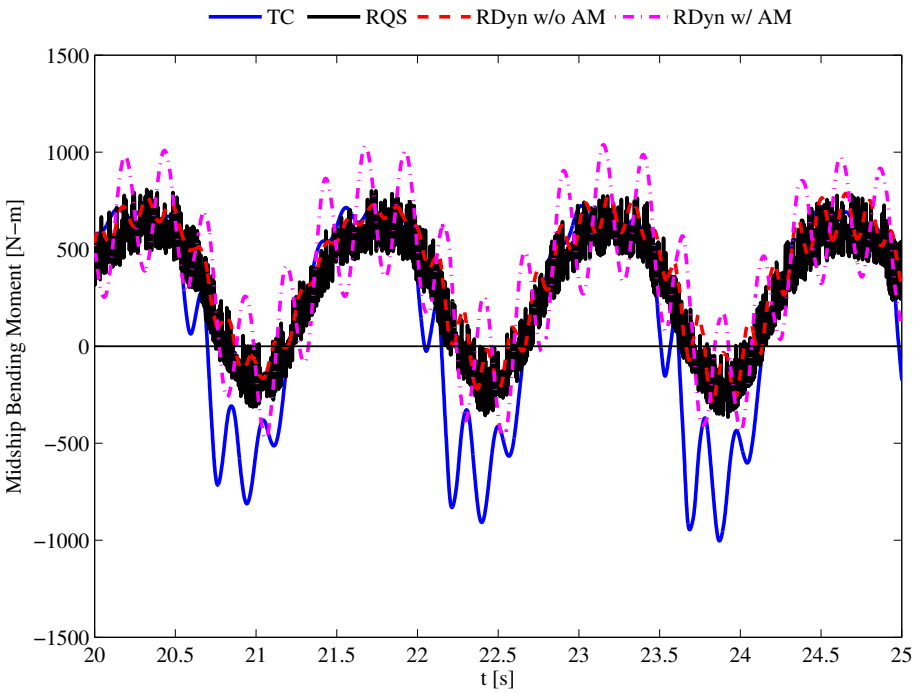

Figure 5.46: JHSS fine grid: midship bending moment time series comparison to approximations - 15 knots, 1/15 wave slope.

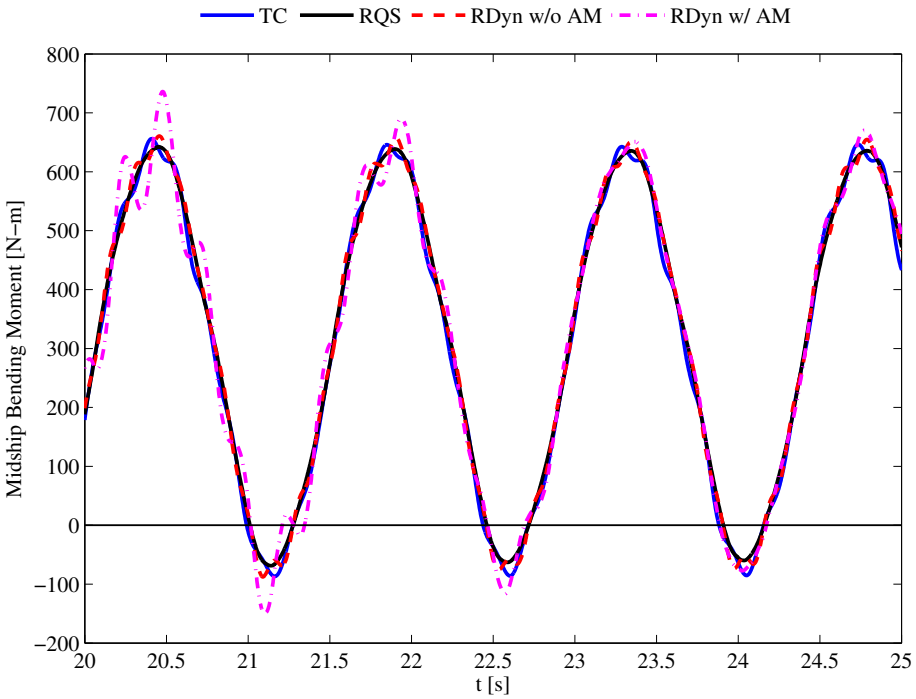

Figure 5.47: JHSS fine grid: midship bending moment time series comparison to approximations - 15 knots, 1/30 wave slope.

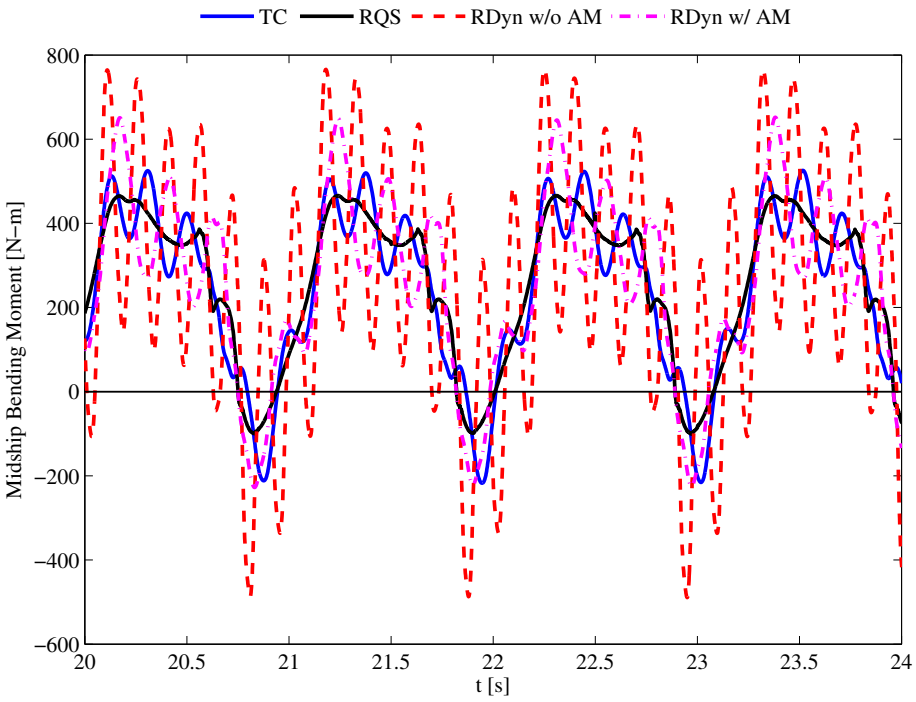

Figure 5.48: JHSS fine grid: midship bending moment time series comparison to approximations - 35 knots, 1/30 wave slope.

rigid-dynamic approximation does well for the 35 knot, 1/30 wave slope case, with the sagging moment overpredicted when added mass is included, seen in Figure 5.51.

Based on the three cases shown in this section, it can be seen that hydroelastic effects can be important to consider. For the 1/30 wave slope cases, the rigid-dynamic approximation yeilds similar stress ranges as the tightly-coupled simulations. For the 15 knot, 1/15 wave slope case, the approximations do not capture the sagging moment, with the rigid-quasi-static respone not matching the time average of the tightly-coupled response. A comparison of rigid body motion between rigid and elastic hulls, shown in Figure 5.52, also demonstrates the effects of including the elasticity of this case. Thus, for some cases hydroelastic effects are important to consider. A more exhaustive parameter search would give designers a better understanding of under what conditions to include hydroelastic effects.

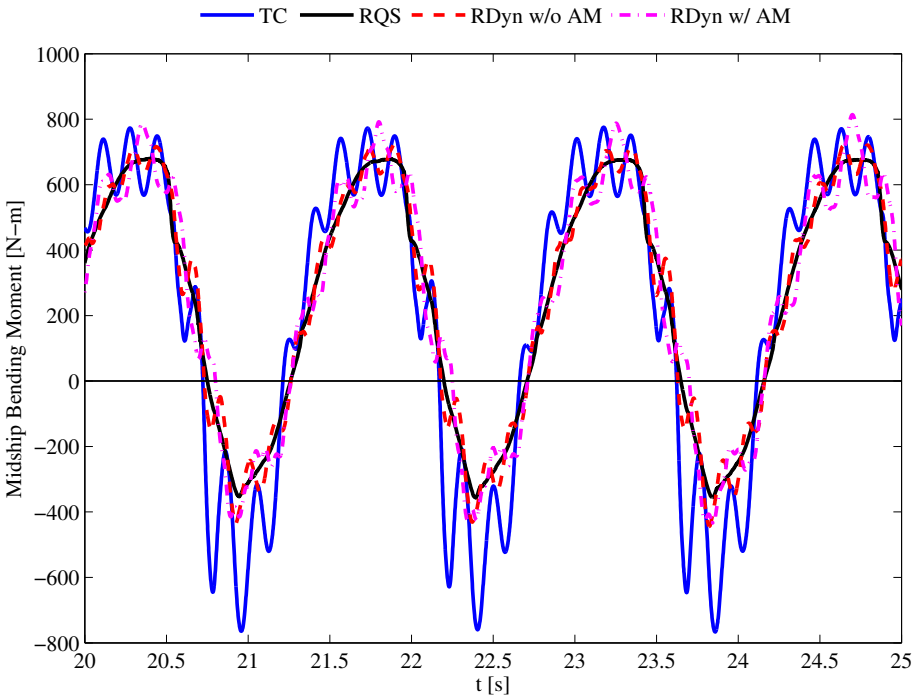

Figure 5.49: JHSS refined coarse grid: midship bending moment time series comparison to approximations - 15 knots, 1/15 wave slope.

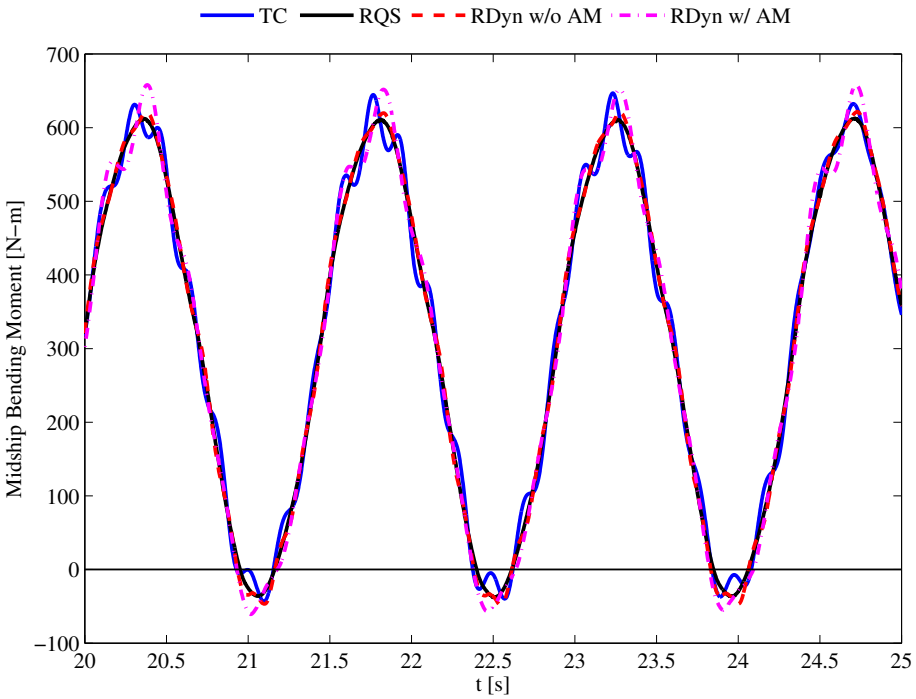

Figure 5.50: JHSS refined coarse grid: midship bending moment time series comparison to approximations - 15 knots, 1/30 wave slope.

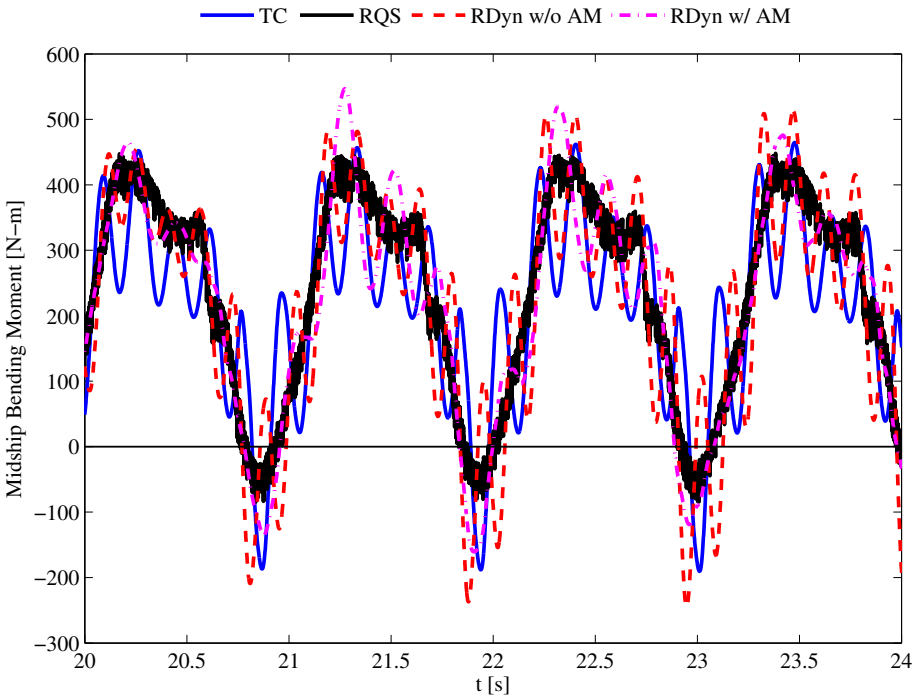

Figure 5.51: JHSS refined coarse grid: midship bending moment time series comparison to approximations - 35 knots, 1/30 wave slope.

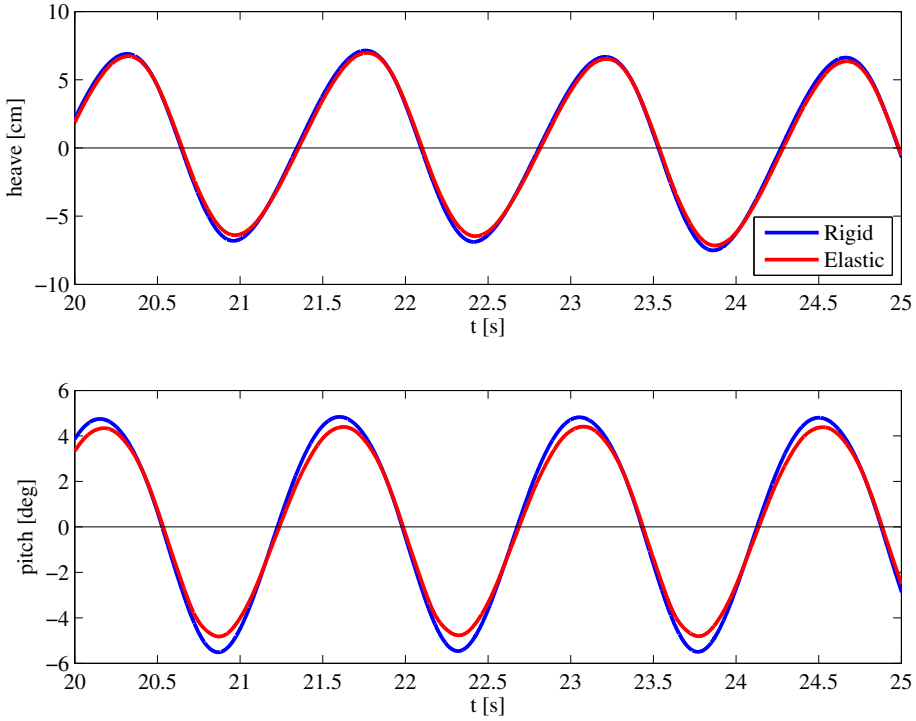

Figure 5.52: JHSS rigid body motion comparision for 15 knot, 1/15 wave slope case: rigid vs. elastic.

5.5 Summary

This chapter validates the present method for hydroelastic problems with a ship in a seaway. The ability to generate, propogate, and dissipate waves is shown. A Wigley hull is used to evaluate the effects of iteration on accuracy for the rigid body motion solver. Then, the combined rigid body and flexural solver is validated with experiments of an elastic box barge. Finally, the JHSS segmented model tests are used to further validate the method for cases with large waves in which the hull experiences whipping. The JHSS model is also used to evaluate common hydroelastic approximations versus the present method.

With the JHSS model, three cases are studied with realistic ship geometry. For one of these cases, hydroelastic effects are shown to be important for predicting the structural response. With a broader range of case parameters, the current method can be used to inform designers when hydroelastic effects are important to include.

CHAPTER VI

Summary and Conclusions

6.1 Summary

A fluid-structure interaction method and tool has been developed for the modeling and analysis of marine vessels that encounter slamming events while moving in a seaway. The method uses a CFD approach to solve the fluid equations and a modal basis to describe the structure. The modal basis is generated from a finite-element model. The use of finite-volume CFD with VOF interface capturing allows for implicit capturing of nonlinear viscous free-surface behavior. The use of a modal basis for the structure implies small deformations, which is appropriate for many metallic ship structures. The structures are modeled using finite elements in a custom program which also performs the modal analysis. The fluid-structure coupling code is implemented as a library within the CFD solver to maximize efficiency. The method is validated on and used to analyze several important hydroelastic problems.

The FSI method is validated by comparing the structural response of a wedge-shaped body that enters a calm free surface with constant velocity. Comparison is made with the theoretical results of *Korobkin et al.* (2006). As a model for a vessel in a seaway, the entry and exit of the same wedge-shaped body is studied for motion with constant acceleration as a rigid body before an elastic structure is added. The motion is chosen to result in either a chines-dry or chines-wet trajectory.

The rigid-body force and the position of the jet root on the body compare well with impact theory and jet-root model of Wagner during the phase in which the wetted region of the body is increasing. Then the problem of the entry and exit of an elastic wedge is studied. A wide range of plate thicknesses is studied to examine the influence of elasticity on the deflection and stress. Comparison is made with two common approximate methods: rigid-quasi-static and rigid-dynamic. Analysis of the comparison shows that the rigid-quasi-static approximation may under predict stress by a factor of more than two. The rigid-dynamic approximation is more accurate with an under prediction of approximately 20% and over prediction of 50% across the range of loading periods.

The rigid-body motion solver is validated using the Wigley hull seakeeping experiments of *Journée* (1992). The amplitude and phase of the heave and pitch motions in regular, head seas are examined. The Wigley hull is selected for study because its narrow shape generates small added mass, and thus no relaxation is required. The comparison is made between the reported experimental values and simulations using different numbers of FSI iterations and different orders of time integration. The results obtained with three FSI iterations and second-order time integration are considered converged.

Experimental data for a segmented box barge is used to validate the combined rigid-body and elastic FSI solver. Response amplitude operators of heave, pitch, roll, vertical bending, horizontal bending, and torsion using the present method are compared to the experimental and numerical results reported in *Senjanović et al.* (2008) for regular, oblique seas. The results for the vertical plane motions (heave, pitch, and vertical bending) compare very well with a relatively coarse CFD grid. The horizontal bending modes require additional damping to account for the flow between the segment gaps in the experiment. The roll and torsion responses require finer discretization in the wave direction to accurately capture the motion.

Another set of experimental data used to validate the complete FSI tool is the JHSS segmented model data. An expansive data set was collected for this model, but only three regular, head seas cases are studied in this work. These three cases include two speeds and two wave slopes. Results are shown for three levels of discretization, as well as with the coarsest mesh refined only in the bow region. The results on the coarsest grid show that the discretization does quite well for wave-induced bending, but is not resolved enough to capture slamming and whipping. Grid refinement, especially in the bow region, is shown to improve the resolution of the impact flow and more accurately capture the ringing response due to slamming.

The JHSS model is also used to analyze the use of the rigid-quasi-static and rigid-dynamic approximations for global vessel structural response. Time series of the midship bending moment are used to show that the rigid-dynamic approximation can provide a good approximation of the response if added mass is included. The added mass is estimated with strip theory and Lewis forms, but improvements can be made to this estimation. However, it must be noted that the approximations still require the pressure distribution on the hull obtained by a seakeeping simulation, which takes practially the same amount of time as the tightly-coupled simulations.

The present FSI solver provides a tightly-coupled method for the simulation of marine vessels that undergo slamming in a seaway. The solver has been validated and analyzed to be as efficent as possible while maintaining high accuracy. Design rules are used in the early stage of ship design, and thus have the most influence on the track of a design. An important application of the present method is to provide high-fidelity information into the development of future design rules.

6.2 Contributions

The major contributions of this work are highlighted here, along with descriptions of their importance in the field of hydroelastic analysis.

- A tightly-coupled FSI solver has been developed that uses computational fluid dynamics and computational structural dynamics. The finite-volume CFD with volume-of-fluid interface capturing is important for solving the global wave-bending and slam-induced whipping problems together because this method can solve wave breaking and multi-valued free-surface flows (such as the jet-root) implicitly. This is an improvement over potential flow codes that commonly solve the two problems separately because of the overturning free-surface and jet-root associated with slamming.

- The algorithm implements several techniques to improve the computational efficiency over existing CFD-CSD solvers. The use of a modal basis for the structure allows for a reduction in the number of degrees-of-freedom when compared to a full finite-element model. The approximate boundary condition removes the need for solution of additional mesh deformation equations, which are expensive and not always robust. And finally, the inertial under-relaxation method allows for a stable solution with a smaller number of iterations than explicit relaxation. With all of these techniques, the expense for a hydroelastic simulation is nearly the same as that for a rigid-body simulation using CFD.

- A method is shown for developing a stability requirement for a relaxed tightly-coupled algorithm based on the ratio of added mass to physical mass. The stability limit for explicit under-relaxation matches that reported in previous results. A new stability limit is developed for the equations of motion with inertial under-relaxation by application of the same method.

- The current method has been used to evaluate industry approximations with a single, high-fidelity tool. The evaluation has been done for both the wedge entry and exit problem, as well as the JHSS model in head seas. These evaluations highlight parameter regions where hydroelastic effects are important, and

identify ranges where the approximations are valid.

6.3 Future Work

The current FSI solver has been demonstrated and validated on several problems. The solver can now be used to further expand understanding of when hydroelastic effects are important by comparing to the approximate methods. Studies should be performed on realistic ship geometries (such as the JHSS) with wide ranges of parameters. Parameters of interest include Froude Number, heading, wavelength (λ/L), wave period (T/T_n), wave height (H_s/L or H_s/d). Additionally, irregular waves add the spectrum shape and directional spreading functions. A thorough investigation of these parameters would give designers clear guidelines as to how they should include hydroelastic effects in their analyses.

While the current method is designed to be as efficient as possible, it is still not practical for use in early stage design. However, the solver can be used to develop improved approximate methods, as well as evaluate and update design rules.

The linear, small deflection approximation is not valid for all FSI problems. Adding the capability for non-linear structures would increase the versatility of the method to be able to solve a wider range of problems. The current use of finite elements in the grid matching makes the implementation of a non-linear finite-element model straightforward.

The current work neglects turbulence when solving the fluid equations. The influence of turbulence on hydrelastic response can be easily studied with the current solution framework by including turblence models in the CFD solution. Also important to consider is the influence of the approximate boundary condition on boundary layer generation, especially for problems where viscosity is important, such as maneuvering.

The study of the entry and exit of an elastic wedge yeilds interesting results,

namely that the structural deflection on exit could be larger than during impact. While experimental study of this problem would be difficult, it could provide validation of the presented results, and confirm the conclusion that exit is important to consider.

BIBLIOGRAPHY

BIBLIOGRAPHY

ASME (2008), Procedure for estimation and reporting of uncertainty due to discretization in CFD applications, *Journal of Fluids Engineering*, *130*.

Bishop, R. E. D., and W. G. Price (1979), *Hydroelasticity of Ships*, Cambridge University Press.

Causin, P., J. F. Gerbeau, and F. Nobile (2005), Added-mass effect in the design of partitioned algorithms for fluid-structure problems, *Computer Methods in Applied Mechanics and Engineering*, *194*(42-44), 4506–4527.

Chandrupatla, T. R., and A. D. Belegundu (2002), *Introduction to Finite Elements in Engineering*, Prentice-Hall Inc.

Das, K., and R. C. Batra (2011), Local water slamming impact on sandwich composite hulls, *Journal of Fluids and Structures*, *27*(4), 523–551.

Dessi, D., and R. Mariani (2006), Slamming load analysis of a fast vessel in regular waves: a combined experimental/numerical approach, in *Twenty-Sixth Symposium on Naval Hydrodynamics*, Rome, Italy.

el Moctar, O., T. E. Schellin, and T. Priebe (2006), CFD and FE methods to predict wave loads and ship structural response, in *Twenty-Sixth Symposium on Naval Hydrodynamics*, Rome, Italy.

el Moctar, O., J. Oberhagemann, and T. Schellin (2011), Free surface rans method for hull girder springing and whipping, *SNAME Transaction*.

Faltinsen, O. M. (1997), The effect of hydroelasticity on ship slamming, *Philosophical Transactions: Mathematical, Physical and Engineering Sciences*, *355*(1724), 575–591.

Faltinsen, O. M. (1999), Water entry of a wedge by hydroelastic orthotropic plate theory, *Journal of Ship Research*, *43*(3), 180–193.

Faltinsen, O. M. (2005), *Hydrodynamics of High-Speed Marine Vehicles*, Cambridge University Press.

Faltinsen, O. M., J. Kvålsvold, and J. V. Aarsnes (1997), Wave impact on a horizontal elastic plate, *Journal of Marine Science and Technology*, *2*(2), 87–100.

Farhat, C., M. Lesoinne, and P. LeTallec (1998), Load and motion transfer algorithms for fluid/structure interaction problems with non-matching discrete interfaces: Momentum and energy conservation, optimal discretization and application to aeroelasticity, *Computer Methods in Applied Mechanics and Engineering*, *157*, 95–114.

Friedman, Z., and J. Kosmatka (1993), An improved two-node timoshenko beam finite element, *Computers & Structures*, *47*(3), 473 – 481, doi:10.1016/0045-7949(93)90243-7.

Heller, S. R., Jr., and N. H. Jasper (1960), On the structural design of planing craft, *Quarterly Transactions of the Royal Institution of Naval Architects*, pp. 49–65.

Henwood, D. (2002), Approximating the hysteretic damping matrix by a viscous matrix for modelling in the time domain, *Journal of Sound and Vibration*, *254*(3), 575 – 593, doi:10.1006/jsvi.2001.4136.

Iura, M., and S. Atluri (1992), Formulation of a membrane finite element with drilling degrees of freedom, *Computational Mechanics*, *9*, 417–428, doi:10.1007/BF00364007.

Jacobsen, N. G., D. R. Fuhrman, and J. Fredsøe (2012), A wave generation toolbox for the open-source cfd library: Openfoam®, *International Journal for Numerical Methods in Fluids*, *70*(9), 1073–1088, doi:10.1002/fld.2726.

Jasak, H. (2009), Dynamic mesh handling in openfoam, in 47^{th} *AIAA Aerospace Sciences Meeting*, Orlando, Florida, USA, doi:doi:10.2514/6.2009-341.

Journée, J. M. J. (1992), Experiments and calculations on 4 wigley hull forms in head waves, (0909).

Keulegan, G. H. (1948), Gradual damping of solitary waves, *Journal of Research of the National Bureau of Standards*, *40*(6), 487.

Khabakhpasheva, T., and A. Korobkin (2013), Elastic wedge impact onto a liquid surface: Wagner's solution and approximate models, *Journal of Fluids and Structures*, *36*(0), 32 – 49, doi:10.1016/j.jfluidstructs.2012.08.004.

Kim, K.-H., J.-S. Bang, J.-H. Kim, Y. Kim, S.-J. Kim, and Y. Kim (2013), Fully coupled bem-fem analysis for ship hydroelasticity in waves, *Marine Structures*, *33*(0), 71 – 99, doi:10.1016/j.marstruc.2013.04.004.

Kim, Y., K. Kim, and Y. Kim (2009), Springing analysis of a seagoing vessel using fully coupled BEM-FEM in the time domain, *Ocean Engineering*, *36*(11), 785–796.

Korobkin, A. (2004), Analytical models of water impact, *European Journal of Applied Mathematics*, *15*, 821–838.

Korobkin, A., and T. Khabakhpasheva (2006), Regular wave impact onto an elastic plate, *Journal of Engineering Mathematics*, *55*, 127–150.

Korobkin, A., R. Guéret, and Š. Malenica (2006), Hydroelastic coupling of beam finite element model with wagner theory of water impact, *Journal of Fluids and Structures*, *22*, 493–504.

Korobkin, A. A., T. I. Khabakhpasheva, and G. X. Wu (2008), Coupled hydrodynamic and structural analysis of compressible jet impact onto elastic panels, *Journal of Fluids and Structures*, *24*, 1021–1041.

Kvålsvold, J., and O. M. Faltinsen (1995), Hydroelastic modeling of wet deck slamming on multihull vessels, *Journal of Ship Research*, *39*(3), 225–239.

Lu, C., Y. He, and G. Wu (2000), Coupled analysis of nonlinear interaction between fluid and structure during impact, *Journal of Fluids and Structures*, *14*, 127–146.

Maki, K. J., D. Lee, A. W. Troesch, and N. Vlahopoulos (2011), Hydroelastic impact of a wedge-shaped body, *Ocean Engineering*, *38*(3), 621–629.

Maman, N., and C. Farhat (1995), Matching fluid and structure meshes for aeroelastic computations: A parallel approach, *Computers and Structures*, *54*(4), 779–785.

Mariani, R., and D. Dessi (2012), Analysis of the global bending modes of a floating structure using the proper orthogonal decomposition, *Journal of Fluids and Structures*, *28*, 115–134.

Newman, J. N. (1994), Wave effects on deformable bodies, *Applied Ocean Research*, *16*, 47–59.

Oberhagemann, J., M. Holtmann, O. el Moctar, T. E. Schellin, and D. Kim (2009), Stern slamming of a LNG carrier, *Journal of Offshore Mechanics and Arctic Engineering*, *131*(3).

Paik, K., P. M. Carrica, D. Lee, and K. J. Maki (2009), Strongly coupled fluid-structure interaction method for structural loads on surface ships, *Ocean Engineering*, *36*(1718), 1346–1357.

Papaioannou, I., R. Gao, E. Rank, and C. M. Wang (2013), Stochastic hydroelastic analysis of pontoon-type very large floating structures considering directional wave spectrum, *Probabilistic Engineering Mechanics*, *33*(0), 26 – 37, doi: 10.1016/j.probengmech.2013.01.006.

Piro, D., and K. Maki (2011), Hydroelastic wedge entry and exit, in 11^{th} *International Conference on Fast Sea Transportation*, Honolulu, Hawaii, USA.

Piro, D. J., and K. J. Maki (2013), Hydroelastic analysis of bodies that enter and exit water, *Journal of Fluids and Structures*, *37*(0), 134 – 150, doi: 10.1016/j.jfluidstructs.2012.09.006.

Piro, D. J., T. C. Fu, and K. J. Maki (2012), Joint high speed sealift (JHSS) segmented model test results, in *Thirty-First International Conference on Ocean, Offshore, and Arctic Engineering*, Rio de Janeiro, Brazil.

Remy, F., B. Molin, and A. Ledoux (2006), Experimental and numerical study of the wave response of a flexible barge, in *Fourth International Conference on Hydroelasticity in Marine Technology*, Wuxi, China.

Schellin, T. E., and O. el Moctar (2007), Numerical prediction of impact-related wave loads on ships, *Journal of Offshore Mechanics and Arctic Engineering*, *129*(1), 39–47.

Senjanović, I., Šime Malenica, and S. Tomausević (2008), Investigation of ship hydroelasticity, *Ocean Engineering*, *35*(5-6), 523 – 535, doi: 10.1016/j.oceaneng.2007.11.008.

Shames, I. H., and C. L. Dym (2003), *Energy and Finite Element Methods in Structural Mechanics*, Taylor & Francis Books, Inc.

Stenius, I., A. Rosén, and J. Kuttenkeuler (2007), Explicit FE-modelling of hydroelasticity in panel-water impacts, *International Shipbuilding Progress*, *54*, 111–127.

Stenius, I., A. Rosén, and J. Kuttenkeuler (2010), Hydroelastic interaction in panel-water impacts of high-speed craft, *Ocean Engineering*, *38*(2-3), 371–381.

Sun, H., and O. Faltinsen (2011), Predictions of porpoising inception for planing vessels, *Journal of Marine Science and Technology*, *16*, 270–282, doi:10.1007/s00773-011-0125-2.

Tuitman, J. T., and Š. Malenica (2009), Fully coupled seakeeping, slamming, and whipping calculations, *Journal of Engineering for the Maritime Environment*, *223*(3), 439–456.

Tuitman, J. T., Š. Malenica, and R. van 't Veer (2012), Generalized modes in time-domain seakeeping calculations, *Journal of Ship Research*, *56*(4), 215–233, doi: doi:10.5957/JOSR.56.4.100034.

Ubbink, O., and R. Issa (1999), A method for capturing sharp fluid interfaces on arbitrary meshes, *Journal of Computational Physics*, *153*(1), 26–50.

Š. Malenica, B. Molin, F. Remy, and I. Senjanović (2003), Hydroelastic response of a barge to impulsive and non-impulsive wave loads, in *Third International Conference on Hydroelasticity in Marine Technology*, Oxford, UK.

Wall, W. A., S. Genkinger, and E. Ramm (2007), A strong coupling partitioned approach for fluid-structure interaction with free surfaces, *Computers and Fluids*, *36*, 169–183.

Yang, S., F. Liu, H. Tsai, and D. Schuster (2004), Time-domain aeroelastic simulation on stationary body-conforming grids with small perturbation boundary conditions, *Tech. Rep. 04-0885*, American Institute of Aeronautics and Astronautics.

Young, Y., E. Chae, and D. Akcabay (2012), Hybrid algorithm for modeling of fluid-structure interaction in incompressible, viscous flows, *Acta Mechanica Sinica*, *28*, 1030–1041.